Examination of Parametric Subharmonic Instability of K_1 Internal Tides Generated by Tidal Flow over a Ridge

by

Andrew Bernakevitch

A thesis
presented to the University of Waterloo
in fulfillment of the
thesis requirement for the degree of
Master of Mathematics
in
Applied Mathematics

Waterloo, Ontario, Canada, 2022

Author's Declaration

I hereby declare that I am the sole author of this thesis. This is a true copy of the thesis, including any required final revisions, as accepted by my examiners.

I understand that my thesis may be made electronically available to the public.

Abstract

Internal gravity waves are thought to be a predominant source of mixing in the Earth's oceans. Here, we explore the interplay between two phenomena experienced by internal gravity waves - parametric subharmonic instability (PSI) and the changing of their inertial frequency by the effects of rotation (or the effective Coriolis frequency). PSI occurs when three waves satisfy a group of "resonant triad conditions", and we have a higher-frequency wave transferring energy to two waves of approximately half of the original wave's frequency. We get an effective Coriolis frequency in systems where the effects of vorticity are present. Waves experiencing the vorticity "feel" a changed Coriolis parameter, which has the potential to raise or lower the lower bound (or inertial frequency) on allowable frequencies of internal waves. Combined, these factors allow for the occurrence of PSI in regions wherein internal waves would not be able to achieve half the tidal frequency, due to the lowering of the inertial frequency by the effects of vorticity. We apply a 2D second-order finite-volume projection-based model to construct simulations of internal tides travelling over a ridge with the aim of creating such a situation. A variety of different stratifications are introduced into this model to create different background current structures and explore the visibility of the effective Coriolis frequency and the effects of PSI within. Simulations are consistently compared to controls to confirm desired effects and avoid undesirable inertial instabilities. Ultimately, using a carefully managed stratification created via a difference of hyperbolic tangents, the effects of PSI in a region enabled via a lowered inertial frequency are observed, and are confirmed via spectral density analysis to be seen within two orders of magnitude, one order of magnitude, and even eclipsing the amplitude of the primary tidal frequency. This work can help aid in the understanding of global mixing and circulation, and of the types of regions in which effects that may drive them occur.

Acknowledgements

I would like to thank all the people who helped make this thesis possible. In particular, I would like to offer my sincerest gratitude to my supervisor, Dr. Kevin Lamb, for his tireless support in drafting and revising of this thesis, as well as in learning and researching about internal waves (and more). It is through his support that this project was able to come to fruition. I would also like to thank Drs. Marek Stastna and Michael Waite, who, both directly and indirectly, helped provide both inspiration and resources for the completion of this thesis. Finally, I would like to extend my heartfelt thanks to my friends and family, both for their endless support and tireless patience throughout this experience.

Dedication

This thesis is dedicated to my friends and family, without the support of whom this thesis could never have been completed. A very special thanks to Trent, Carol, Lauren, Mia, and Sydney, for your tireless love and support.

Table of Contents

List of Figures

List of Tables

Chapter 1

Introduction

1.1 Overview

Oceanic mixing and turbulence has been a topic of great interest for the past several decades. From problems in fluid dynamics, to Earth sciences and even ecology (among so many others), understanding how waves interact, mix, overturn, and transfer energy plays an important role in developing our understanding of multiple dynamical systems across numerous fields of study.

Internal gravity waves in particular are thought to be a key source of mixing in the ocean. As a barotropic current flows over seafloor topography, or wind drives surface currents and disturbs the mixed layer in the upper ocean, these waves are produced, and they are ubiquitous in the planet's oceans (Ferrari and Wunsch, 2004 [1]). Internal waves are thought to transfer energy to the ocean's interior, and they are capable of moving energy over great distances. As, by some mechanism, they break and become turbulent, they produce significant mixing, which itself creates lateral density gradients capable of driving both local oceanic currents as well as those on the scale of global thermohaline circulation [2].

This mixing is a key driver of many processes. For example, it plays a key role in the redistribution of nutrients in the oceans, which affects the lives of many oceanic creatures (e.g. Boyd, 2007 [3]). Another relevant example, and one that we will focus on in particular, is this mixing's role in global oceanic circulation. The interaction of internal waves with seafloor topography (such as tidal currents traveling over seamounts/ridges, for example) drives the downward mixing of heat by allowing cool, dense water at the bottom of the

ocean to return to the surface. These tide-topography interactions are thought to be a source of around half of the 2 TW needed to maintain global overturning and circulation, not to mention a sink of a third of the world's barotropic tidal energy. It thus follows that understanding internal waves, their interactions, how much energy they produce, and where it ultimately ends up is a problem of great interest across many studies [2], [4], [5], [6].

This study in particular will focus on the interaction of internal tides with seafloor topography in the presence of a baroclinic background current and a particular path to turbulence down which this may lead. We will return to this, however, after we take a moment to examine important contextual elements for our study in greater detail.

1.2 On Internal Waves

Internal waves are a type of gravity wave which occur within the interior of a fluid. Common in the Earth's atmosphere and oceans, they occur within stratified fluids and are generated by a variety of different mechanisms. In our study, we will be considering internal waves created by fluid flow over topography triggering a propagating disturbance in the fluid.

Internal waves act as one of the major sources of mixing within the world's oceans, driving oceanic circulation and energy transfer (e.g. Ferrari and Wunsch, 2004 [1], Ferrari and Wunsch, 2009 [7]). They also play a key role in driving nutrient upwelling (Schaftstall et al., 2010 [8]), and are even thought to be a major factor in the shaping of continental shelves (e.g. Klymak et al., 2012 [2]). Internal waves are generated by many different means, and of these, one of the most important mechanisms for their generation is the interaction of the tides with seafloor topography. When baroclinic tides oscillate over the bathymetry, energy is transferred from the tides into baroclinic internal waves which are predominantly (though not exclusively) of the tidal frequency - so-called "internal tides". These internal tides then proceed to radiate outwards. Such a phenomenon has been observed in many studies; an in-depth study by Garrett and Kunze (2007) [9], for example, gives theoretical and numerical considerations to the generation of internal tides via tide-topography interaction. The produced internal tides have the potential to travel for tremendous distances, upwards of thousands of kilometres from the point of their generation (e.g. Zhao et al., 2012 [10]). Consequentially, these internal tides are destined towards interacting repeatedly with currents and mesoscale eddies (though we will not focus on that particular aspect of internal waves here) [5].

The interaction of tides and seafloor topography is a topic of significant interest (and one we will focus on at great length), particularly as it acts as a major source of the generation of internal wave energy within the planet's oceans. It is estimated that this process accounts for around 50% of the global internal wave energy, roughly equal to that of wind-driven forcing. Tide-topography interactions are capable of moving energy from barotropic tidal currents to internal tides at about 1 TW and are responsible for somewhere between 25-30% of the dissipation of barotropic tidal energy (e.g. Nikurashin and Ferrari, 2013 [11]). While energy generated by this process can be partly dissipated near the seafloor above rough topography (e.g. Ferrari et al., 2016 [12]), as previously mentioned, the energy produced can travel great distances from the site of its generation, particularly if the waves are generated primarily by isolated features in the bathymetry (Falahat et al., 2014 [13]). Geostrophic currents are also capable of interacting with the bathymetry to create lee waves, which injects an additional 0.2-0.4 TW into the internal wave field (Nikurashin and Ferrari, 2013 [11]). This process is particularly prevalent in the Southern Ocean, where the Antarctic Circumpolar Current produces a significant amount of internal waves by means of tide-topography interactions [6].

To be a bit more specific, as the surface tide propagates over density-stratified fluid, it forces the fluid over the seafloor topography. As the fluid is forced to move vertically over this topography, it is subject to a gravitational restoring force which generates internal waves. A result of this is the creation of internal pressure gradients that drive the production of the internal tides. Assuming our ocean is bounded, as the waves move away from the bathymetry, they do so in vertical modes. The lowest-order mode is the longest vertical wavelength capable of fitting between the seafloor and the ocean's surface; has the strongest velocities at these points and has zero horizontal velocity in the centre of the wave column (assuming a constant buoyancy frequency; in general, this may not always be true), and it has a horizontal phase speed that is higher than that of the other nodes. Higher-order modes generally travel slower and will have more zero crossings that zeroth-order modes. Higher-order modes are also often capable of breaking into turbulence via nonlinear processes transferring energy from lower-mode waves. This occurs at/near the point of their generation (Klymak et al., 2012 [2]) as they encounter remote topographical features (Nash et al., 2004 [14]), or as they interact with other waves in the interior (e.g. Mackinnon and Winters, 2005 [15]). Lower-order modes are prone to reflection and interference with one another, and scattering into higher-order modes, though the prevalence of each of these features at any

point is not well understood [2].

A factor of particular importance when considering the interactions of topography and internal waves is the steepness of the topography itself (Garrett and Kunze, 2007 [9]). As they leave the topography, internal waves travel in beam-like structures, along which energy propagates at an angle dependent on the waves' frequency and the given density stratification (more on this in Section 2). Topography steeper than that of the internal wave beams is said to be *supercritical*, while if it is shallower than the wave beams, it is called *subcritical*. Real topography often has regions of both classes, and they both play important roles in understanding and simulating internal tide generation. For more on subcritical topographies, see Bell, 1975 [16] and Balmforth et al., 2002 [17]; for supercritical, see, for example, Llewellyn Smith and Young, 2003 [18], St. Laurent et al., 2003 [19], and Klymak et al., 2012 [2].

1.3 On Instability and PSI

Internal waves experience intrinsic instabilities [20]. While linear theories suggest that all harmonics with frequencies less than the buoyancy frequency, N, are produced in internal wave generation (e.g. [16]), as a result of these instabilities they experience, their set of allowable frequencies is not strictly limited to harmonics. Indeed, interharmonic frequencies occur and have been studied as well [21]. Weakly non-linear interactions between internal waves have been proposed to be a mechanism of energy transfer between waves of different wavenumbers and frequencies (e.g. McComas and Müller, 1981 [22]). In weakly nonlinear theory, we often think about this in terms of so-called resonant triads - groups of three waves which interact such that the sums of their frequencies and wavevectors add to zero (more on this in Section 2.3), resulting in a transfer of energy back and forth between waves in the triad. In particular, if we have a given internal wave with wavevector $\vec{k}_0$ and frequency ω_0 and subject it to a perturbation, a type of instability known as parametric subharmonic instability (PSI) may occur. This instability involves the initial (lower-mode/large vertical wavelength) wave decaying into two smaller-scale (higher-mode/smaller vertical wavelength) waves each of about half the frequency of the original wave, with these new waves having opposite vertical wavenumber signs [21], [23].

It has been suggested that PSI may serve as a potentially significant source of energy loss in low-mode internal tides, particularly near critical latitudes (the smallest possible latitudes at which the subharmonic frequency - one

cycle per 24.8 hours - exceeds the local inertial/Coriolis frequency, f) [15]. In general, PSI may occur in any region wherein the frequencies of all three waves of the triad lie within the permissible band of internal wave frequencies, $f < \omega < N$, though it is often at its strongest when the daughter waves are produced at frequencies near that of the local inertial frequency [23].

Resonant triad interactions, including PSI, are too slow to be the dominant source of energy transfer in any incoherent isotropic wave field, such as that in the deep ocean (Olbers and Pomphrey, 1981 [24], Eden and Olbers, 2014 [25]). It has not, however, been ruled out that PSI could be more significant for coherent, low-mode internal tides, often produced by the motions of internal waves over tall, steep bathymetries. Indeed, studies such as Mackinnon and Winters, 2005 [15] and Hazewinkel and Winters, 2011 [26] suggest that PSI could be an important factor for energy transfer in situations like these, and results from studies including Alford et al., 2007 [27] and Mackinnon et al., 2013 [28] suggest that PSI is an active phenomenon within the ocean. The latter pair of studies also proposes that while in situ energy transfer rates are not exceptionally high, as the critical latitude near the equator is approached and crossed, the transfer of energy from near-inertial waves increases. These types of resonant nonlinear interactions (as well as nonresonant ones, as a matter of fact) are omnipresent within internal wave fields throughout Earth's oceans (Lvov et al., 2012 [29]), and they serve as a means of consistent, steady energy transfer towards wave motion occurring near or at local inertial frequencies [23]. Therefore, PSI (along with other similar resonant interactions) may indeed provide a possible pathway for the development of inertial and near-inertial waves as well as the transfer of energy from the deep ocean into oceanic mixing.

To remark, in addition to coherence, increased nonlinearity can also increase the energy transfer rate of PSI. Like with the case of coherence, this occurs at the point at which the waves are generated. While understanding the transition from linearity to nonlinearity has faced much difficulty in the past (e.g. Staquet and Sommeria, 2002 [30]), it is well understood that as this transition occurs and as nonlinearity becomes stronger, the time scales of PSI shorten (e.g. Mackinnon and Winters, 2007 [31]), thus amplifying its effects. Regions in which this may occur include regions of reflection of an internal wave beam from a boundary (Javam, Imberger, and Armfield, 1999 [32]), regions of intersecting internal wave beams (e.g. Javam, Imberger, and Armfield, 2000 [33]), and, as we have mentioned previously, regions of strong coherence among waves undergoing interactions (see the numerical simulations of Mackinnon and Winters, 2003 [34], Lamb, 2004 [35], and Gerkema et al.,

2006 [36]) [21]. Our goal will be to study near-inertial waves and PSI, so it will be these regions of coherence that we want to focus on, and we will turn our attention accordingly.

1.4 On Near-Inertial Waves

Near-inertial internal waves, or internal waves propagating with frequency close to that of the local Coriolis parameter, are a well-known and oft-studied phenomenon. Near the inertial frequency, the frequency spectrum of internal waves is thought to be similar to that of a continuum spectra on the order of frequency ω^{-2}, with a large, highly-variable, and event-like inertial peak (Fu, 1981 [37]). This type of peak acts in sharp contrast to the universal peak of the continuum spectrum of higher-frequency internal waves (e.g. Garrett and Munk, 1972 [38], Garrett and Munk, 1975 [39], Munk, 1981 [40]). Hence, the intermittency of near-inertial internal waves is an object of great interest.

In particular, the importance of the intermittency of near-inertial waves arises as a result of the near-inertial peak containing almost half of the total energy in the internal waveband [40], and providing a major contribution to the total vertical shear. Inertial waves created by winds and forced downward provide a significant source of energy in the ocean leading to turbulence and mixing. The interaction of these waves with their environment determines the location of this mixing, whether it will be in the interior or at the boundaries [41].

Kunze, in his 1985 paper [41], proposed a cause for this intermittency - the interaction of internal wave beams with geostophic shears. When such an interaction occurs, as explored in Mooers, 1975 [42], among other sources, in the interaction between the mean-flow and geostrophic shears, the effects of vorticity of the background flow ζ (we largely focus on its vertical component here) shift the lower limit of the frequency of the internal waveband from the local planetary Coriolis frequency, f, to a new value, dubbed the effective Coriolis frequency. This frequency takes the form $f_{eff}^2 \approx f(f + \zeta)$, meaning that the minimum frequency of the waveband could be raised or lowered depending on if cyclonic or anticyclonic currents are encountered.

The importance of such a shift, as proposed by Kunze, is that it can change the propagation behaviour of near-inertial waves. Most notably, in regions of anticyclone vorticity wherein the lower bound on internal wave frequencies is dropped, trapping and amplification can occur. To give an example, if we have

a spatially varying effective Coriolis frequency, the propagation behaviour of waves at frequencies near its value can change. Waves just above the effective Coriolis frequency may encounter strong inhomogeneities as they travel. If their wavevectors have a component approaching zero, they encounter turning points, while if a wavevector component approaches infinity, they hit critical layers. At these zones, these waves will reflect if they hit a turning point in the horizontal and will stall if they reach a critical layer in the vertical. Supposing the latter is the case, the waves' vertical wavelength would begin to decrease, resulting in a corresponding increase in amplitude by conservation of action-flux and a group velocity that is being lowered. The hard lower limit at f_{eff}, however, drives energy toward inertial frequencies. Hence, in these types of regions, instead of continuum enhancement (as our internal waves are prone to intermittence), we would expect to observe wave packets undergoing trapping and amplification [41]. This result was later explored in Kunze's 1986 paper [43], wherein mean and near-inertial velocity fields in warm core rings (large cyclonic mesoscale eddies circulating warm water; Kunze's warm core ring was located in the Gulf Stream) were studied and it was found that significant energy trapping and critical-layer amplification were occurring in regions of anticyclone vorticity, consistent with the ideas discussed previously. This trapping was further observed in Arctic measurements taken by Halle, 2003 [44]. Lateral shears may also have the effect of modulating f_{eff}, as has been observed in the Kuroshio by Rainville and Pinkel, 2004 [45], but this will not be our focus here.

As a consequence of this near-inertial wave trapping, a phenomenon known as inertial chimneys can occur, where as a result of the group velocity increasing with frequency above f_{eff}, waves are able to penetrate much deeper than expected [23]. These effects have been seen in numerical simulations by Zhai et al., 2005 [46], 2007 [47], as well as appearing in the aforementioned Kunze 1986 paper. As eddies are stronger at the ocean's surface, if near-inertial waves are trapped while propagating downward, they have the capability to reach depths where they encounter critical layers at points where the group velocity vanishes as background vorticity increases (assuming we are in the Northern Hemisphere; effects will be opposite in the Southern Hemisphere). That said, direct observations of this phenomenon are quite rare [23].

More generally, near-inertial waves appear commonly in studies involving wind-driven mixing. Indeed, wind supplies a significant amount of energy to near-inertial motions near the ocean's surface (Alford et al., 2016 [23]). Near-inertial waves appear in the deep ocean (Alford and Whitmont, 2007 [48]), on the continental shelf (Shearman, 2005 [49]), and even in the Laurentian Great

Lakes (e.g. Choi et al., 2012 [50]). As different currents converge, they are capable of driving motion into the surface of the ocean and the mixed layer's base, resulting in the production of near-inertial waves. This pumping can be brought about as a result of storms (e.g. Price, 1983 [51]), the variation of inertial frequency with latitude (the so-called β effect; e.g. D'Asaro et al,, 1995 [52]), the interaction of waves with mesoscale features (e.g. Weller, 1982 [53]), and coastlines (e.g. Pettigrew, 1980 [54], Kelly, 2019 [55]). While it is unknown to what extent each process contributes to energy generation and mixing, it is nonetheless true that all of them play a vital role in developing our understanding of internal currents and wind-driven mixing [23] [55].

1.5 Outline

Given what we have seen up to this point, our goal is to combine these many facets in a study observing if parametric subharmonic instability can be observed in regions where it would not otherwise be possible, observable as a result of vorticity's effects creating a suitable effective Coriolis frequency for the occurrence of resonant effects. Such a system will be created by simulations of internal tides sloshing over a ridge.

To this end, the rest of this thesis is outlined as follows. In Chapter 2, we will examine the theory behind the topics we have explored in this chapter from a mathematical standpoint. Chapter 3 will be a discussion of the code employed, derived from this theory, to create internal wave simulations. It will also include a brief discussion of conditions used to analyze the stability of our simulations and a process used to iterate on successive prospective tests. The results of these tests are included in Chapter 4, organized by the type(s) of current employed in the simulation. This will include a discussion of these results and their implications. Finally, we summarize all that we will see in a conclusion in Chapter 5.

Chapter 2

Theory

We will begin by introducing the fundamental equations with which we will be working, before examining the concepts of the effective Coriolis frequency and Parametric Subharmonic Instability, the two key components of our investigation.

2.1 Governing Equations

We commence by outlining the equations that will form the framework of our investigation. We will follow the same outline as in [57]. Assume that we have an incompressible fluid with negligible viscosity and diffusion on a rotating Earth. We will take the plane of motion to be the vertical xz-plane. Let $\vec{U} = (u, w)$ be the velocity vector of the fluid in this plane, v be its velocity in the y-direction, ρ_f the fluid's density, and P_d its pressure. Define f to be the Coriolis parameter and g to be acceleration due to Earth's gravity. We will also make the traditional f-plane approximation (neglecting the horizontal component of Earth's rotation vector), wherein we assume the Coriolis parameter is constant (as opposed to changing with latitude). Such an approximation is valid here as the length scales of the flows we will observe are not large enough to cause meaningful changes in the value of the Coriolis parameter. Assuming, then, that we are to solve the resulting equations of motion in 2D (i.e. we allow all relevant quantities to be functions of only x and z), then these equations are

given as follows:

$$\rho_f(\vec{U}_t + \vec{U}\cdot\vec{\nabla}\vec{U} - fv\hat{i}) = -\vec{\nabla}P_d - \rho_f g\hat{k} \tag{2.1}$$

$$v_t + \vec{U}\cdot\vec{\nabla}v + fu = 0 \tag{2.2}$$

$$(\rho_f)_t + \vec{U}\cdot\vec{\nabla}\rho_f = 0 \tag{2.3}$$

$$\vec{\nabla}\cdot\vec{U} = 0 \tag{2.4}$$

where $\vec{\nabla} = (\frac{\partial}{\partial x}, \frac{\partial}{\partial z})$ and t represents time. Now, we can perform the so-called Boussinesq Approximation. This approximation assumes that for the fluid in question, the overall density varies slightly about a mean value. We can safely make this approximation since this assumption largely holds true for water, whose density behaves in this manner (with the small fluctuations coming from differences in temperature, salinity, etc.). Note that our assumption of no diffusion reduces our time scale to be much smaller than the diffusive time scale, but in the ocean, the diffusive time scale is quite large due to small temperature and salinity gradients.

To perform the approximation, define:

$$\rho_f = \rho_0(1+\rho) \tag{2.5}$$

where we choose ρ_0 to be a reference density and define ρ to be a non-dimensional quantity.

We can break the pressure down into a component in hydrostatic balance with ρ_0 and a deviation term (which we will denote with P) [58]:

$$P_d = \rho_0(P - gz) \tag{2.6}$$

With these, we can re-write our initial equations as:

$$(1+\rho)(\vec{U}_t + \vec{U}\cdot\vec{\nabla}\vec{U} - fv\hat{i}) = -\vec{\nabla}P - \rho g\hat{k}$$

$$v_t + \vec{U}\cdot\vec{\nabla}v + fu = 0$$

$$\rho_t + \vec{U}\cdot\vec{\nabla}\rho = 0$$

$$\vec{\nabla}\cdot\vec{U} = 0$$

Finally, in the ocean, the parameter $\rho \ll 1$ and so in our case, $(1+\rho) \approx 1$. With this in mind, at last, we arrive at the final form of our equations. These equations are formally referred to as the "Stratified Euler Equations under the

Boussinesq Approximation", but we will abbreviate this henceforth as simply "the Boussinesq Equations".

$$\vec{U}_t + \vec{U} \cdot \vec{\nabla}\vec{U} - fv\hat{i} = -\vec{\nabla}P - \rho g\hat{k} \tag{2.7}$$

$$v_t + \vec{U} \cdot \vec{\nabla}v + fu = 0 \tag{2.8}$$

$$\rho_t + \vec{U} \cdot \vec{\nabla}\rho = 0 \tag{2.9}$$

$$\vec{\nabla} \cdot \vec{U} = 0 \tag{2.10}$$

It is these equations that we will use in our modelling and experimentation.

2.2 Internal Waves

Given the equations we have derived in the previous section, we are capable of modeling many of the properties of internal waves. We will carefully follow the approach of [59] and look at a few cases and key characteristics of internal gravity waves.

2.2.1 Understanding Internal Waves

To begin, assume that our domain is unbounded, not rotating, and experiences uniform stratification (as opposed to layered). Let us define the buoyancy (or Brunt-Väisälä) frequency of a fluid, N, such that:

$$N^2(z) = -\frac{g}{\rho_0}\frac{d\rho}{dz} \tag{2.11}$$

Note here that the ρ in this equation is the proper density of the fluid, and not to be confused with the dimensionless quantity we just finished using previously. Assume now that we take N^2 to be constant across the body of fluid (which corresponds to the assumption that stratification varies linearly in the vertical). Such an assumption allows us to get an exact solution to the (linearized) Boussinesq equations. This solution takes the form of a wave:

$$\exp(i(kx + \ell y + mz - \omega t))$$

The resulting substitution of a solution of this form into the Boussinesq equations leads to an equation for the wave frequency, ω, or equivalently, a dispersion relation for internal gravity waves:

$$\omega^2 = N^2\frac{k^2 + \ell^2}{k^2 + \ell^2 + m^2}. \tag{2.12}$$

One important property we see from this is that the frequency of the internal waves will never exceed the value of the buoyancy frequency. Another important note is that the frequency is completely independent of the magnitude of the wavenumber. Indeed, through simple substitution in spherical coordinates (where we take the radial coordinate to be the magnitude of the wavenumber, θ its angle with respect to the horizontal, and ϕ its projection to the x-axis), it is easy to show that

$$\omega = N\cos(\theta), \tag{2.13}$$

so we find that the frequency depends exclusively on the angle of the wavenumber relative to the horizontal and the buoyancy frequency's magnitude. Note that we allow θ to be positive or negative, meaning that the waves can travel upwards or downwards along the direction of the wavenumber vector.

Suppose, for a moment, that we rotate our coordinate system so that the wavevector aligns perfectly with the xz-plane, and there is no motion whatsoever along the y-axis. In such a case, we can solve for the remaining parameters exactly to obtain:

$$u = -A\frac{g\omega m}{N^2 k}\sin(kx + mz - \omega t) \tag{2.14}$$

$$w = A\frac{g\omega}{N^2}\sin(kx + mz - \omega t) \tag{2.15}$$

$$P = -A\frac{\rho_0 g m}{k^2 + m^2}\sin(kx + mz - \omega t) \tag{2.16}$$

$$\rho = A\rho_0\cos(kx + mz - \omega t) \tag{2.17}$$

Such a wave will have its phase travel at the speed:

$$c = \frac{\omega}{\sqrt{k^2 + m^2}}$$

This phase speed is the speed of propagation of the crests/troughs of the waves, and this propagation will occur in the direction of the wave vector. The waves will transfer energy at the *group velocity* $\vec{c_g} = \vec{\nabla}_k\omega = (c_{g_x}, c_{g_z})$, where:

$$c_{g_x} = \frac{\partial\omega}{\partial k} = \frac{\omega m^2}{k(k^2 + m^2)}$$

$$c_{g_z} = \frac{\partial\omega}{\partial m} = -\frac{\omega m}{k^2 + m^2}$$

Note that while the phase travels in the direction of the wave vector, the waves themselves will propagate in a direction perpendicular to the wavenumber vector. This means that energy is transferred perpendicular to the wave vector.

Note that as we can have a positive or negative value of the frequency, ω, the phase speed can accept positive or negative values. Additionally, the phase velocity (if we consider the waves travelling in the direction of the wave vector) could have differing signs in the vertical direction, depending on the orientation of the wave vector. Consequently, internal waves could see the upward or downward transference of energy, depending on the vertical phase speed's sign. When we have downward propagation of energy, while we see that the crests and troughs seem to rise, energy actually sinks, and vice-versa for the opposite (which follows naturally if one considers that $\frac{\omega}{m}\omega_m < 0$). Figure 2.1 gives a schematic of internal plane waves for visual reference, reproduced from [62] with permission from the original author.

2.2.2 Vertical Modes and Rotation

It is important to note that to this point, our approach is only valid should we assume that our domain is unbounded, not rotating, and uniformly stratified. We would like to proceed by relaxing these restrictions now. Let us take our body of fluid to be of uniform depth with a rigid lid. We introduce rotation by applying an f-plane approximation. Suppose we also let the buoyancy frequency be a function of z, and, as is usually the case in nature, we assume that $N^2(z) > f^2$ everywhere.

Applying our Boussinesq equations once again, let us apply the separation of variables to look for a solution of the form:

$$u = \tilde{F}(z)\tilde{U}(x,y)\exp(-i\omega t) \tag{2.18}$$

$$v = \tilde{F}(z)\tilde{V}(x,y)\exp(-i\omega t) \tag{2.19}$$

$$P = \rho_0\tilde{F}(z)\tilde{P}(x,y)\exp(-i\omega t) \tag{2.20}$$

$$w = i\omega\tilde{W}(z)\tilde{P}(x,y)\exp(-i\omega t) \tag{2.21}$$

$$\rho = -\frac{N^2\rho_0}{g}\tilde{W}(z)\tilde{P}(x,y)\exp(-i\omega t) \tag{2.22}$$

If we were to substitute this solution form into the Boussinesq equations, we would find that the density equation is satisfied exactly, leaving us with four

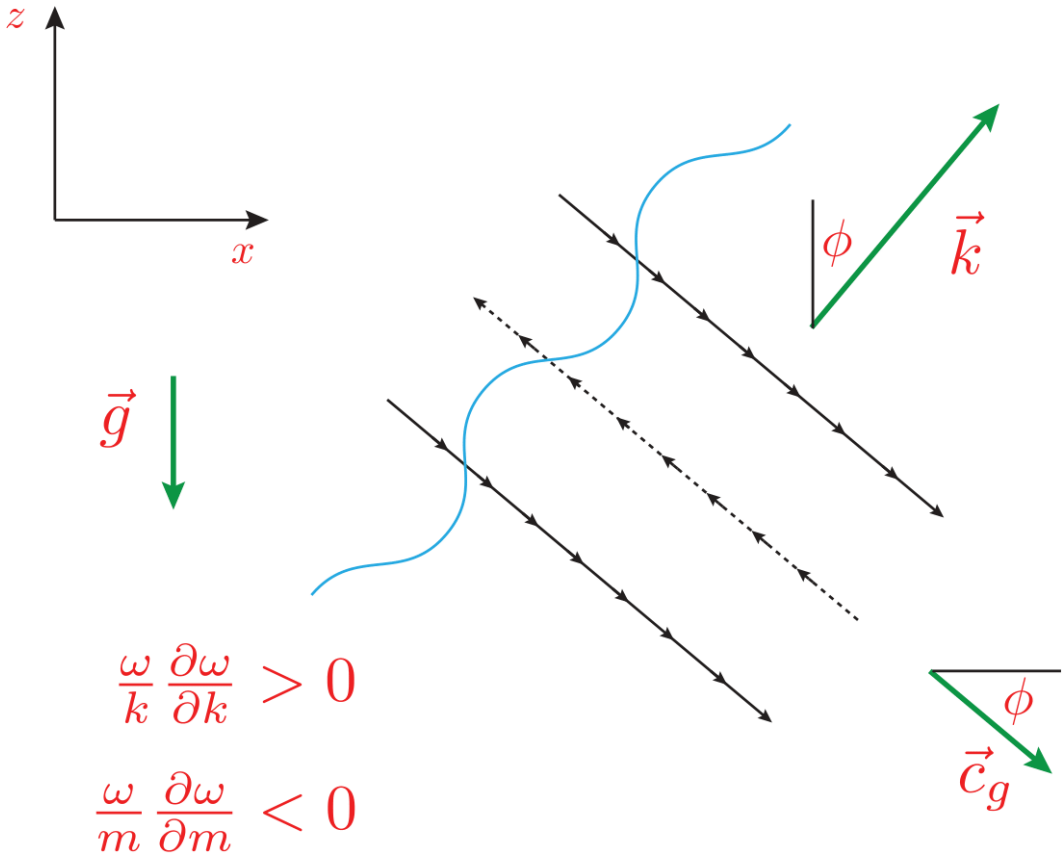

Figure 2.1: A schematic of an internal wave for $f = 0$. The sloping lines (both solid and dashed) indicate lines of constant phase, while the arrows along these lines show the current. When we have a positive frequency ($\omega > 0$), the lines of constant phase propagate in the direction of the wavevector, $\vec{k}$, which makes an angle of ϕ with the vertical. The group velocity vector $\vec{c_g}$ lies perpendicular to the wavevector, and has a vertical component with the opposite sign of $\frac{\omega}{m}$. The vector for gravity is denoted by $\vec{g}$. [62]

remaining equations:

$$-i\omega\tilde{U} = f\tilde{V} - \frac{\partial\tilde{P}}{\partial x} \tag{2.23}$$

$$-i\omega\tilde{V} = -f\tilde{U} - \frac{\partial\tilde{P}}{\partial y} \tag{2.24}$$

$$(\omega^2 - N^2)\tilde{W} = -\frac{d\tilde{F}}{dz} \tag{2.25}$$

$$\frac{1}{P}(\frac{\partial\tilde{U}}{\partial x} + \frac{\partial V}{\partial y}) = -\frac{i\omega}{\tilde{F}}\frac{d\tilde{W}}{dz} \tag{2.26}$$

We make a few notes. The first two equations are independent of the z-coordinate, the third equation is independent of the x and y coordinates, and the left-hand side of the fourth equation is purely in terms of x and y, while the right-hand side is purely in terms of z. For this last point to be the case, it must follow that both sides of the fourth equation are constant, and this constant is defined as $\frac{i\omega}{gh^{(j)}}$, where $h^{(j)}$ is called the equivalent depth (it has a dimension of depth and it takes the same role as the standard depth in the shallow water equations).

If we plug this constant into our third equation, the result yields:

$$\frac{d^2\tilde{W}}{dz^2} + \frac{N^2 - \omega^2}{gh^{(j)}}\tilde{W} = 0 \tag{2.27}$$

which is an equation that gives us vertical modes for $\tilde{W}$. A similar completion exists in the horizontal:

$$\frac{\partial\tilde{U}}{\partial x} + \frac{\partial\tilde{V}}{\partial y} = \frac{i\omega}{gh^{(j)}}\tilde{P} \tag{2.28}$$

We observe that this structure is exactly the same as that of shallow water equations [59]), but with the surface height replaced by $\frac{\tilde{P}}{g}$ and the depth replaced by $h^{(j)}$. Consequentially, we recover the solutions for shallow-water theory in the horizontal, yielding a periodic solution of the type:

$$(u, v, P) = (\tilde{U}, \tilde{V}, \tilde{P})\exp(i(kx + ly)) \tag{2.29}$$

with constant $(\tilde{U}, \tilde{V}, \tilde{P})$. These internal waves will also obey the dispersion relation for Poincaré waves in the horizontal:

$$\omega^2 = f^2 + gh^{(j)}(k^2 + l^2) \tag{2.30}$$

where it is assumed that (k, l) is a given pair. We can substitute this horizontal dispersion relation into our vertical mode equation to get:

$$\frac{d^2\tilde{W}}{dz^2} + (k^2 + l^2)\frac{N^2(z) - \omega^2}{\omega^2 - f^2}\tilde{W} = 0 \tag{2.31}$$

with boundary conditions $\tilde{W}(0) = \tilde{W}(H) = 0$. One important thing to note is the fraction in the second term of this equation - it is exactly the slope of an internal wave beam of frequency ω [21] (we will readdress this in the next section). Hence, we notice immediately that our internal waves will want to travel in beams of this given slope (more on internal wave beams in the Section 2.2.3). We note that to get solutions to our vertical mode equation, we require special values of ω such that we can have non-trivial solutions for $\tilde{W}$. Such ω are called eigenvalues, while the resulting $\tilde{W}$ are eigenfunctions (or vertical modes).

To conclude our discussion, we consider the case of uniform stratification (i.e. constant N^2) in a rotating bounded domain. More complicated scenarios including those with non-constant N^2 as well as nonlinear effects can be considered through various means (e.g. through numerical decomposition), though this falls outside the scope of our study.

For this situation, the vertical-mode eigenvalue problem has an exact solution:

$$\tilde{W}(z) = \sin(mz), \quad m = \frac{j\pi}{H}, \quad j = 1, 2, 3, ... \tag{2.32}$$

The resulting dispersion relation is:

$$\omega^2 = \frac{(k^2 + l^2)N^2 + m^2 f^2}{k^2 + l^2 + m^2} \tag{2.33}$$

We observe from this an infinite set of eigenfunctions produced from discrete eigenvalues m. We can also see that permissible frequencies lie in the range of $f^2 \leq \omega^2 \leq N^2$ (more on this later). If we were to perform this same analysis on an unbounded domain, we would get similar results, though our wavelengths here must satisfy the boundary conditions.

This process also restricts the value of the free constant we have been using:

$$gh^{(j)} = \frac{\omega^2 - f^2}{k^2 + l^2} = \frac{N^2 - f^2}{k^2 + l^2 + (\frac{j\pi}{H})^2} \tag{2.34}$$

As this term acts analogously to the radius of deformation in a shallow water system, we can similarly define a radius of determination for our system here

as well:

$$R_j = \frac{\sqrt{gh^{(j)}}}{f} \tag{2.35}$$

This radius of deformation determines to what extent waves are affected by gravity versus rotational effects. Waves with a shorter wavelength than this radius will experience primarily stratification's effects, while longer wavelengths with experience primarily rotational ones.

As a final remark, though we will omit the derivation, for near-inertial waves (as a special case in the ocean's interior taking the hydrostatic limit), one can repeat this process to get a dispersion relation and approximate group velocity:

$$\omega_{NIW}^2 = f^2 + N^2 \frac{k^2 + l^2}{m^2}, \quad c_{g_{z,NIW}} \approx -\frac{N^2(k^2 + l^2)}{m^3 f} \tag{2.36}$$

where the subscript NIW (for "near-inertial waves") is introduced to avoid confusion with our earlier discussion. While we ignore this derivation to focus on examining more general properties of internal waves applicable to our study, for more detail, consult Alford et al., 2016 [23].

2.2.3 Internal Wave Beams

As a final note on internal waves, we address what an internal wave beam actually is. We get an internal wave beam when we have an internal wave of finite cross-section. In an unbounded domain, an internal wave beam is a linear superposition of internal plane waves with parallel wave vectors. Note that a plane wave is an exact nonlinear solution of our governing equations (Phillips, 1966 [60]), as is any linear combination of plane waves with parallel wave vectors (e.g. Tabaei and Akylas, 2003 [61]). As an internal wave beam is a linear combination of individual plane-wave solutions to the Boussinesq equations with parallel wave vectors, it follows that the beam itself also exactly satisfies the nonlinear wave equations.

To construct an internal wave beam, we can employ the method of [62]. Let us assume we have a vertical profile of our wave at $x = 0, t = 0$, and let us choose our profile to be periodic with a period of twice the fluid depth ($2H$). This choice allows us to apply this method to construct reflecting beams in a fluid of depth H. We will take the first M terms of the Fourier series of our profile. We can then employ it to build of linear combination of waves.

We begin by setting:

$$w(x=0,z,t=0) = f(z) \approx a_0 + \sum_{n=1}^{M} a_n \cos(m_n z) + b_n \sin(m_n z) \tag{2.37}$$

where $z \in [-H, H]$ and $m_n = \frac{n\pi}{H}$. In particular, $f(z)$ is chosen so that it is approximately zero at $z = \pm H$ (this later allows us to have define the velocity at the seafloor to be zero). It then follows that (introducing the subscript u for "up"; more on this when we add reflections):

$$w_u(x,z,t) = a_0 + \sum_{n=1}^{M} a_n \cos(k_n x - m_n z - \sigma t) - b_n \sin(k_n x - m_n z - \sigma t) \tag{2.38}$$

with

$$k_n = \sqrt{\frac{\sigma^2 - f^2}{N^2 - \sigma^2}} m_n. \tag{2.39}$$

This gives us our desired linear combination of internal waves. Each wave has a wave vector of $(k_n, -m_n)$ and they are chosen to be in parallel with one another. Note that our choice of sign has the waves transporting energy in the positive horizontal and vertical directions (up and right). The sign of m_n can be swapped to point the waves downwards, and the sign of σ can likewise be swapped to give another valid solution. Swapping the signs of σ and k_n together still generally provides a solution that satisfies the dispersion relation, though due to its combination of waves travelling in the four cardinal directions, it follows that the wave vectors of the solution may not lie in parallel.

With this in mind, we can now consider a bounded domain. Suppose we have a rigid boundary at the surface, $z = 0$ (we make the rigid-lid approximation, so such a choice is not invalid). In such a case, the reflected wave will take the form (where we introduce the subscript d for "down", following up on our earlier convention):

$$w_d(x,z,t) = -a_0 - \sum_{n=1}^{M} a_n \cos(k_n x + m_n z - \sigma t) - b_n \sin(k_n x + m_n z - \sigma t) \tag{2.40}$$

The combination of the incident (upward-travelling) and reflected (downard travelling) waves is therefore:

$$\begin{aligned} w(x,z,t) &= w_u + w_d \\ &= \sum_{n=1}^{M} a_n[\cos(k_n x - m_n z - \sigma t) - \cos(k_n x + m_n z - \sigma t)] \\ &\quad - b_n[\sin(k_n x - m_n z - \sigma t) + \sin(k_n x + m_n z - \sigma t)]. \end{aligned} \tag{2.41}$$

An important thing to note here is that we have two sets of plane waves in this sum - one travelling upwards with wave vectors parallel to $(k_1, -m_1)$, and the other travelling downwards with wave vectors parallel to (k_1, m_1). These two sets of wave vectors are not parallel to each other. It follows that this linear combination does not work as a nonlinear solution to our Boussinesq equations.

We can rewrite our sum into a more compact form:

$$w = \sum_{n=1}^{M} [2a_n \sin(k_n x - \sigma t) + 2b_n \cos(k_n x - \sigma t)] \sin(m_n z) \tag{2.42}$$

$$= \sum_{n=1}^{M} A_n \sin(k n_x - \sigma t + \phi_n) \sin(m_n z) \tag{2.43}$$

We note that this form is that of a linear combination of horizontally propagating plane waves. Additionally, observe that $w(x, -H, t) = 0 = w(x, 0, t)$, so we have a wave that vanishes at our top and bottom boundaries. Hence, we have a solution to our Boussinesq equations in an ocean of finite depth H that vanishes at the surface ($z = 0$) and the bottom ($z = -H$). Note that such a solution would also be a solution if we were to extend the depth of our ocean by integer multiples of H.

An important point to note is that the nonlinear terms in our solution only occur wherever we have crossing upward and downward propagating beams, i.e. at the points of reflection at the boundary. When we have the nonlinear interaction of wave beams each with tidal frequency σ, a wave beam of tidal frequency 2σ is formed. Should this new beam now cross paths with the wave beams of tidal frequency σ, another interaction can can occur, resulting in wave beams of either frequency σ or frequency 3σ. In short, in this way, energy is transferred to increasingly higher frequencies.

One last remark here is that the linear combination wave beam solution we have developed is horizontally periodic. We have also set no bounds on our horizontal domain. Consequentially, these internal wave beams could transfer wave energy infinitely far in the horizontal, which is not physically possible in reality. Unlike in our idealized model here, interference, instabilities, and other factors act to prevent the infinite spread of energy by these beams. While internal wave beams are indeed capable of transferring energy over immense horizontal distances, it is still important to recognize this caveat.

2.3 Parametric Subharmonic Instability (PSI)

Before looking at parametric subharmonic instability, we briefly want to discuss the slope of an internal wave beam. Suppose we have a body oscillating in a linearly stratified fluid on a rotating Earth. Let the fluid have buoyancy frequency N_b and set the Coriolis frequency to f, both of which will be taken to be constant. It follows then that the slope, r, of the resulting internal wave beam of frequency ω can be obtained from [21]:

$$r^2 = \frac{\omega^2 - f^2}{N_b^2 - \omega^2} \tag{2.44}$$

and these waves will be of the form of the well-known St. Andrew's cross pattern. This slope value will be useful to us, both in defining the necessary components of PSI, and in observing it later on (see sections 4, 5). A change in this slope value, given our assumption of constant parameters, will suggest a changing frequency, something we expect to see in PSI.

To understand PSI, we must first define a resonant triad. Suppose we have three freely-propagating waves, each with different wave vectors and frequencies, $(\vec{k_i}, \omega_i)$, $i = 0, 1, 2$, each of which satisfies the dispersion relation $\pm r = \frac{k_h}{m}$ (where k_h is the horizontal wavenumber and m the vertical, r as described previously). If these three waves obey the following two conditions (the so-called "triad resonance conditions"), then they are said to be a resonant triad [21], [4]:

$$\vec{k_0} + \vec{k_1} + \vec{k_2} = 0, \quad \omega_0 + \omega_1 + \omega_2 = 0 \tag{2.45}$$

Should the second of these two conditions fail to be satisfied, then the result will be harmonically generated waves of frequency $\omega_0 + \omega_1 + \omega_2$, which will not have cumulative effects on wave amplitudes.

Where does such a set of conditions come from? Before we continue, let us take a moment to ponder this question. More generally, a resonant triad is a set of three waves in which a nonlinear interaction between two of them causes the third to undergo resonant forcing. They arise from quadratic nonlinearities in a system, wherein a wave with phase θ_0 interacts with a wave of phase θ_1, producing terms with the phase $\theta_2 = \theta_0 \pm \theta_1$. Should this combination of phases result in a freely propagating wave, then the aforementioned resonant forcing will occur. Consequentially, the sum/difference of the wave vectors and frequencies must be capable of satisfying the dispersion relation for a resonant triad to occur. It is this requirement that births the resonant triad conditions [63].

In the systems we will observe, we will want waves that both satisfy these conditions and the Boussinesq equations we derived in the previous section. One possible solution to the Boussinesq equation, among others, is a propagating internal wave solution. If we have a triad of waves with wavenumbers and frequencies $(\omega_0, \vec{k_0}), (\omega_1, \vec{k_1}), (\omega_2, \vec{k_2})$, then the resulting vertical velocity we get from the Boussinesq equations is:

$$w = \Sigma_{j=0,1,2} A_j \sin(m_j(z+h)) \exp(i(\vec{k_j} \cdot \vec{x} - i\omega_j t)) + c.c. \tag{2.46}$$

where $\vec{k_j} = k_j\hat{x} + \ell_j\hat{y} + m_j\hat{z}$ and A_j are the complex amplitudes of the three waves. To follow the triad resonance condition, these complex amplitudes of the waves must abide by a specific form. The derivation for this is rather intensive, so we will omit the lengthy algebraic steps and focus on the core ideas of the process.

To derive the amplitudes of the waves, we can apply the method of multiple scales and introduce slow-moving space and time scales to thereby introduce slowly evolving amplitudes into our problem. By doing as such, we are capable of eliminating resonant forcing terms in the resulting second-order problem. As we perform the perturbation expansion (and we do so in terms of streamfunctions for simplicity), the zeroth-order problem we get is the linear internal wave problem. At first order, we can get a solution to the zeroth-order term of the streamfunction of the form $\psi^{(0)} = A\exp(i\theta)$, where $A = \frac{1}{(k^2+m^2)(\sigma^2 - \frac{N^2k^2+f^2m^2}{k^2+m^2})}$, so long as θ does not take the form of a freely propagating internal gravity wave (i.e k, m, σ happen to satisfy the dispersion relation, making a zero denominator). So long as this is not the case, we get a bounded solution oscillating in time. Should this occur, however, an unbounded resonant forcing term instead acts as the particular solution, and this term takes the form $\psi^{(0)} = At\exp(i\theta)$. Recall that $\theta_j = k_j x + \ell j y + m_j z - \sigma_j t$.

To deal with the first order term in the streamfunction in our problem, it is important to consider our definition of a resonant triad once again. We have a resonant triad when we have three waves such that:

$$\theta_0 + \theta_1 + \theta_2 = 0 \tag{2.47}$$

Hence, we have that $\exp(-i(\theta_0 + \theta_1)) = \exp(i\theta_2)$ is a resonant forcing term. If $\exp(i\theta)$ acts as a resonant forcing term, it follows immediately that $\exp(-i\theta)$ does so as well, and hence $\exp(\pm i(\theta_0 + \theta_1))$, $\exp(\pm i(\theta_1 + \theta_2))$, and $\exp(\pm i(\theta_2 + \theta_0))$ are as well. Therefore, when we have a satisfied resonant triad condition, all six of these terms are resonant forcing terms. Note that, for simplicity, we assume that in our resonant triad condition, two waves have a frequency of

one sign, and the third the other (though such an assumption is not strictly necessary).

Turning back to the first-order solution for the streamfunction, we can arrive at a solution by eliminating terms of the form $\exp(\pm i(\theta_0-\theta_1))$, $\exp(\pm i(\theta_1-\theta_2))$, and $\exp(\pm i(\theta_2-\theta_0))$, as our resonant forcing terms are only proportional to the values discussed in the previous paragraph and their complex conjugates. To do this, we apply a multiple-scale expansion with a slow time scale (a slow spatial scale can also be introduced for considering the problem of horizontally-propagating internal modes, though that is a separate problem). Through manipulation and the application of conservation of wave energy across the triad, at last, the form of our wave amplitudes can be expressed analytically as follows [4], [63]:

$$\frac{dA_0}{dt} = s_0\omega_0 A_1^* A_2^* \tag{2.48}$$

$$\frac{dA_1}{dt} = s_1\omega_1 A_0^* A_2^* \tag{2.49}$$

$$\frac{dA_2}{dt} = s_2\omega_2 A_0^* A_1^* \tag{2.50}$$

$$s_0 = \frac{k_1 m_2 - k_2 m_1}{4k_0k_1k_2}\Big(\frac{k_1}{\omega_1} - \frac{k_2}{\omega_2}\Big)\Big(\frac{k_0}{\omega_0} + \frac{k_1}{\omega_1} + \frac{k_2}{\omega_2}\Big)\omega_0 \tag{2.51}$$

where the s_i are coefficients of interaction, and s_1 and s_2 can be determined by swapping the relevant indices throughout the equation with the zeroes in s_0.

To consider the development of these waves over time, we could consider the example where the amplitude of the primary wave is constant. For this, we let the subscript 0 denote our primary wave, and assuming A_0 is constant (which, of course, would only truly hold in the first moment of the interaction). In this case, we would have two equations for the other two wave amplitudes:

$$\frac{dA_1}{dt} = s_1\omega_1 A_0^* A_2^* \tag{2.52}$$

$$\frac{dA_2}{dt} = s_2\omega_2 A_0^* A_1^* \tag{2.53}$$

Supposing the initial amplitudes for the other waves in the triad were α_1 and α_2, respectively, then the solution for $A_1(t)$ would be given by:

$$A_1(t) = \frac{1}{2}\Big(\frac{s_1\omega_1 A_0^*\alpha_2^*}{\sigma} + \alpha_1\Big)\exp(\sigma t) - \frac{1}{2}\Big(\frac{s_1\omega_1 A_0^*\alpha_2^*}{\sigma} - \alpha_1\Big)\exp(-\sigma t) \tag{2.54}$$

where $\sigma = \sqrt{s_1 s_2}|A_0|$. Note that $A_2(t)$ could be similarly found by simply swapping the indices 1 and 2 in the previous equation. Consequently, we see exponential growth in the perturbation waves, controlled by the parameter σ [30], [4].

As for other parameters, the energy density of each wave in the triad can be given by $E_j = A_j A_j^*$. Each wave has a wave action of $\mathcal{A}_j = \frac{E_j}{\omega_j}$, and respective pseudo-momentum vector $\vec{p}_j = \mathcal{A}_j \vec{k}_j$. The energy of the system $E_0 + E_1 + E_2$ must be conserved (so we cannot have indefinite growth of the daughter waves), and the pseudo-momentum $\vec{p}_0 + \vec{p}_1 + \vec{p}_2$ is also conserved. Note that the total wave action is not generally conserved across the triad. In general, energy is periodically transferred between the members of the triad subject to the conditions we have heretofore established [30].

To conclude, we discuss the meaning of the term *PSI*. In systems like these, the first, larger-frequency wave is said to be unstable to the other two, transferring its energy to them via the instability. Though initially infinitesimally small, as we have seen, the amplitude of these disturbance waves has the capability to grow even beyond the amplitude of the primary wave; hence, these waves are called resonant. As this resonance appears to derive solely from the parameters of our system (as opposed to an external force), this resonance is called parametric. For internal gravity waves, the resonated waves experience their maximum amplitude when they are generated at around half of the frequency of the primary wave ($\frac{\omega_0}{2}$); this occurs in the limit of the high wavenumber regime, $|\vec{k_1}| \sim |\vec{k_2}| \gg |\vec{k_0}|$ (Staquet and Sommeria, 2002 [30]). These subharmonic waves generated via parametric resonance are what give us parametric subharmonic instability (PSI) [30], [4], [21], [20].

2.4 Effective Coriolis Frequency

Next, we want to turn our attention to a phenomenon known as the effective Coriolis frequency. Traditionally, we see the Coriolis frequency appear in systems wherein we consider a body of fluid on a rotating Earth, and, for a phenomenon in a sufficiently small domain, we usually consider this parameter to be a constant, determined by latitude. It is possible, however, for this constant to experience adjustments due to fluid vorticity, and this is where the effective Coriolis frequency appears.

To derive an expression for the effective Coriolis frequency, we can take our Boussinesq equations and include an additional equation for buoyancy.

A dispersion relation can be obtained from this set of equations by seeking a plane wave solution, which leads to a determinant to solve for the intrinsic frequency. This procedure is covered in detail in [41]. The key result we obtain from this procedure is an expression for the effective Coriolis frequency as one of the terms in the determinant. In its most exact form, it is expressed as:

$$f_{eff}^2 = f^2 + f(\frac{\partial v}{\partial x} - \frac{\partial u}{\partial y}) - \frac{\partial u}{\partial x}\frac{\partial v}{\partial y} \tag{2.55}$$

If we add an additional constraint on the geostrophic flow, we can simplify this further. We can assume that the transverse horizontal shears are significantly smaller than the Coriolis frequency, i.e. $|\frac{\partial u}{\partial y}|, |\frac{\partial v}{\partial x}| \ll f$, or equivalently, $|\frac{\partial u}{\partial y}|, |\frac{\partial v}{\partial x}| \sim \delta_f f$, where $\delta_f \ll 1$. This is equivalent to a small Rossby number approximation, and is valid in most of the ocean as it is a condition for stable quasi-geostrophic flow. Moreover, the horizontal strain terms $\frac{\partial u}{\partial x}\frac{\partial v}{\partial y}$ are much smaller in magnitude than the horizontal shear terms for geostrophic time scales much larger than a single inertial period. Finally, vorticities in many flow structures (e.g. open-ocean fronts, rings, and western boundary currents) typically assume values less than $0.2f$ [41].

Combined, these assumptions allow us to simplify our expression for f_{eff}. We can start by eliminating the third term:

$$f_{eff}^2 \approx f^2 + f(\frac{\partial v}{\partial x} - \frac{\partial u}{\partial y}) \tag{2.56}$$

If we introduce the horizontal vorticity parameter as $\zeta = \frac{\partial v}{\partial x} - \frac{\partial u}{\partial y}$, we can then substitute this into our equation to yield [64]:

$$f_{eff}^2 \approx f(f + \zeta) \tag{2.57}$$

Given our assumptions, we can also further approximate the square root (though we will not employ this specific form ourselves):

$$f_{eff} \approx f + \frac{\zeta}{2}$$

With this, we have our final working forms of f_{eff}^2 and f_{eff}.

The important thing to note about the effective Coriolis frequency is that it provides us with a new lower bound for the minimum propagation frequency of internal waves. To elaborate, if we recall the equation for the slope of internal wave beams, two conditions are placed upon the value of the beam

frequency ω: it must be no smaller than f (to get a real slope) and must be smaller than the buoyancy frequency (or the slope becomes undefined). That is, we have $f \leq \omega < N_b$. Now, however, if the waves experience an effective Coriolis frequency of $f_{eff} \approx f + \frac{\zeta}{2}$, then the lower bound of its propagation frequency is changed based on the background vorticity. For any cyclonic vorticity, as the vorticity increases, the allowable band of frequencies narrows. If the vorticity were negative, the band of frequencies would widen as the vorticity increased in magnitude. In this way, we have vorticity changing our permissible frequency spectrum, thus allowing us to consider wave effects in regions normally disallowed by traditional approximations (e.g [56]).

Keeping in mind what we discussed about PSI in the previous section, it is then possible to consider constructing near-inertial waves (or rather, waves near a lowered inertial frequency) that might allow for the frequency to take values required to achieve PSI in regions in which it would not otherwise be capable of doing so. This is our goal for this study, and we will use the next section to go into further detail about our means of doing so.

Chapter 3

Methodology

3.1 Code

To create the data needed to look at various internal wave setups and examine them for possible PSI, the numerical model outlined in [57] was used. While we will not go particularly deep into detail about the code here, a brief summary will be provided.

Based upon the numerical methods created by Bell, Colella and Glaz, 1989 [65]; Bell, Solomon, and Szymczak, 1989 [66]; and Bell and Marcus, 1992 [67], the code uses a second-order finite-volume projection-based method to solve the Boussinesq equations outlined in section 2.1.

The projection method operates as follows, noting that we perform this projection to enforce incompressibility. We want to eliminate the pressure terms from the Boussinesq equations from section 2.1. We can do so by noting that for any given vector $\vec{v}$, we can break it down into the sum of a divergence-free vector and a multiple of a strictly-positive scalar field function and a gradient, i.e.

$$\vec{v} = \vec{v}^D + a(x,z)\vec{\nabla}\phi \tag{3.1}$$

where $\vec{v}^D$ is a divergence-free vector. Such a decomposition can be unique, so long as adequate boundary conditions are imposed. For our case, we will choose the Dirichlet boundary conditions, such that $\vec{v}^D \cdot \hat{n}$ is specified on three sides of the domain of our problem, excluding the right-hand side boundary (more on this in the following section),

We can define a projection operator P_a to map the vector $\vec{v}$ onto its

divergence-free component, $\vec{v}^D$:

$$P_a(\vec{v}) = \vec{v}^D \tag{3.2}$$

Note that the projection operator itself will depend on the function $a = a(x, z)$ chosen and on the specifications of the boundary conditions.

Let us return to the first of our wave motion equations from Chapter 2.1 (though let us do so before fully completing the Boussinesq approximation, thus leaving $1 + \rho$ present in the equation). We can re-write the equation as follows:

$$\vec{U}_t + \frac{1}{1+\rho}\vec{\nabla}P = -\vec{U} \cdot \vec{\nabla}\vec{U} + fv\hat{i} - \frac{\rho}{1+\rho}g\hat{k} \tag{3.3}$$

The left-hand side of this equation has exactly a divergence-free vector ($\vec{U}_t$) plus a strictly-positive scalar field multiplied by a gradient. Hence, we can apply our previous definition of a projection to create the operator P_ρ so that:

$$\vec{U}_t = P_\rho(-\vec{U} \cdot \vec{\nabla}\vec{U} + fv\hat{i} - \frac{\rho}{1+\rho}g\hat{k}) \tag{3.4}$$

With this method, we can eliminate the pressure from our original equations (though the pressure gradient, which can be obtained once our projection equation is solved, will still be used). This operator is time-dependent, as the density is time-dependent and the boundary conditions have the potential to depend on time as well. Note that when we make the Boussinesq approximation, we can eliminate the density dependence from our projection. The dependence on the boundary conditions can also be eliminated by discretizing the projection operator. The procedure for doing so is complicated, however, and so we will leave its discussion to [57].

With this projection operator defined, the numerical problem we then seek to solve is: assuming we have a vector $\vec{v}$ and are given a density ρ, we wish to solve the following equation for $\vec{U}_t$

$$(1+\rho)\vec{U}_t + \vec{\nabla}P = \vec{v} \tag{3.5}$$

This amounts to constructing a basis of divergence-free vectors $\vec{\Psi}_{i,j}$ such that:

$$\vec{U}_t = \Sigma_{s,t}\alpha_{s,t}\vec{\Psi}_{s,t} \tag{3.6}$$

We then want to solve for the corresponding $\alpha_{i,j}$. Firstly, we want to construct the basis. As a part of doing so, we should consider how coordinates will work in our system.

The simulations to be used will apply terrain-following (σ) coordinates. A quadrilateral grid with I grid points in the horizontal and J grid points in the vertical is used for computation. The code operates by mapping the physical coordinates of our system (x, z) to coordinates inside the computational grid, (ξ, ζ), such that:

$$(\xi, \zeta) = (\xi(x, z), \zeta(x, z)) \tag{3.7}$$

We restrict our transformation such that $\xi = 0$ at the left boundary, $\xi = I$ at the right boundary, $\zeta = 0$ along the bottom bathymetry, and $\zeta = J$ at the surface of the fluid ($z = 0$). Note that if we were to use a free surface, this transformation would be dependent on time. Our Boussinesq equations then transform to be in terms of these new coordinates, though we will omit this derivation for brevity.

Returning to our projection, with the coordinates we have defined, let us consider the corners of each cell as defining a scalar grid. This scalar grid, (ξ, ζ), has coordinates $(\xi, \zeta) = (i, j)$ such that $i = 0, 1, ..., I,\ \ j = 0, 1, ..., J$. There are then $I + 1$ scalar grid points in the horizontal and $J + 1$ in the vertical direction.

We define the vector grid to be composed of two components: interior vector grid points and boundary vector grid points. Interior grid points sit in the centre of the vector grid cells (i, j) with coordinates $(i - 0.5, j - 0.5),\ \ i = 1, ..., I,\ \ j = 1, ..., J$ on our computational grid. Boundary vector grid points lie in the middle of the cell edges along the boundary of our domain. They have coordinates in the computational domain of $(0, j - 0.5), (I, j - 0.5)\ \ j = 1, ..., J$ and $(i - 0.5, 0), (i - 0.5, J)\ \ i = 1, ..., J$, along their respective components of the boundary.

Values of $\vec{U}, v, \vec{\nabla} P, \rho$ are then given along the vector grid points, while we use the scalar grid points to create the desired basis of divergence-free vectors from a set of scalar fields.

As a final remark about discretization, we need to define discretized gradient and divergence operators. We need the gradient operator to be such that it takes a scalar field with values at the scalar grid points and maps it to a vector field with values at the vector grid points. In particular, we want to define the two operators so that they satisfy the discretized version of Gauss' theorem:

$$\iint \phi \vec{\nabla} \cdot \vec{v} dx dz = -\iint \vec{\nabla} \phi \cdot \vec{v} + \oint \phi \vec{v} \cdot \hat{n} ds \tag{3.8}$$

where ϕ is an arbitrary scalar from our scalar grid and $\vec{v}$ is an arbitrary vector from our vector grid.

The basis of divergence-free vectors can then be constructed, and once done so, we discretize the projection by taking the dot product of the problem we want to solve with the system of basis vectors, then integrating over our domain, yielding:

$$\Sigma_{s,t}\alpha_{s,t}\iint(1+\rho)\vec{\Psi}_{i,j}\cdot\vec{\Psi}_{s,t}dxdz+\oint P\vec{\Psi}_{i,j}\cdot\hat{n}=\iint\vec{v}\cdot\vec{\Psi}_{i,j} \tag{3.9}$$

It is from this equation that our code discretizes the projection operator, thus leading to the numerical method needed to solve our equations and create our simulations. The exact details of how this works beyond this point become extremely technical and well-warranted of a discussion all their own. Hence, having covered the fundamentals, we leave our discussion here. Consult [57] and its references for the discussion in full.

To conclude, we think about how we advance time in our code. Variable time-stepping is used in our simulation, with $\vec{U}$ and ρ being calculated simultaneously at each time step. We impose a CFL condition to ensure that fluid parcels do not travel further than half a grid cell per time step. We need a second restriction as well (preferably related to the speed of propagation of our waves), so we also choose to specify a maximum allowable time step. Then, given the values of $\vec{U}, v, \rho$ at time step t_n, the goal is then to compute their values at time $t_{n+1} = t + \delta t_n$. This procedure and its particulars are described in detail by [57], and we will not repeat their derivation here.

3.2 Model

We use a 2D-model with a fixed length, L, in the horizontal (x) direction. The rigid lid approximation is used at the surface boundary, i.e. we assume that the ocean we are modelling has a fixed and immobile surface. Such an approximation is used since we are interested in internal motions in our study, and any vertical displacements of the surface would be minuscule in comparison to vertical displacements in the interior of the fluid body. Not only does such an assumption simplify our model, but it also enables us to eliminate fast-moving surface gravity waves, allowing us to employ larger time steps.

With this in mind, in the vertical (z) direction, we set the surface to be along the line $z = 0$. As for the bottom, we employ a seafloor bathymetry $z = -H + h(x)$, where $h(x)$ is a function which we will discuss in more detail

later in this section. Note that for convenience we generally choose the $h(x)$ such that it has a minimum at $-H$, where H is the maximum water depth. Bathymetries chosen are subject to the condition $h(x) < H$, i.e. the seafloor does not breach the ocean surface. Hence, in conclusion, we solve the model on the domain [57]:

$$R = \{(x, z) | x_l \leq x \leq x_r = L - x_r, \quad h(x) \leq z \leq 0\}. \tag{3.10}$$

Finally, we note that the model employs a variable grid, such that we are capable of controlling the size of the grid cells in both the horizontal and vertical directions. Additionally, in the horizontal, we are capable of stretching the left and right boundaries, such that we have a central region with regularly spaced grid cells, and to the left and right of that, regions of stretched grid cells. The size of the cells in the central region, d_x, takes the form:

$$d_x = \frac{L}{I - I_l - I_r} \tag{3.11}$$

where L is the length of the horizontal domain, I is the number of grid points in the central region, and I_l, I_r are the number of grid points in the stretched left/right regions, respectively. If $I_{l,r} = 0$, the grid is uniformly spaced in the horizontal. To create stretching, when stretching needs be employed, this parameter d_x is scaled on either side of the uniform grid (in our case, by a factor of 15). The centre of this increase occurs a set number of grid points out (in our case, 400), and it occurs over a set number of grid points (we use 600). Note that these parameters could vary within the code, but we choose to keep them fixed across all runs with stretching for uniformity's sake. No such stretching is employed in the vertical domain.

With this out of the way, we now take a moment to discuss the basic setup. Our model simulates tidal flow over an isolated ridge in the presence of a steady along-ridge background current. Simulations are initiated at the maximum flood tide via setting the initial fields as:

$$(u, v, w) = \Big(\frac{Q}{H - h(x)}, 0, -\frac{Qh'(x)}{(H - h(x))^2} z\Big) \tag{3.12}$$

$$\rho = \rho(z) \tag{3.13}$$

where $Q = U_{max} H$ is the peak volume flux, U_{max} is the barotropic tidal amplitude in deep water far from the ridge, and ρ is an arbitrary prescribed density. Both boundaries in the horizontal direction are open, and forcing occurs at the left boundary subject to the condition:

$$\frac{\partial u}{\partial t} = -\omega_T U_{max} \sin(\omega_T t) \tag{3.14}$$

where ω_T is the tidal frequency (in our case this will be the K_1 tidal frequency). The code integrates the given density field along the lines of the thermal wind relation (integrating starting from the seafloor up to any given point in z, setting the velocity at the seafloor to be zero) to solve for the initial background current, $V(x)$. The initial tidal phase is set to $\frac{\pi}{2}$ radians [68].

To define a density for use in our initialization, we employ the following definition:

$$\rho(x,z) = -\frac{N^2}{g}\tilde{z}(x,z) \tag{3.15}$$

$$\tilde{z}(x,z) = z + \zeta(z)hvar(x) \tag{3.16}$$

$$F = F(x, x_0, \lambda_x) \tag{3.17}$$

$$G = G(z, z_0, \lambda_z) \tag{3.18}$$

$$\zeta(z) = \zeta_{max}F \tag{3.19}$$

$$hvar(x) = hvar_{max}G \tag{3.20}$$

where F, G are arbitrarily chosen functions of z and x, $\zeta_{max}, hvar_{max}$ are the maximum values of the perturbations in z and x, z_0, x_0 control the location of the perturbations, and λ_z, λ_x their respective widths. N and g are the buoyancy frequency and acceleration due to gravity, set at $N^2 = 1 \times 10^{-6} s^{-1}$ and $g = 9.81 m/s^2$, respectively. Note that this value of N is set for the region sufficiently far outside of the background current where $\tilde{z} \approx z$. Inside the background current, the buoyancy frequency would dynamically change with the stratification. However, $hvar$ and ζ will generally be chosen to have forms such that far from x_0 and Z_0 (to the left/right, above/below), respectively, their respective rates of change would be approximately zero, and it is in such regions of minimal change in stratification that we will employ the constant N^2 value we mentioned here.

Test cases were be created by varying in particular the parameters of ζ and $hvar$. Specifics about and results from these test cases will be discussed in Chapter 4. Broadly speaking, however, test cases will be organized into families based on the chosen structure of $hvar$, further broken down into individual cases based on the magnitude of λ_x (the reason for this to be discussed in section 3.4). Note that individual cases with similar λ_x values may have some differing parameters, such as location of the perturbation x_0, length of run, and so on.

Two specific bathymetries, h, were chosen for our waves to propagate over. The first used was fourth-order Gaussian of the form:

$$h = A\exp(-(\frac{x}{w})^4)$$

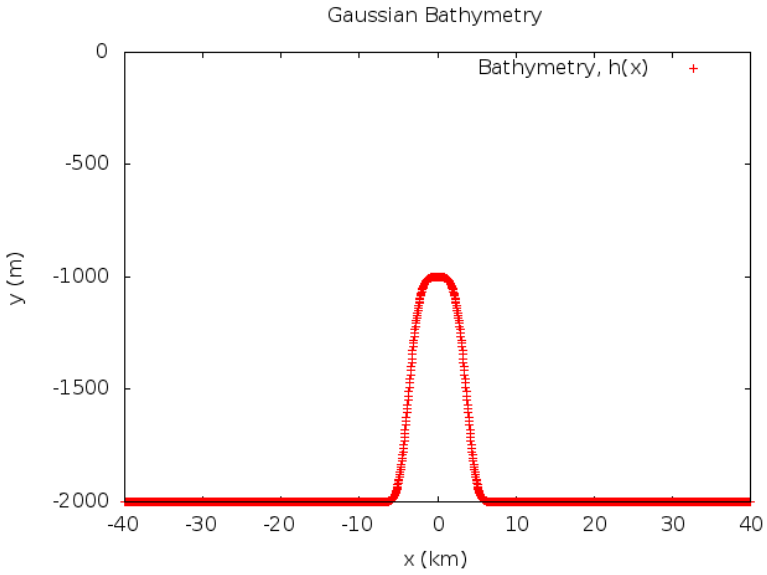

Figure 3.1: The fourth-order Gaussian bathymetry. The x and z axes represent distance in the horizontal and vertical directions, in kilometers and meters, respectively.

where A is an amplitude factor and w is a width parameter. For our cases, unless otherwise listed, for this bathymetry we fix (across all simulations, unless otherwise noted) $A = 1000m, w = 4000m$.

See Figure 3.1 for a visual reference for the fourth-order Gaussian bathymetry used. Such a bathymetry is commonly used in similar studies, though it is sometimes desirable to further control the steepness of the bathymetry's slopes/edges. For example, having shallower slopes could help leave a broader area for breaking, a desirable trait to help minimize inertial instabilities. To that end, a second bathymetry was also used. In this bathymetry, the seafloor ridge is broken up into three specific regions, each with its own defined length, steepness, and curvature. This kind of bathymetry allows for smooth, controllable transitions between its parts, and for more precise shaping of the ridge, at the cost of simplicity.

Mathematically, this bathymetry is defined as follows:

$$h(x) = 0.5\{s_1[\int(1+\tanh(\frac{x-x_1}{d_1}))dx] - (s_2-s_1)[\int(1+\tanh(\frac{x-x_2}{d_2}))dx] \\ -(s_3-s_2)[\int(1+\tanh(\frac{x-x_3}{d_3}))dx] + (s_4-s_3)[\int(1+\tanh(\frac{x-x_4}{d_4}))dx]\} \tag{3.21}$$

where once again, x is the horizontal distance parameter. As for the new parameters, the x_i, $i = 1, 2, 3, 4$, are the points at which the slope changes, the s_i are the value of the slopes in each region, and the d_i determine the roundedness of each transitory region. So, for example, the slope begins at zero, then smoothly increases to s_1 at x_1, with a curvature defined by d_1. It then does the same for the second transition region, and so on until at last it transitions to the fourth slope, then back down to zero. Note that the factor of 0.5 in front of the bathymetry is due to the derivative of the integral of $1+\tanh(x)$ having a maximum of 2, and we want to normalize this to 1. Note that we can choose the length of the flat top region (L_{top}) in-between x_2 and x_3 as we see fit, and we can introduce an amplitude parameter A like we did with the Gaussian as well.

The values for each of our chosen parameters are as follows:

$$
\begin{aligned}
d_1 &= d_4 = 10000 \\
d_2 &= d_3 = 2000 \\
s_1 &= 0.04 = -s_3 \\
s_2 &= s_4 = 0 \\
L_{top} &= 10000 \\
x_3 &= 0.5 L_{top} = 5000 = -x_2 \\
x_4 &= x_3 + \frac{A}{s_1} = x_3 + \frac{1000}{0.04} = 30000 = -x_1
\end{aligned}
$$

In general, parameters were chosen to allow for smooth, slow transitions between different of different slopes, reducing the likelihood that waves might overturn on sharp transitory regions. With the exception of top length (where explicitly stated, particularly in Chapter 4.3.2), assume that these parameters remained constant across across all simulations employing this type of bathymetry. For a visual reference, consult Figure 3.2.

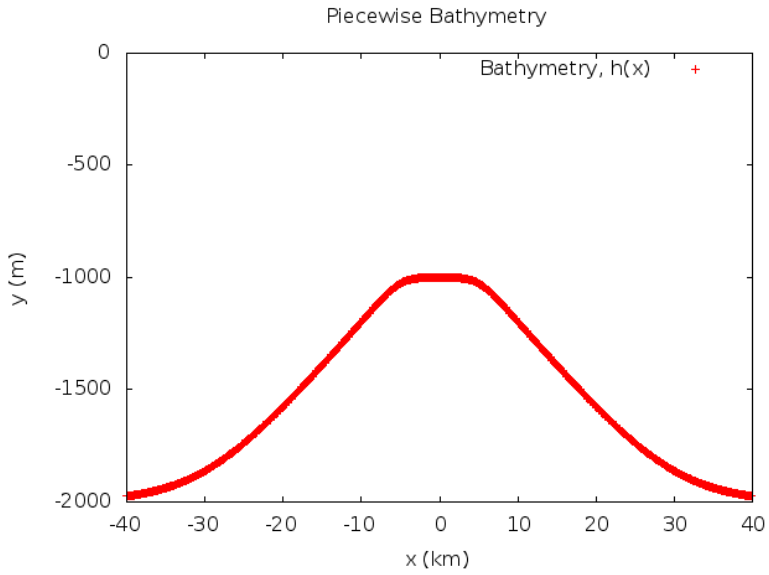

Figure 3.2: The second bathymetry used. Note the shallowness of its sides compared to the relative steepness of the Gaussian bathymetry. The four regions as mentioned previously can be seen here - a concave region on the far left, a convex region left of centre, and their mirror images on the right (though in general, these four regions do not need to have pairwise symmetry). Each of these regions can be individually shaped. The x and z axes denote spatial distance in kilometers and metres, respectively.

3.3 Inertial Instability

Inertial instability, called such due to acceleration being the key driver of particle displacement in systems experiencing it, occurs in a stratified rotating fluid when a fluid particle is displaced from its point of origin and continues to move away from it. Such instability can be catastrophic in nature - should one particle experience this, there is no reason others should not as well. The end result of this can be overturning, mixing, and chaos entering the fluid system. [59]

With our model established, we want to establish a means of checking for inertial instabilities in our background state. We want to ensure that these are not observed in our data - not only are they not the instability we are looking for, but they can also introduce breaking and chaos into our simulations, neither of which are desirable. In ensuring we do not have initial instabilities, we are also capable of developing a natural means of iterating on parameters for the test cases we will develop in the subsequent sections.

3.3.1 Instability Criterion

Using [59] once again as our reference, we will develop a criterion for checking for inertial instability.

Let us assume we have an inviscid fluid undergoing steady flow, with all variation occurring across the 2D xz-plane. Let the flow be in thermal wind balance, with shear velocity $v = v(x, z)$ in an equilibrium with slanted stratification $\rho = \rho(x, z)$ (note that this stratification is used for our derivation here, and is the physical, dimensional density; it is not quite the same scaled stratification as in our Boussinesq equations). For such a flow to exist, it must satisfy the conditions of hydrostatic balance and geostrophy:

$$0 = -\frac{1}{\rho_0}\frac{\partial P}{\partial z} - \frac{g}{\rho_0}\rho \tag{3.22}$$

$$-fv = -\frac{1}{\rho_0}\frac{\partial P}{\partial x} \tag{3.23}$$

We can combine these two equations to eliminate pressure terms and get a single equation for thermal wind balance:

$$f\frac{\partial v}{\partial z} = -\frac{g}{\rho_0}\frac{\partial \rho}{\partial x} \tag{3.24}$$

From the characteristics of the flow we have defined above, we are capable of defining the following three quantities. Each will take the form and units of a frequency squared, and we will use them again momentarily.

$$N^2 = -\frac{g}{\rho_0}\frac{\partial \rho}{\partial z} = \frac{1}{\rho_0}\frac{\partial^2 P}{\partial z^2} \tag{3.25}$$

$$F^2 = f(f + \frac{\partial v}{\partial x}) = f^2 + \frac{1}{\rho_0}\frac{\partial^2 P}{\partial x^2} \tag{3.26}$$

$$fM = f\frac{\partial v}{\partial z} = -\frac{g}{\rho_0}\frac{\partial \rho}{\partial x} = \frac{1}{\rho_0}\frac{\partial^2 P}{\partial x \partial z} \tag{3.27}$$

We note that N^2 is of the form of the square of the familiar buoyancy (Brunt-Väisälä) frequency and that F^2 takes the form of the square of the effective Coriolis frequency we explored in section 2.3.

To examine changes in our system, let us perturb our base flow with the introduction of time dependence and velocity components u and w (in the x and z directions, respectively). We continue to assume no variations in the y direction, non-hydrostaticity, and we will approximate motion to the f-plane.

$$\frac{Du}{Dt} - fv = -\frac{1}{\rho_0}\frac{\partial P}{\partial x} \tag{3.28}$$

$$\frac{Dv}{Dt} + fu = 0 \tag{3.29}$$

$$\frac{Dw}{Dt} = -\frac{1}{\rho_0}\frac{\partial P}{\partial z} - \frac{g}{\rho_0}\rho \tag{3.30}$$

where $\frac{D}{Dt}$ denotes a material derivative. Suppose we now choose to observe a single particle in our flow. It has coordinates that change in time as it moves with the flow, $[x(t), z(t)]$. Its horizontal and vertical velocity are given by:

$$u = \frac{dx}{dt} \tag{3.31}$$

$$w = \frac{dz}{dt} \tag{3.32}$$

With these, we can transform the second of our perturbed equations to yield:

$$\frac{dv}{dt} + f\frac{dx}{dt} = 0 \tag{3.33}$$

Given that we assume a constant Coriolis frequency, it follows via an integration in time that $v + fx$ is a constant in our system. Hence, should the particle

undergo a change in position Δx, it experiences a change in transverse velocity Δv so that:

$$\Delta v + f\Delta x = 0 \tag{3.34}$$

As we did with the second perturbation equation, we can eliminate u and w from our first and third equations to get:

$$\frac{d^2x}{dt^2} - fv = -\frac{1}{\rho_0}\frac{\partial P}{\partial x} \tag{3.35}$$

$$\frac{d^2z}{dt^2} = -\frac{1}{\rho_0}\frac{\partial P}{\partial z} - \frac{g}{\rho_0}\rho \tag{3.36}$$

Note that here the pressure function P is an arbitrary function of x and z and could be complicated.

Now, we would like to linearize these equations. Suppose that we perturb the fluid particles from their initial positions by a small amount (dependent on time), i.e. $x(t) = x_0 + \Delta x(t)$, $z(t) = z_0 + \Delta z(t)$. We will neglect effects in y, as they do not contribute to the dynamic balance. We must also make a few assumptions. Assuming incompressibility, a change in a particle's position causes no corresponding change in a particle's density. As the particle moves, it leaves equilibrium, experiencing the force of buoyancy in the vertical direction and having its geostrophy broken in the horizontal. Such forces would appear as changes in the local pressure gradient, and we can express these small perturbations via a Taylor expansion:

$$\frac{\partial P}{\partial x}|_{(x+\Delta x,z+\Delta z)} = \frac{\partial P}{\partial x}|_{(x,z)} + \Delta x\frac{\partial^2 P}{\partial x^2}|_{(x,z)} + \Delta z\frac{\partial^2 P}{\partial x\partial z}|_{(x,z)} \tag{3.37}$$

$$\frac{\partial P}{\partial z}|_{(x+\Delta x,z+\Delta z)} = \frac{\partial P}{\partial z}|_{(x,z)} + \Delta x\frac{\partial^2 P}{\partial x\partial z}|_{(x,z)} + \Delta z\frac{\partial^2 P}{\partial z^2}|_{(x,z)} \tag{3.38}$$

We can subtract off the base state to yield equations for the perturbed quantities:

$$\frac{d^2\Delta x}{dt} - f\Delta v = -\frac{\Delta x}{\rho_0}(\frac{\partial^2 P}{\partial x^2}) - \frac{\Delta z}{\rho_0}(\frac{\partial^2 P}{\partial x\partial z}) \tag{3.39}$$

$$\frac{d^2\Delta z}{dt} = -\frac{\Delta x}{\rho_0}(\frac{\partial^2 P}{\partial x\partial z}) - \frac{\Delta z}{\rho_0}(\frac{\partial^2 P}{\partial z^2}) \tag{3.40}$$

where we have used $\Delta v = -f\Delta x$ in the first equation. In the first equation, we see a force imbalance due to Coriolis effects and changing pressure gradients in the horizontal, producing a horizontal acceleration. We see something similar with a vertical acceleration due to changing pressure gradients in the vertical

(which effects new buoyancy forces upon our particle). Both of these equations are linear, so we may now look for solutions for them, which will be of the form:

$$\Delta x = A\exp(i\omega t) \tag{3.41}$$
$$\Delta z = B\exp(i\omega t) \tag{3.42}$$

A real value of ω would produce stable sinusoidal oscillations about an equilibrium point. It therefore follows that if we are looking for instability, we want to characterize under what conditions a complex ω occurs, and particularly, when ω is complex with a negative imaginary part. Such an ω would be conducive to exponential growth, thereby causing our particle to leave its position and never return.

If we substitute our solutions into the 2nd-order equations we have derived for Δx and Δt, we get a 2x2 system for the values of our amplitudes A and B:

$$(F^2 - \omega^2)\Delta x + fM\Delta z = 0 \tag{3.43}$$
$$fM\Delta x + (N^2 - \omega^2)\Delta z = 0 \tag{3.44}$$

To get a non-zero solution, we require:

$$(F^2 - \omega^2)(N^2 - \omega^2) = f^2M^2 \tag{3.45}$$

which we can solve a quadratic in ω^2 with roots:

$$\omega^2 = \frac{F^2 + N^2 \pm \sqrt{(F^2 - N^2)^2 + 4f^2M^2}}{2} \tag{3.46}$$

From this equation, we are capable of deriving our criteria for instability to occur.

Firstly, consider the case of no rotation, i.e. $F^2 = f^2M^2 = 0$, and assume that N^2 is non-zero. Then,

$$\omega^2 = \frac{N^2 \pm N^2}{2} = N^2, 0 \tag{3.47}$$

So long as $N^2 \geq 0$, it follows that ω is universally real (this corresponds to density increasing in a downward direction; the alternative is gravitational instability).

Secondly, consider the case of a pure shear flow (horizontally sheared flow $V(x)$), i.e. $N^2 = f^2M^2 = 0$, and assume non-zero F^2. Then,

$$\omega^2 = \frac{F^2 \pm F^2}{2} = F^2, 0 \tag{3.48}$$

So long as $F^2 \geq 0$, we have a universally real ω. Such values of F^2 correspond to $f(f + \frac{\partial v}{\partial x}) \geq 0$, which means f takes the same sign as the term in brackets (or, as we have observed, a non-negative effective Coriolis frequency). The alternative would be pure inertial instability.

Finally, consider the general case. Given what we have seen so far, we observe that the transition from stability to instability occurs at $\omega^2 = 0$, meaning that for instability not to occur, we require:

$$F^2N^2 - f^2M^2 \geq 0. \tag{3.49}$$

Putting this together with our previous conditions, we conclude that in order to have no inertial instability, we require:

$$F^2 \geq 0 \tag{3.50}$$

$$N^2 \geq 0 \tag{3.51}$$

$$F^2N^2 - f^2M^2 \geq 0 \tag{3.52}$$

Note that we also need to enforce $N^2 > 0$ to avoid any gravitational instabilities. It is this trio of conditions that we will use to monitor for instabilities in our model. To remark on the physical interpretation of this last condition, it refers to lines of constant geostrophic momentum $(v + fx)$ needing to be steeper than lines of constant density in our system in order to maintain stability. [59] presents a further discussion of this interpretation, including diagrams modeling lines of stability.

As a final remark, we could explore inertial instability again through the lens of potential vorticity. A detailed discussion of this can be found in [69]. Instead of going through their whole derivation, though, we will just quote the key result. Note that this formulation is in terms of y and z instead of our x and z.

If we define the Ertel potential vorticity as:

$$Q_E = -[2\vec{\Omega} + \vec{\omega}] \cdot \frac{g}{\rho_0}\vec{\nabla}\rho \tag{3.53}$$

$$Q_E = (f - \frac{\partial u}{\partial y})[N^2 - \gamma(\gamma + \frac{\partial u}{\partial z})] - f(\gamma + \frac{\partial u}{\partial z})^2 \tag{3.54}$$

where $\vec{\Omega}$ is Earth's rotation vector, ω is the vorticity, γ is the horizontal Coriolis parameter (we neglect this in our model, but it is included for completeness) and ρ, u are the basic, unperturbed density/velocity of the fluid system. Then for no inertial instability in our system, we require:

$$fQ_E \leq 0 \tag{3.55}$$

Through some manipulation (that we omit for brevity), this condition can be brought into a similar form of the one we developed previously (with a sign difference altering the inequality). Hence, we see multiple approaches are capable of bringing us to this same condition for stability.

3.3.2 Varying Parameters

Now that we have a criterion by which we can determine if our flow is unstable, it is easy to explore how changes in the parameters we use to define it may affect its stability. In turn, we can use this to explore how to optimally change our parameters to maximally increase the permissible regions of PSI with a changing effective Coriolis frequency while still maintaining no inertial instability.

To demonstrate this, we will use our established stability criteria to explore how our system might vary with the thickness of the changing stratification regions in x and z. In particular, we will examine the condition $F^2N^2 - f^2M^2 \geq 0$ using inputs of the form we established in section 3.2.

For the sake of demonstration, suppose we set:

$$\zeta(z) = A(1 + \tanh(\frac{z - z_0}{\lambda_z})) \tag{3.56}$$

$$hvar = B(\tanh^2(\frac{x - x_0}{\lambda_x})) \tag{3.57}$$

$$\rho(x, z) = -\frac{N_b^2}{g}[z + AB(1 + \tanh(\frac{z - z_0}{\lambda_z}))(\tanh^2(\frac{x - x_0}{\lambda_x}))] \tag{3.58}$$

where we use N_b to distinguish between the constant we might use in our model versus the N^2 we used in section 3.3, and A and B are constant-valued parameters for amplitude. Note that while these values of ζ and $hvar$ might not be exactly the same as the ones we will use, they are close enough to show the same behaviour as our to-be-chosen setups, while simple enough to demonstrate the dependencies without excessive computation.

Given that we will be working with density in the code, we want to convert all of the values in our condition into a form expressed purely in terms of density:

$$N^2 = -\frac{g}{\rho_0}\frac{\partial \rho}{\partial z} \tag{3.59}$$

$$fM = f\frac{\partial v}{\partial z} = -\frac{g}{\rho_0}\frac{\partial \rho}{\partial x} \tag{3.60}$$

$$F^2 = f(f + \frac{\partial v}{\partial x}) = f(f - \frac{g}{\rho_0 f}\int_0^z \frac{\partial^2 \rho}{\partial x^2}\lambda_z) \tag{3.61}$$

Plugging in our given form of ρ, let us consider how each of these terms behaves. We will omit the differentiated/integrated functions by use of ellipses, as the terms we want to analyze are outside of those functions.

$$\begin{aligned} N^2 &\sim \frac{N_b^2}{\rho_0}[1 + \frac{AB}{\lambda_z}(...)] \\ f^2M^2 &\sim \frac{f^2N_b^4}{\rho_0^2}\frac{4AB}{\lambda_x^2}(...) \\ F^2 &\sim f^2 + \frac{N_b^2}{\rho_0}\frac{AB(\lambda_z)}{\lambda_x^2}(...) \\ F^2N^2 &\geq f^2M^2 \end{aligned}$$

With our inequality here as a reminder, from these results, we can make a few notes.

1. The LHS (F^2N^2) will be highly dependent on λ_x for small λ_x, and will roughly balance with the RHS (f^2M^2). However, for large λ_x, terms with it in the denominator on the LHS will become significantly smaller, thus the LHS to have its largest contribution in magnitude come from terms on the order of f^2. The term with f^2 on the RHS has λ_x^2 on the bottom, so in the large λ_x regime, it could not see the same magnitude as the LHS term that does not the λ_x^2 denominator. We would thus see a larger LHS in such a regime (larger being a relative term - values involved in this instability criterion are ultimately extremely small; more on this throughout Chapter 4). Hence, one key parameter we will focus on is λ_x - ensuring that it is large enough for the LHS to be greater than the RHS, satisfying the inequality.

2. We notice that λ_z has the ability to impact the magnitude of terms on the LHS as well (particularly when it multiplies terms on the order of f^2 but not λ_x^2), so this parameter can also be used to ensure stability.

3. We see the amplitudes for *hvar* and ζ, A and B, appearing on both sides, but the LHS will have their squares in one of its terms. Hence, these amplitudes also mark a key point for varying parameters, and we will ensure that they are chosen large enough to ensure stability while also maintaining their relevancy to actual oceanic simulations.

To recap, our key parameters for modulation are the horizontal and vertical distances over which the disturbances occur, λ_x and λ_z, along with the magnitude of the disturbances in the horizontal and vertical, A and B. By looking at our stability condition, we see that these values have the potential to yield the largest possible impacts upon the potential stability of our simulated waves, and hence, they will serve as the key parameters we modulate to create different test cases. Note that while we only looked at one type of stratification in our example, this type of analysis indeed works out to yield the same result for all of these stratifications we intend to employ (see Section 4 for all of these), and the varying of parameters remains universal across all of our test cases.

Chapter 4

Results and Discussion

Note that for all cases, we set the Coriolis frequency to $f^2 = 1.6 \times 10^{-9}$ s^{-2} (corresponding to a latitude of 15.92°N) and $N^2 = 1.0 \times 10^{-6}$ s^{-2}. Recall that the critical value of f_{eff}^2 in order for parametric subharmonic instability to occur is the square of half of the K_1 tidal frequency, or $f_{eff}^2|_{crit} = 1.32987 \times 10^{-9}$ s^{-2}. Equivalently, for simplicity, we can say that the critical value occurs when $\frac{f_{eff}}{\sigma} = \frac{1}{2}$, where σ is the K_1 tidal frequency. Note that all instability criterion plots in this chapter will plot the value of the left-hand side of the inequality in Eq. 3.52 for the relevant case. For a table of all relevant cases in this chapter, consult Table A.1 in Appendix A.

4.1 Controls

Before examining relevant simulations, we illustrate a few controls used in our experiments.

4.1.1 No Current

The simplest test case that we can use as a control is one without any background current present.

For our "no current" case, we set the horizontal background current to zero, so that $\rho(x, z) = \rho(z)$, and run the simulation as we would in the presence of a background current. This control case was run on the piecewise-defined bathymetry (see Figure 3.2 for reference) for 10 K_1 tidal periods. The simulation has 100 gridpoints in the vertical direction and $I = 12000, I_l = I_r = 0$,

with an initial timestep of 14.95625 s. The value of this timestep is derived as follows. The code saves 48 times per K_1 tidal period, or once every 1794.5 seconds. Such a timestep therefore gives 120 time intervals between save points. Note that timesteps generally remain constant throughout simulations, unless prompted to change by events in the simulation (e.g. by the simulation failing in inertially unstable cases causing the timestep to rapidly increase in value). To avoid any possible confusion on this matter, we will give the timestep here as it was initially set in the code. We will adopt the abbreviation "NC", for "no current", in figures regarding this case.

In Figure 4.1, we have presented a series of plots depicting the x-component of the baroclinic tidal current (i.e., with the vertically averaged velocity removed). Note that in this thesis, we will not show the initial baroclinic tidal current, as it is always zero everywhere. As we can see from the plots, over the passing of tidal periods, while internal wave beams do form, they remain relatively straight over time. This lack of bending is what is to be expected from a case with no horizontal background current and a linear stratification. Without such a current, there is no means of shifting the effective Coriolis frequency the waves experience, nor is there any change in the the buoyancy frequency experienced by the waves. Indeed, the lack of such a current serves to keep f_{eff} and N constant. Hence, the beams remain straight, as expected. The importance of seeing this control is that we can confirm that our code can indeed render the most simple of simulations, and that no "phantom" currents/effects are being introduced at any point in the process. With this, we can be confident in the application of our code to more complex current structures.

4.1.2 Inertially Unstable Cases

Moving beyond the simplest case, another type of control we have is the family of cases where a current is present, but the inertial instability criterion is not met. It is important to understand what happens in cases such as these, in particular to see the contrast with cases where we do indeed meet the inertial instability criterion we established previously. Hence, we will take the time to present here a couple of cases with different background currents that failed to meet the required stability criterion.

We will illustrate a few examples of failed instability criterion runs from two different families of simulations. Note that the plots we will present here were taken at the end of each of these respective simulations. While intense

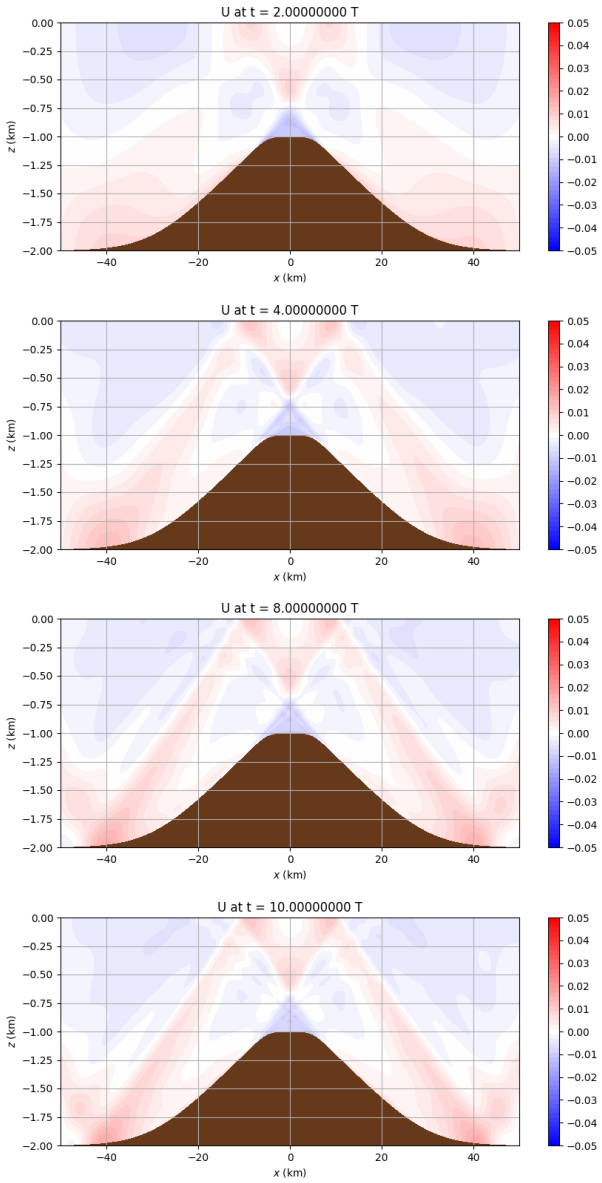

Figure 4.1: Plots of the x-component of the baroclinic current U for our NC case. Note that U here is shown as a function of x and z (both in km), while the colourbar shows its value (in m/s). Respectively, these plots show U at 2,4, 8, and 10 tidal periods.

waveforms and visible chaos will be visible on one, the other will appear mundane, almost normal. Some simulations, when subject to inertial instability, quickly undergo strong turbulence, amplifying in nature until it dominates the waveforms. Others, however, have not yet had this occur (it may do so in the future, or it may be currently too small to notice). Either way, it is important to observe both of these cases, as indeed, inertial instabilities start small and have the potential to grow to large amplitudes. Even the smallest instability, while seemingly unimportant, can indeed magnify into full turbulence and chaos.

With this discussion out of the way, we at last look at a few slices of unstable runs. Note that with each unstable run, we will present a value of the instability criterion. This value is equivalent to $F^2N^2 - f^2M^2$, or the left-hand side of our inequality if we moved everything onto one side. For a case to pass the criterion, this value would need to be greater than zero. For these cases, obviously, this will not be as such.

The first case we will look at is a simple one, but deceptively important nonetheless. For this test case, the following parameters are set:

$$\zeta(z) = 10[1 + \tanh(\frac{z + 1500}{50})] \tag{4.1}$$

$$hvar(x) = 0.25[1 + \tanh(\frac{x + 30000}{40000})]^2 \tag{4.2}$$

This case was run for 4 K_1 tidal periods, with 100 gridpoints in the vertical, $I = 12000$ and no stretching, an initial timestep of 14.95625 s, and the Gaussian bathymetry. The value of the inertial instability criterion's minimum for this case is -8.47×10^{-16} s^{-4}. We will adopt the abbreviation "U1PT", for "unstable 1 plus tanh", in figures regarding this case.

We first consider the plots presented in Figure 4.2. Recall for the density plots here and hereafter that we are plotting the dimensionless density used in our Boussinesq approximation, not the dimensional density proper. The instability criterion plot shows a large unstable region extending from almost $x = -30$ km to almost $x = 10$ km along the horizontal with the region reaching down about 600 m over-top of and to the left of the ridge, while shallowing out to the right of the ridge. This corresponds with the regions in which we see the most rapid/steepest density change on the initial density plot. The initial velocity plot also aligns with this, as we see regions of rapid change of density along the points where the background current at the surface has the steepest slopes. This is likewise the region we have the largest initial magnitude of the fluid velocity, $V(x, z)$. Looking further at Figure 4.3, we see instability quickly

seeping in over the top of the ridge on the left-hand side, in the same region we previously identified as unstable on the instability criterion plot. Taking these figures together, we see that even in a region that is majority stable, a pocket of instability is able to grow, and has the potential to begin propagating through the simulation, even with only a few tidal periods passing.

The next case we will look at is slightly less subtle, and will serve to demonstrate a bit of contrast with what we discussed previously. For this test case, the following parameters are set:

$$\zeta(z) = 0.5[1 + \tanh(\frac{z + 400}{100})] \tag{4.3}$$

$$hvar(x) = 1600\{0.5[1 + \tanh(\frac{x + 30000}{20000})] - 0.5[1 + \tanh(\frac{x - 30000}{20000})]\}^2 \tag{4.4}$$

The case was run for just over 7 K_1 tidal periods before it collapsed due to turbulence. It has with 200 gridpoints in the vertical; $I = 16000$, $I_l = I_r = 2000$; an initial timestep of 3.7390625 s; and the simulation was performed on the Gaussian bathymetry with half its usual amplitude (i.e. 500 m instead of the usual 1000 m). The value of the inertial instability criterion's minimum for this case is -1.31×10^{-15} s^{-4}. We will adopt the abbreviation "UDT", for "unstable difference (of) tanh (functions)", in figures regarding this case.

Note that this time, looking at the first plot in Figure 4.4 we see a different-looking region wherein the instability criterion is not met. It is centered over the ridge, extending to around $x = \pm$ 25km in the horizontal, with two deeper parts in the vertical on the outsides of the ridge (extending to around $z = -0.6$ km) and a shallow component (approximately 0.1km deep) in between them. Once again, we see spikes in instability where the density seems to change the most rapidly, looking at the centre and left/right edges of the instability criterion plot in comparison with the initial density. As the density starts changing more rapidly around $\pm$20 km, we see larger regions of instability, compared to the flatter region near the hill's centre. This correlates with the straight central region of the initial background current at the surface plot, and starts getting unstable right as the slope would be beginning to change (albeit still minutely at that point). We see a similar correlation with the regions wherein the initial vertical baroclinic current is at its largest.

Looking at Figure 4.5, however, we see the growing effects of an instability creeping into the top region at around 6 tidal periods, noting how the region into which they extend blends into the region of widening instability in the instability criterion plot in Figure 4.4. By just before 7.5 tidal periods, the

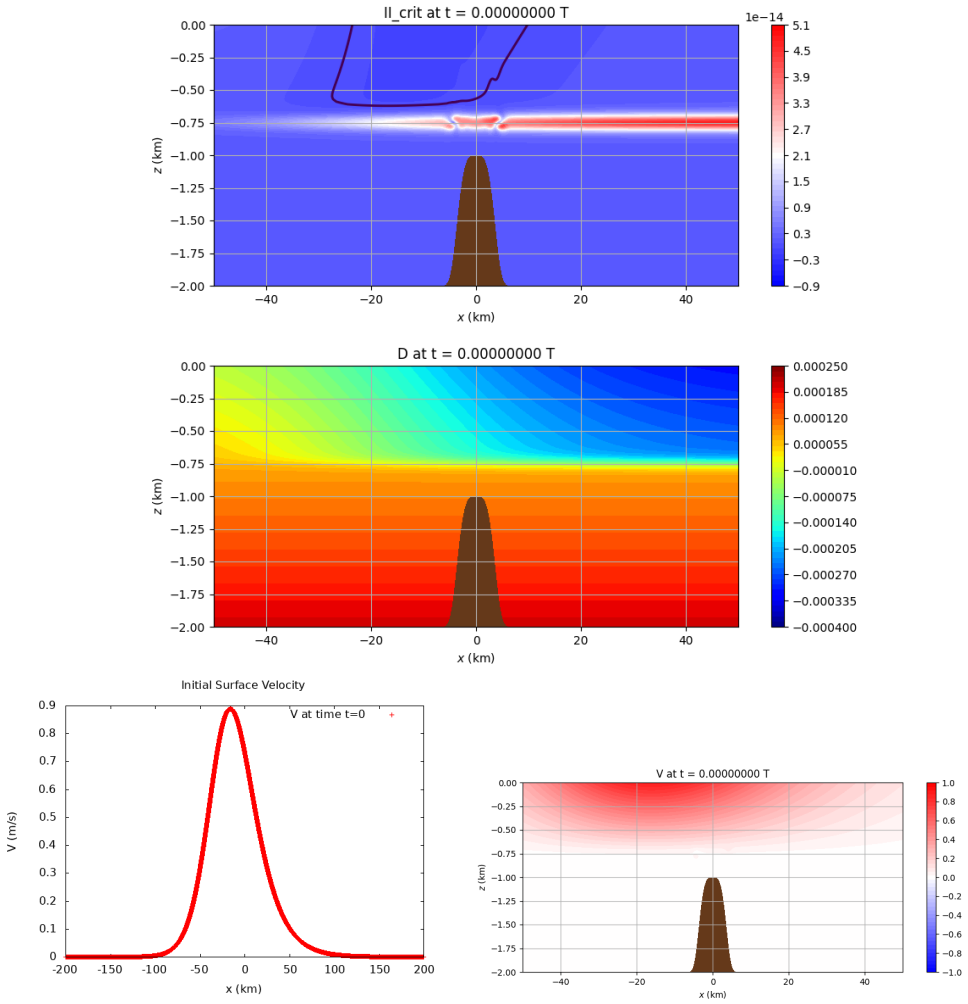

Figure 4.2: Top: A plot of the absolute value of the instability criterion for our U1PT case. The instability criterion, or II_{crit} on the plot, is shown as a function of x and z, with the colourbar showing its value (units of s^{-4}). The dark line shows the contour at which the criterion is zero; all the area above it is negative and unstable. Middle: The initial density profile for this case. The colourbar shows the magnitude of the density D, which is dimensionless. Bottom-left: A plot of the initial background current at the surface for this case. The red line shows the velocity at the surface, V, in units of m/s. Bottom-right: A plot of the initial background current V for this case. Note that V here is shown as a function of x and z (both in km), while the colourbar shows its value (in m/s).

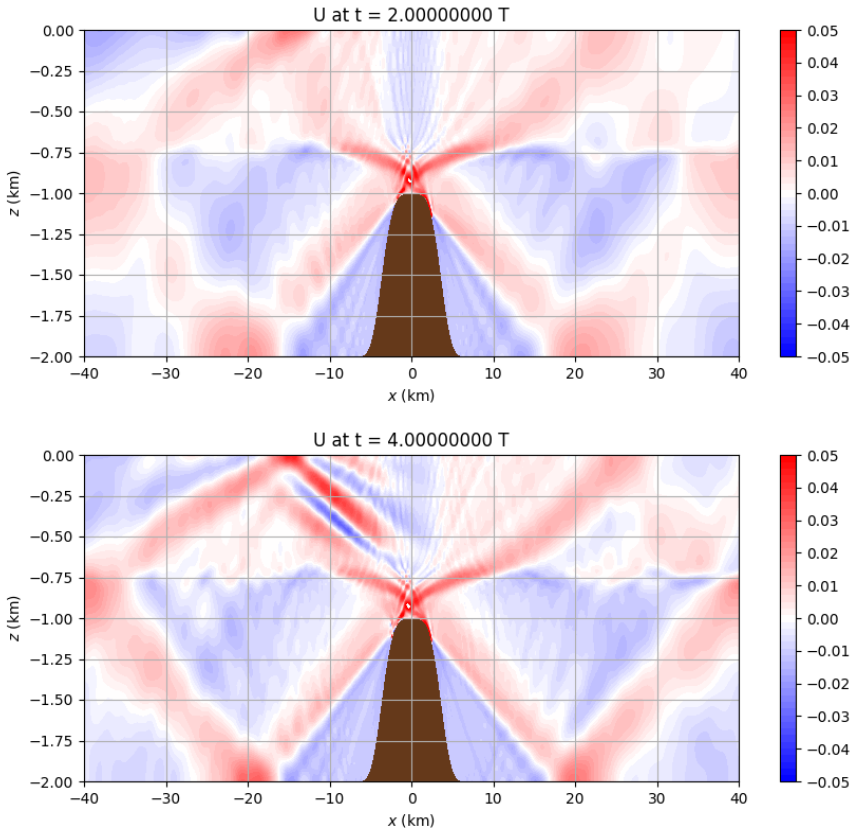

Figure 4.3: Plots of the x-component of the baroclinic current U for our U1PT case. Note that U here is shown as a function of x and z (both in km), while the colourbar shows its value (in m/s). Respectively, these plots show U at 2 and 4 tidal periods.

waves have broken down. While there is some semblance of the internal wave beam structure to the right of the ridge, in that region, and more noticeably, in the left, the effects of instability have grown such in magnitude that the range of the magnitude of our current colourbar fails to capture it. Indeed, this unstable effect, despite originating from a slim region, comes to dominate the waveforms extremely quickly, and has led to dramatic consequences.

Across a variety of cases consisting of different current structures and parameters, we can see the instability manifesting itself in many ways, all stemming from different failures to meet the stability criterion we have previously established. Indeed, while we have only seen a couple of examples of it here, there are many more ways for inertial instability to enter simulations and bring the effects of chaos along with it. It should be therefore thoroughly noted that satisfying the inertial instability criterion is essential for any successful simulation, and we have seen the ramifications of the contrary.

4.2 Summary of Test Cases

With our control cases examined, we can now observe successful test cases. In this section, we will present the results for a variety of background currents and bathymetries. Broadly speaking, we will organize results into families of different horizontal background current structures, and the differences among members of the same family will be discussed as they arise.

Note that the discussion presented here will be fairly general - the data included here is largely for illustrative purposes. One particularly successful case was chosen for in-depth study and analysis over all the rest, and we will go in-depth in its discussion in the next section.

4.2.1 Horizontal Background Density Field of the Form 1+tanh

We will begin by looking at the results of a successful case from a family of simulations using a $1 + \tanh$ structure in the horizontal background density field. For this run, the parameters are set as follows:

$$\zeta(z) = 1 + \tanh(\frac{z + 750}{100}) \tag{4.5}$$

$$hvar(x) = 400[1 + \tanh(\frac{x + 30000}{40000})]^2 \tag{4.6}$$

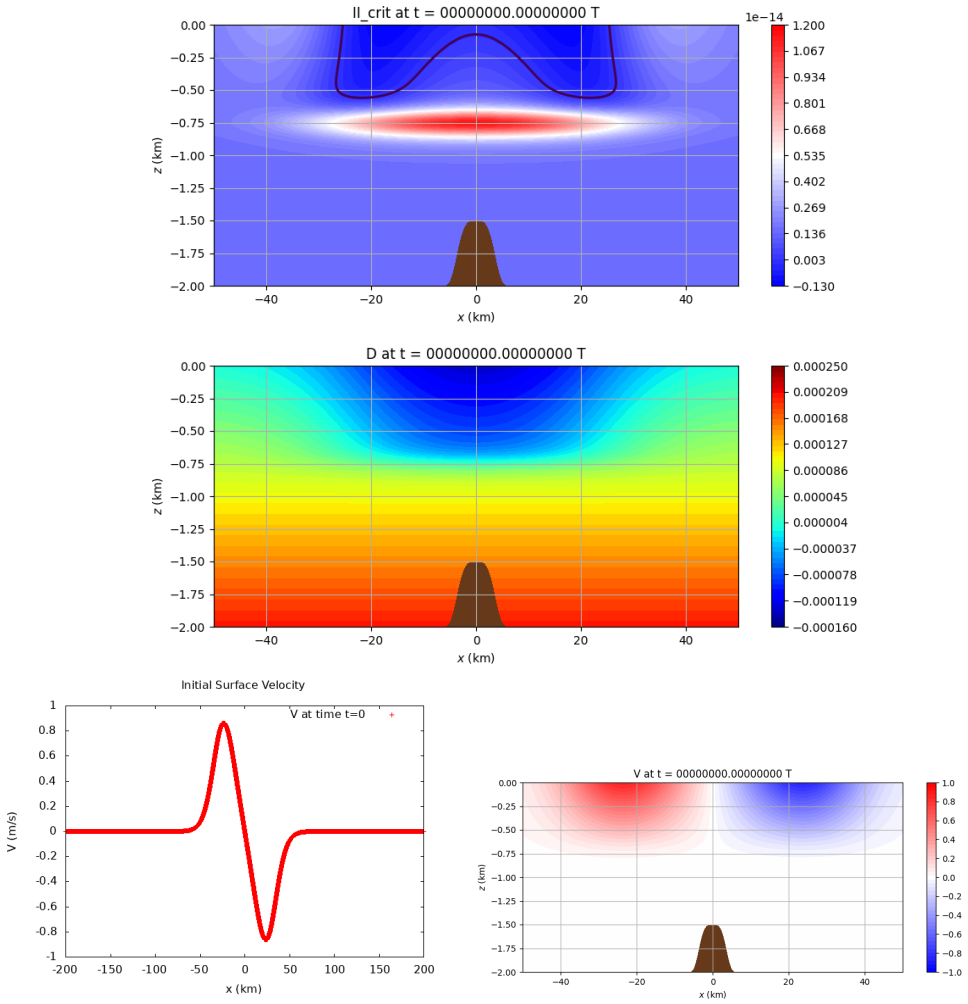

Figure 4.4: Top: A plot of the absolute value of the instability criterion for our UDT case. The instability criterion, or II_{crit} on the plot, is shown as a function of x and z, with the colourbar showing its value (units of s^{-4}). The dark line shows the contour at which the criterion is zero; all the area above it is negative and unstable. Middle: The initial density profile for this case. The colourbar shows the magnitude of the density D, which is dimensionless. Bottom-left: A plot of the initial background current at the surface for this case. The red line shows the velocity at the surface, V, in units of m/s. Bottom-right: A plot of the initial background current V for this case. Note that V here is shown as a function of x and z (both in km), while the colourbar shows its value (in m/s).

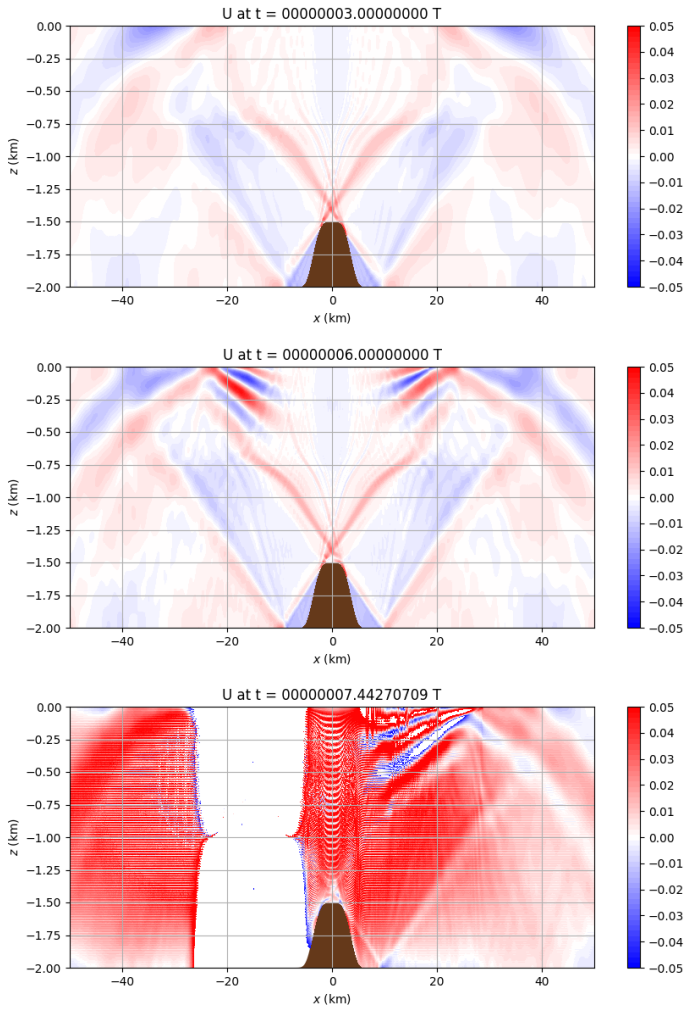

Figure 4.5: Plots of the x-component of the baroclinic current U for our UDT case. Note that U here is shown as a function of x and z (both in km), while the colourbar shows its value (in m/s). Respectively, these plots show U at 3 and 6, tidal periods, as well as the moment the run failed. Note that the large white space on the final plot shows values exceeding the range of the colourbar.

This case was run for 20 K_1 tidal periods, with 200 gridpoints in the vertical; $I = 16000$, $I_l = I_r = 2000$; an initial timestep of 3.7390625 s; and the simulation was performed on the Gaussian bathymetry with half its normal amplitude (i.e. 500m). We will adopt the abbreviation "1PT", for "1 plus tanh", in figures regarding this case.

For this test case, we have $f_{eff}^2|_{min} = 4.75 \times 10^{-10}$ s^{-2} and $f_{eff}^2|_{max} = 2.55 \times 10^{-9}$ s^{-2}. This gives $\frac{f_{eff}|_{min}}{\sigma} \approx 0.299$ and $\frac{f_{eff}|_{max}}{\sigma} \approx 0.692$.

In Figure 4.6, we have plots of the instability criterion, square of the effective Coriolis frequency, initial density profile, and initial background current. Of first note, our instability criterion in universally positive. This is essential for avoiding inertial instability, so it is important to confirm this. Looking at the effective Coriolis frequency (squared) plot, we see a region in the top 250 m of the water extending from atop the ridge to about 5 km on the left and over 20 km on the right wherein the effective Coriolis frequency's square drops below the critical value. Such a region corresponds with regions of rapid density change or changing slope in the initial velocity (visible in the initial background current plots), though we note the change is more controlled in simulations like this one (thus avoiding instability).

To remark on this run, looking at the current profiles in Figure 4.7 though universally stable with well-defined internal waves, we see minimal activity that might resemble PSI. We would be looking to see such activity originate in the region wherein the effective Coriolis frequency dips below the critical value, and this would be visible by internal wave beams with slopes much closer to the horizontal. That said, neither of these are visible here by the passing of 20 tidal periods. There are a combination of factors that might lead to this. The horizontal structure of the current produced the smallest possible effective Coriolis frequency in a small region near the surface of the water. The effects of PSI in such a region would be minimal, if any, and would be hard to see elsewhere. Additionally, the horizontal background current, set at a maximum of 0.01 m/s, may not be sufficiently strong to produce the effects we are looking for in this case. Finally, it could be possible that the effects would require further time to develop. Such facets could be explored in further experiments with this current structure; for our case study later, we will look at a structure in which more immediate results were present.

As an aside, looking at Figure 4.7, particularly in the 20 tidal periods we see the bending of internal wave beams throughout the figure, particularly between $x = \pm 20$ km and from $z = -1000$ m to $z = -500$ m. Not to be confused with PSI, this bending of the internal wave beams is caused by our

waves moving through a region of varying stratification, as induced by our background current. As the waves travel through this region, the presence of the background current alters the buoyancy frequency and effective Coriolis frequency that these waves experience. Though they remain at tidal frequency, if we recall our discussion of the slope of internal wave beams in Sections 2.2 and 2.3, the change of these other two parameters results in the slope of these beams changing, creating the effect of bending the wave beams as visible in Figure 4.7.

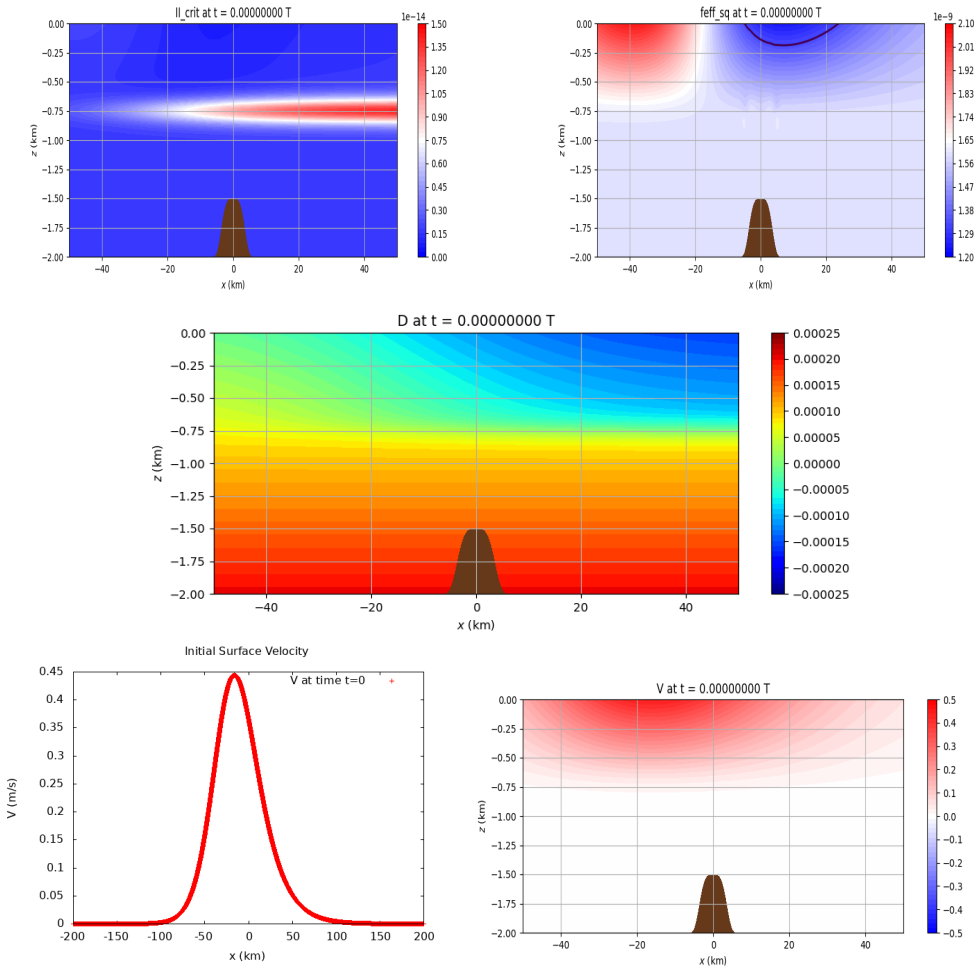

Figure 4.6: Top-left: A plot of the absolute value of the instability criterion for our 1PT case. The instability criterion, or II_{crit} on the plot, is shown as a function of x and z, with the colourbar showing its value (units of s^{-4}). Note the lack of a dark line - there are no zeroes, hence no instabilities. Top-right: A map of the value of the square of effective Coriolis frequency, f_{eff}^2. The colourbar shows its magnitude, in s^{-2}. The purple line denotes the critical value of f_{eff}^2. Middle: The initial density profile for this case. The colourbar shows the magnitude of the density D, which is dimensionless. Bottom-left: A plot of the initial background current at the surface for this case. The red line shows the velocity at the surface, V, in units of m/s. Bottom-right: A plot of the initial background current V for this case. Note that V here is shown as a function of x and z (both in km), while the colourbar shows its value (in m/s).

4.2.2 Horizontal Background Density Field of the Form sech

Another background structure examined over the course of our experimentation was that of a hyperbolic secant function for the horizontal background density field. Several runs of this type were performed, and we include one here for illustrative purposes.

For this test case, the following parameters are set:

$$\zeta(z) = 1 + \tanh(\frac{z + 400}{100}) \tag{4.7}$$

$$hvar(x) = 400\text{sech}^2(\frac{x + 10000}{40000}) \tag{4.8}$$

This case was run for 20 K_1 tidal periods, with 200 gridpoints in the vertical; $I = 16000$, $I_l = I_r = 2000$; an initial timestep of 3.7390625 s; and the simulation was performed on the Gaussian bathymetry with one-quarter its normal amplitude (i.e. 250 m). We will adopt the abbreviation "S", for "sech", in figures regarding this case.

For this test case, we have $f_{eff}^2|_{min} = 1.20 \times 10^{-9}$ s^{-2} and $f_{eff}^2|_{max} = 1.73 \times 10^{-9}$ s^{-2}. This gives $\frac{f_{eff}|_{min}}{\sigma} \approx 0.476$ and $\frac{f_{eff}|_{max}}{\sigma} \approx 0.571$.

Observing Figure 4.8, we again have plots of the instability criterion, square of the effective Coriolis frequency, initial density profile, and initial background current at the surface. Once again, we have a totally positive instability criterion. The effective Coriolis frequency squared plot shows us this time that we have a region about 125 m wide (vertically) at the top of the water extending from above the left side of the ridge to just over $x = -20$ km wherein the effective Coriolis frequency dips below the critical value. This aligns well with the region of most rapid density change and the fastest changing slope in the initial background current at the surface/steepest change(s) in gradient in the background current.

When we look at the current profiles in Figure 4.9 as was the case with the 1 + tanh structure, we have stability and proper internal wave beams, and indeed, while it is not impossible for PSI's effects to be occurring (as we do have a region in which the effective Coriolis frequency drops low enough for it to occur), if present, the results of this are very faint, and it would be difficult to confirm if they were indeed attributable to PSI in the first place. As for the reasoning behind why we fail to see conclusive PSI here, we face largely the same issues we observed in the previous case. Moreover, a

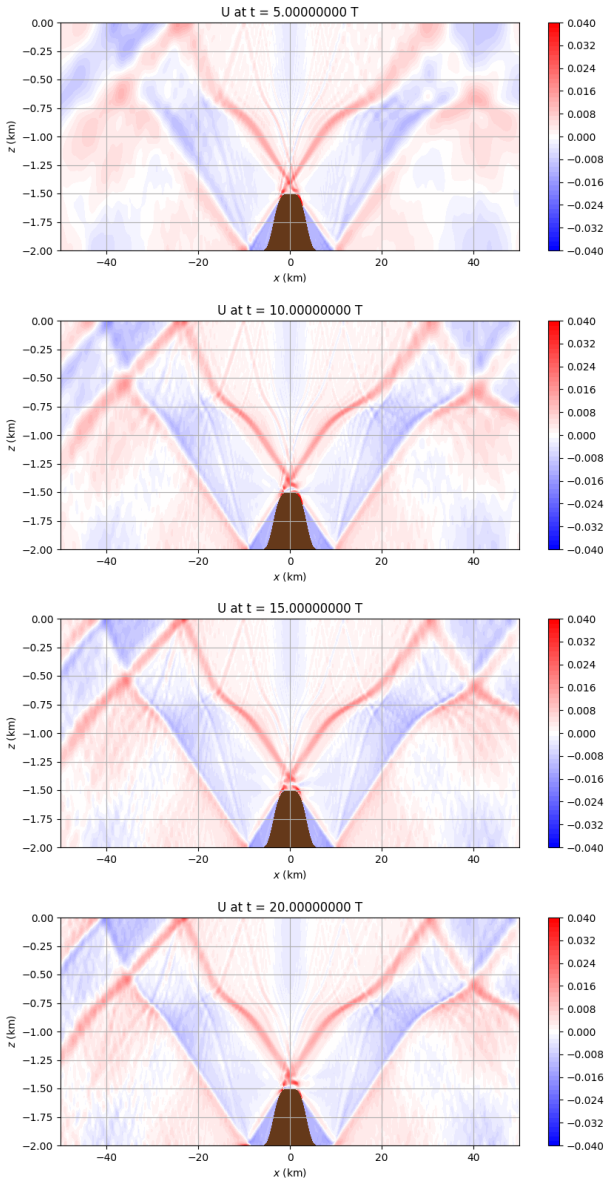

Figure 4.7: Plots of the x-component of the baroclinic current U for our 1PT case. Note that U here is shown as a function of x and z (both in km), while the colourbar shows its value (in m/s). Respectively, these plots show U at 5, 10, 15, and 20 tidal periods.

particular point of challenge with this structure was in achieving stability - in testing, this current required careful management of the amplitude of the ridge to achieve stability (the density plot's large dark-blue region of rapid change helps reflect this). By changing the size of the ridge, the regions in which we see gradients in velocity induced by sloshing over the ridge are are likewise changed, as are the magnitudes of gradient changes themselves. As the ridge's shape changes, the regions at which the internal waves are formed (and from whence they initially travel upward into the background current) are changed, and likewise the background current's relative location to the hill are altered. This is what leads to changes in the velocity gradients (as we have changing locations where we establish our bottom boundary condition of $V = 0$), and it affects the particularities of how the waves travel through (and thus, how they may experience) the background current. Thus, when we have instabilities, it can be helpful to reduce the size of the ridge to affect the absolute value of the instability criterion. Consequentially, a particularly small ridge was used in this case's experimentation, leading to stable, if not particularly dramatic or illuminating results. Indeed, the hill is so small here, the fluid leaving the ridge does not experience the background current for a significant vertical distance, and misses the region wherein the effective Coriolis frequency drops below the critical value in many places. While a smaller ridge can help to achieve stability, the size of a ridge and its ability to allow the fluid to enter the region wherein the effective Coriolis frequency is dropped below half of its critical value serves as a limiting factor for the development of PSI in such fluid systems. Nonetheless, runs such as this one help serve as good context and contrast for our later deep dive, so we still present it here for completeness.

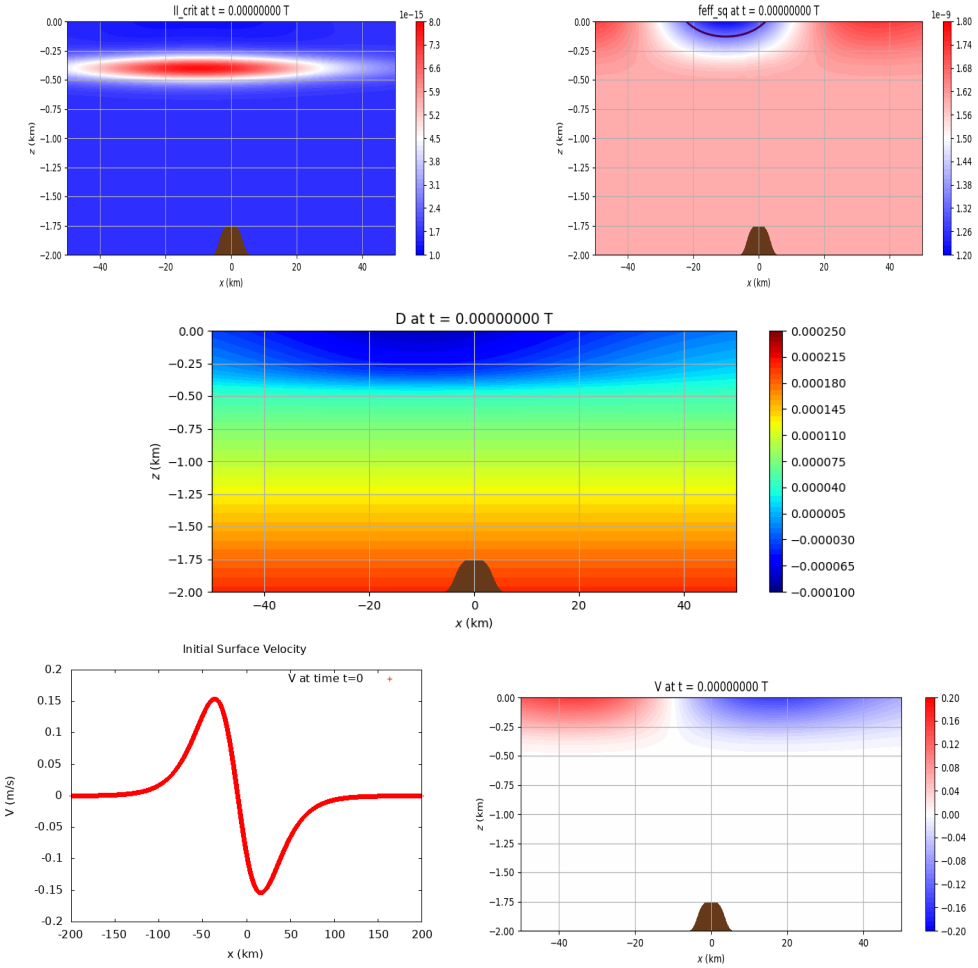

Figure 4.8: Top-left: A plot of the absolute value of the instability criterion for our S case. The instability criterion, or II_{crit} on the plot, is shown as a function of x and z, with the colourbar showing its value (units of s^{-4}). Note the lack of a dark line - there are no zeroes, hence no instabilities. Top-right: A map of the value of the square of effective Coriolis frequency, f_{eff}^2. The colourbar shows its magnitude, in s^{-2}. The purple line denotes the critical value of f_{eff}^2. Middle: The initial density profile for this case. The colourbar shows the magnitude of the density D, which is dimensionless. Bottom-left: A plot of the initial background current at the surface for this case. The red line shows the velocity at the surface, V, in units of m/s. Bottom-right: A plot of the initial background current V for this case. Note that V here is shown as a function of x and z (both in km), while the colourbar shows its value (in m/s).

4.2.3 Horizontal Background Density Field of the Form of a Difference of Tanh Functions

Finally, the last type of background density structure we examined was the difference of two hyperbolic tangents in the horizontal. Such a structure was particularly beneficial - it is particularly easy with this structure to place the region of steepest change directly over the ridge, leading to the region of lowered effective Coriolis being in the centre of our regime. We also have two large regions of changing slope given the shape of a difference of tanh functions current, and these changes can be easily manipulated to take place over broad regions via the adjustment of this pair of functions. While, with further experimentation, the other current types may indeed have had the ability to achieve the PSI we are searching for, of all the examined current structures, this was the most naturally conducive to the generation of near-inertial waves and the examination of their effects (and possible PSI). Hence, a great many tests of this type were performed on this current structure, and we will focus upon it for the remainder of our discussion. For the time being, we will limit ourselves to one example here for a brief demonstration, as we did with the others. The case study following this will closely examine a run of this type in much greater detail, however.

For this test case, the following parameters are set:

$$\zeta(z) = 1 + \tanh(\frac{z + 400}{50}) \tag{4.9}$$

$$hvar(x) = 1600(0.5(1 + \tanh(\frac{x + 30000}{40000})) - 0.5(1 + \tanh(\frac{x - 30000}{40000})))^2 \tag{4.10}$$

This case was run for $60K_1$ tidal periods, using the piecewise bathymetry. This case had 200 gridpoints in the vertical; $I = 13000$, $I_l = I_r = 3000$; and an initial timestep of 14.95625 s. The maximum tidal current strength for this case was set to 0.02 m/s. We will adopt the abbreviation "DT", for "difference (of) tanh (functions)", in figures regarding this case.

For this test case, we have $f_{eff}^2|_{min} = 8.34665204 \times 10^{-10}$ s^{-2} and $f_{eff}^2|_{max} = 1.94981162 \times 10^{-9}$ s^{-2}. This gives $\frac{f_{eff}|_{min}}{\sigma} \approx 0.396$ and $\frac{f_{eff}|_{max}}{\sigma} \approx 0.605$.

An inertial instability criterion mapping, along with initial profiles for the square of the effective Coriolis frequency, density, and background current can be seen in Figure 4.10. We note that we have a stable case, and that the region wherein the effective Coriolis frequency's square dips below the

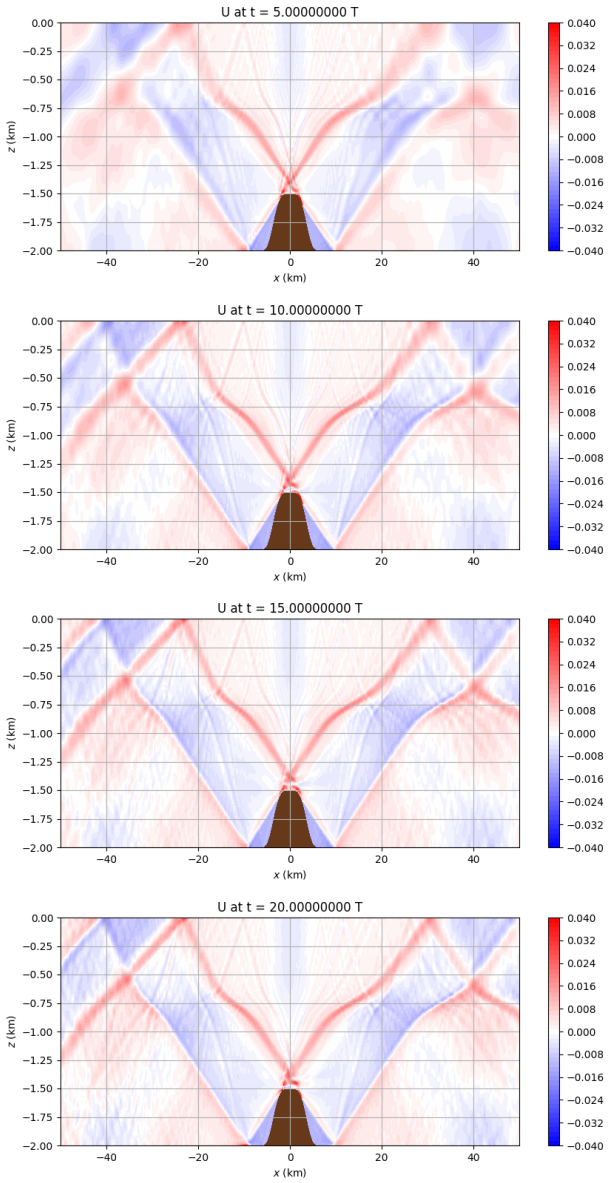

Figure 4.9: Plots of the x-component of the baroclinic current U for our S case. Note that U here is shown as a function of x and z (both in km), while the colourbar shows its value (in m/s). Respectively, these plots show U at 5, 10, 15, and 20 tidal periods.

critical value is a bowl-shaped region at the top of the ocean about 250 m in vertical width stretching out from the centre of the ridge to ± 20 km in either direction. As always, such a region corresponds with where we see the greatest change in density and change in slope of the initial background current at the surface/gradient of the background current.

This test case was one of a great many members of its family, and indeed, the case study we will examine later was actually derived from this case. We can observe the current profiles in Figure 4.11. One key point of note from this case is the effects visible at around $x = \pm 20$ km between $z = 0$ m and $z = -250$ m, particularly starting at around 40 tidal periods (though very faintly visible at 30; much more visible at 60). While initially faint, we notice regions of the internal wave beams that appear almost flat, in a stripe-like pattern. For example, comparing the profiles at 10 tidal periods versus at 60 in this region, whereas we have the relatively standard internal wave beam structure we have seen so far at 10 tidal periods, at 60 tidal periods, we have a pattern of beams with near-horizontal slopes. As we know that our case is inertially stable, it falls to reason then that inertial instability is not the primary cause of such patterns developing. It falls to reason, then, that another factor must be possible for this phenomenon. The patterns visible here take a long time to form, however, and are not particularly strong. To remedy this, if we were to make the initial tidal current strength greater and lengthen the runtime of this simulation, we could hasten the development of and magnify the effects visible here. With this as inspiration, this case had its parameters adjusted accordingly, and was probed in much greater depth to look for more conclusive results. Such probing warrants its own discussion, and so, having seen some simpler results from test cases as motivation, we turn now to the detailed exploration of this particularly interesting case.

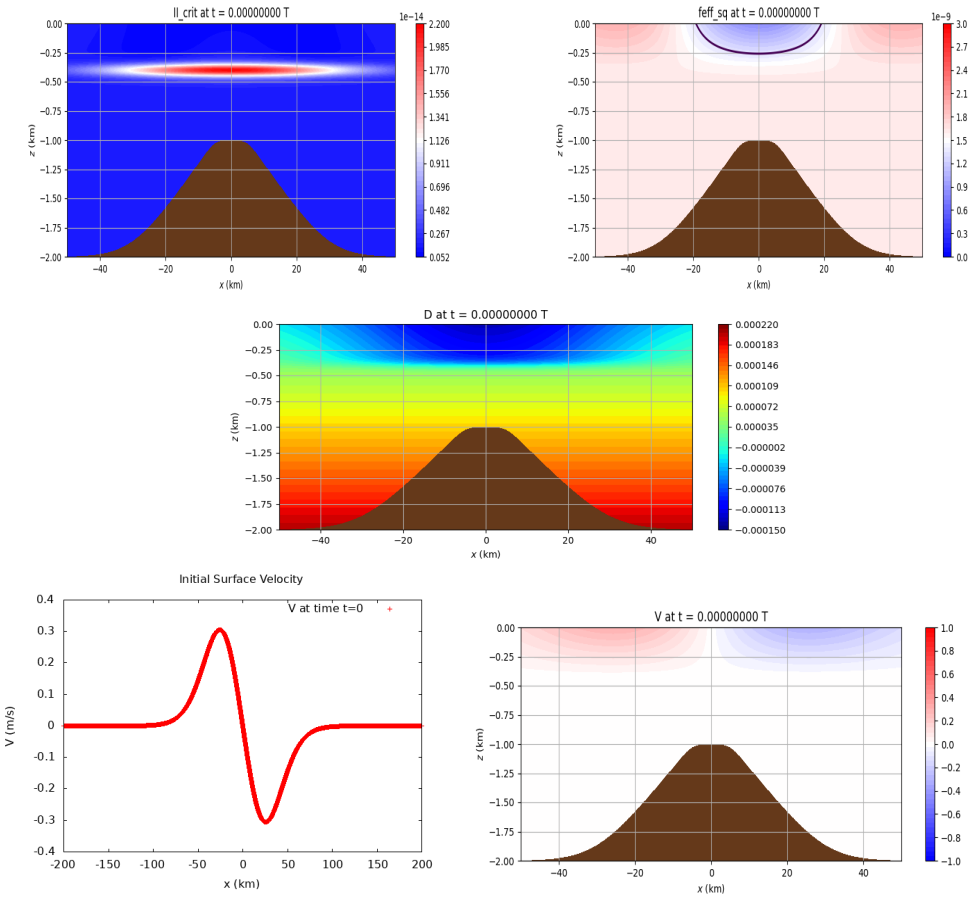

Figure 4.10: Top-left: A plot of the absolute value of the instability criterion for our DT case. The instability criterion, or II_{crit} on the plot, is shown as a function of x and z, with the colourbar showing its value (units of s^{-4}). Note the lack of a dark line - there are no zeroes, hence no instabilities. Top-right: A map of the value of the square of effective Coriolis frequency, f_{eff}^2. The colourbar shows its magnitude, in s^{-2}. The purple line denotes the critical value of f_{eff}^2. Middle: The initial density profile for this case. The colourbar shows the magnitude of the density D, which is dimensionless. Bottom-left: A plot of the initial background current at the surface for this case. The red line shows the velocity at the surface, V, in units of m/s. Bottom-right: A plot of the initial background current V for this case. Note that V here is shown as a function of x and z (both in km), while the colourbar shows its value (in m/s).shows the velocity, V, in units of m/s.

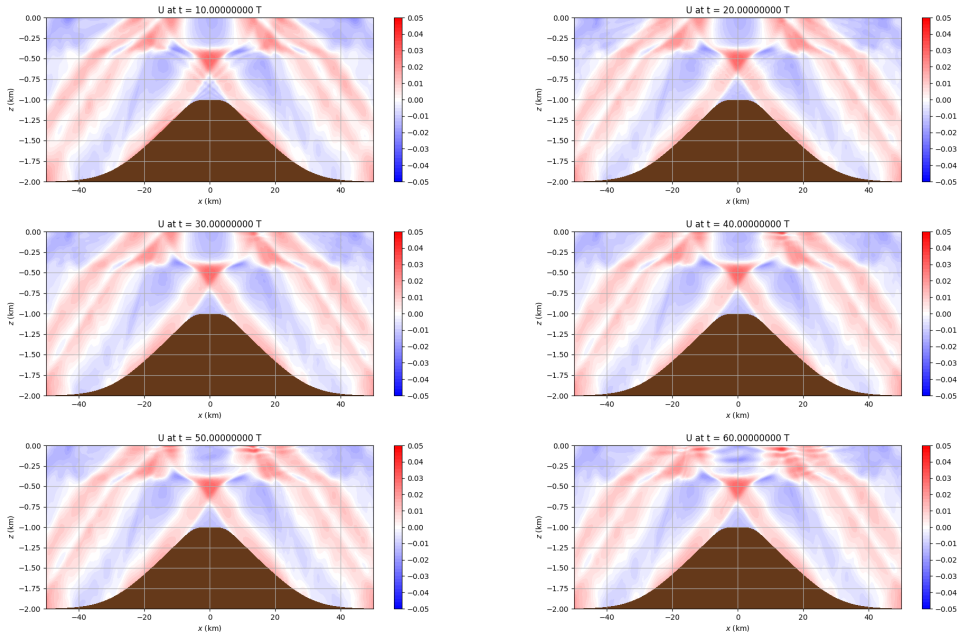

Figure 4.11: Plots of the x-component of the baroclinic current U for our DT case. Note that U here is shown as a function of x and z (both in km), while the colourbar shows its value (in m/s). Respectively, these plots show U at 10, 20, 30, 40, 50, and 60 tidal periods.

4.3 Case Study

4.3.1 Presentation of Core Results

To conclude the presentation of our results, we will take some time to look at a particular case of note. After careful experimentation with all three families of the horizontal current structures seen so far, it was deemed that the difference of hyperbolic tangents seemed most naturally conducive to generating the PSI we are searching for. Hence, a great deal of time was spent examining this particular family in detail.

While using the same general framework as the difference of tanh case we saw previously, this one has the following modifications:

- The maximum current strength was increased to $U = 0.03$ m/s (chosen after careful experimentation for its ability to yield prominently visible, yet stable results).

- The simulation was allowed to run for a full 80 tidal periods.
- The centering in z was moved to -750 m as opposed to -400 m, to enlarge the region capable of experiencing an effective Coriolis frequency below the critical value.
- The piecewise bathymetry was used again, and multiple different values of the length of its top were explored (7.5 km, 10 km, and 15 km, respectively). Of these, we will focus on the 10 km top, though results from the other two cases will be presented for contrast.

With all this in mind, we begin by looking at the preliminary results for this special case, as we have with all of the other cases so far. The parameters set for this case are as follows:

$$\zeta(z) = 1 + \tanh(\frac{z+750}{50}) \tag{4.11}$$

$$hvar(x) = 1600\{0.5[1 + \tanh(\frac{x+30000}{40000})] - 0.5[1 + \tanh(\frac{x-30000}{40000})]\}^2 \tag{4.12}$$

This case was run for $80K_1$ tidal periods, using the piecewise bathymetry. This case had 200 gridpoints in the vertical; $I = 14000$, $I_l = I_r = 4000$; and an initial timestep of 14.95625 s. For this test case, we have $f^2_{eff}|_{min} = 1.61 \times 10^{-10}$ s^{-2} and $f^2_{eff}|_{max} = 2.26 \times 10^{-9}$ s^{-2}. This gives $\frac{f_{eff}|_{min}}{\sigma} \approx 0.174$ and $\frac{f_{eff}|_{max}}{\sigma} \approx 0.652$. We will adopt the abbreviation "CS", for "case study", in figures regarding this case.

As we have done before, we commence by looking at the usual plots of instability criterion, square of the effective Coriolis frequency, initial density, and initial background current. These are presented in Figure 4.12. While these are quite similar to the case we looked at in Section 4.2.3, the most important changes are visible in the density and effective Coriolis frequency plots. The area wherein the effective Coriolis frequency dips below the critical value is significantly larger here, spreading out approximately the same distance horizontally (between ± 20 km), but now extending below a depth of 500 m in the vertical. This corresponds to the large dark-blue region on the density plot, wherein we see the lines of constant density undergoing rapid change in slope. What this tells us is that we have a large central region, extending deep from the surface and well over top of the ridge's sloping sides, in which we have the possibility of the development of PSI.

For a closer look at the results in this case, now, we break the usual current profiles (U) into two separate figures. Figure 4.13 shows the current profiles at each consecutive passing of 10 tidal periods up to 60 tidal periods. Figure 4.14 continues this set of velocity profiles, but now at an interval of 5 periods, up to the complete 80 tidal periods of the simulation.

Looking at the first couple of plots in Figure 4.13, things seem to proceed in a similar manner as the previous observed cases, with the development of internal wave beams. At around 20 tidal periods, however, things begin to change. We see an instability beginning to grow at around $\pm 20km$ near the surface, which takes the form of a faint pattern of lines. This instability grows stronger over time (extending downward as it does), and its growth is observable throughout the rest of the plots in Figures 4.13 and 4.14. By 80 tidal periods, the structure is well-defined and has grown quite strong.

We note that our case is not inertially unstable anywhere, so this instability must have another cause. The region of this instability's inception is within the region where the effective Coriolis frequency is below the critical value (with the exception of just over the ridge; more on this in Chapter 4.3.3), so it is possible for this observed instability to be caused by PSI. To further add credibility to our search, if we recall back to Section 2.2, given what we know about the slope of internal wave beams, observe the wave beams in the region of the growing instability. For example, comparing the internal wave beams in the plot for 10 tidal periods versus the ones in the plot for 30 tidal periods in Figure 4.13, we see that while at 10 tidal periods, we had our standard fairly straight internal wave beams, in the "blurring" regions, we have internal wave beams that are almost horizontal. Indeed, as we progress further into the simulation, we see more of these near-horizontal beams appearing, until, by 80 tidal periods, they are extremely visible and have spread across a wide swath of the area around the ridge. The development of near-horizontal wave beams (thus, significantly closer to zero in slope than beams of waves at tidal frequency; i.e. more likely to have waves of half the tidal frequency), particularly beginning from a region wherein the effective Coriolis frequency was lowered below its critical value, is promising for the analysis of PSI effects in this simulation. While this does not guarantee that PSI is indeed the driving factor behind the patterns we see here, it gives us further motivation to pursue the identity of this instability.

As a final remark before we explore this further, we consider a couple of curious phenomena observed in this case. To begin, we would expect that as the waves of tidal frequency travel upward and outward from the ridge, they would be continually moving into regions of lower f_{eff}. Should PSI occur in

these regions, we would expect the generation of waves with lower frequency than the parent waves, and thus would expect to see flatter slopes on said waves. Why, then, do we see regions of increasing slope in 4.13 and 4.14, particularly between the surface and $z = -750$ m beyond $x = \pm 20$ km? In tandem with this, one other issue of note is that we find the patterns observed initially in the region of lowered effective Coriolis frequency creeping down well below where they should be capable of developing. What, then, is going on in these regions? To answer the first question, the waves we see with positive slopes would be travelling through the region with the background current present. As these beams move into regions of greater f_{eff} and changing N, it is reasonable to assume that their slopes would change accordingly, as we have seen in the some of the cases observed in Chapter 4.2 (e.g. see the plot Figure 4.9 at 20 tidal periods). Thus, even if these waves started from a different frequency than that of the tidal frequency waves, this change in slope, even towards the positive, agrees with what we would expect. As for what generates these waves, or from whence they originate, the clearest way to answer our second question will be to more thoroughly analyze the patterns we are seeing in these peculiar regions, and we will turn to this in Section 4.3.3.

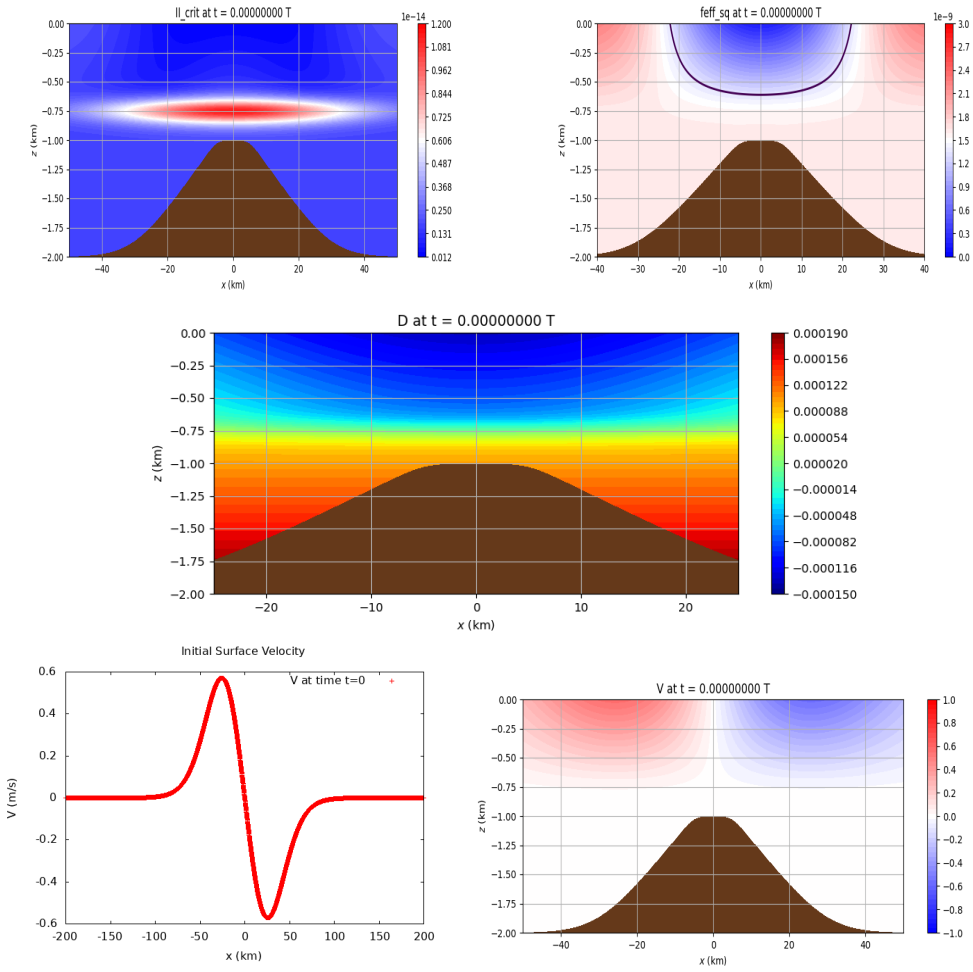

Figure 4.12: Top-left: A plot of the absolute value of the instability criterion for our case study (CS). The instability criterion, or II_{crit} on the plot, is shown as a function of x and z, with the colourbar showing its value (units of s^{-4}). Note the lack of a dark line - there are no zeroes, hence no instabilities. Top-right: A map of the value of the square of effective Coriolis frequency, f_{eff}^2. The colourbar shows its magnitude, in s^{-2}. The purple line denotes the critical value of f_{eff}^2. Middle: The initial density profile for this case. The colourbar shows the magnitude of the density D, which is dimensionless. Bottom-left: A plot of the initial background current at the surface for this case. The red line shows the velocity at the surface, V, in units of m/s. Bottom-right: A plot of the initial background current V for this case. Note that V here is shown as a function of x and z (both in km), while the colourbar shows its value (in m/s).shows the velocity, V, in units of m/s.

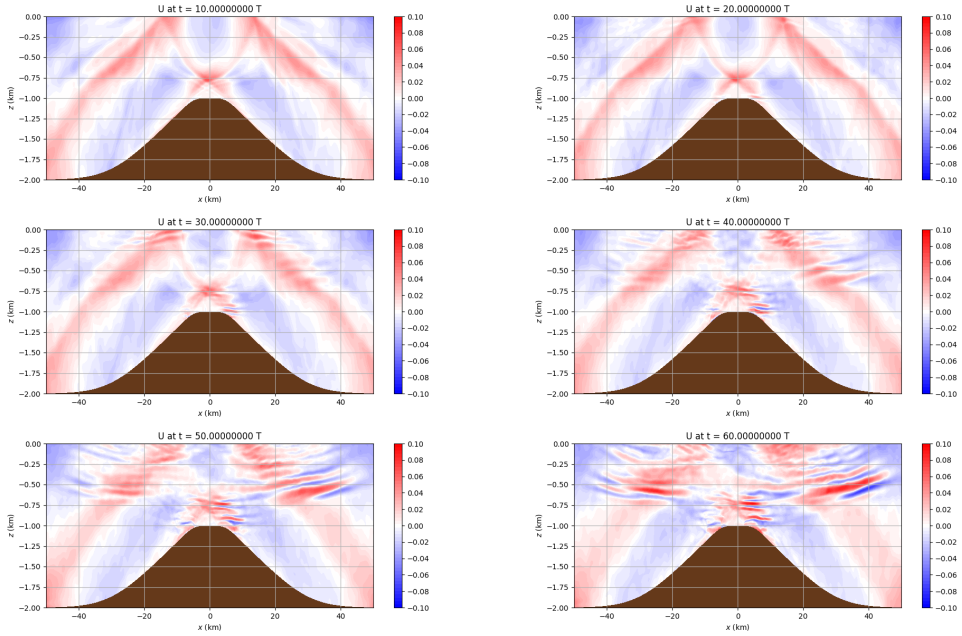

Figure 4.13: Plots of the x-component of the baroclinic current U for our case study (CS). Note that U here is shown as a function of x and z (both in km), while the colourbar shows its value (in m/s). Respectively, these plots show U at 10, 20, 30, 40, 50, and 60 tidal periods.

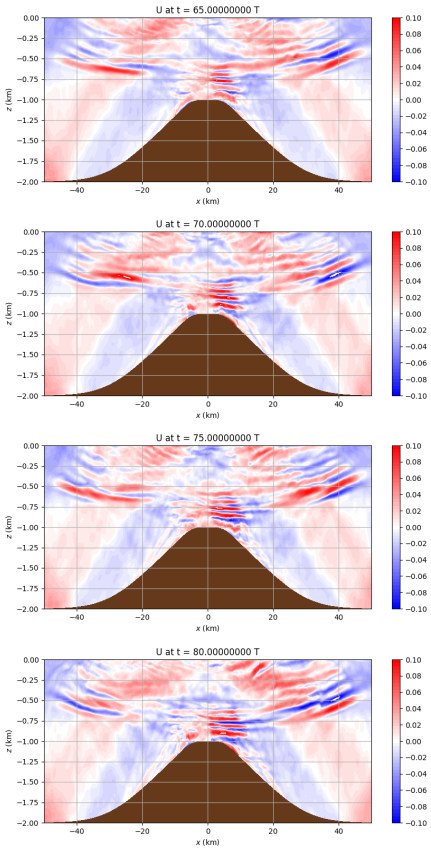

Figure 4.14: Plots of the x-component of the baroclinic current U for our case study (CS). Note that U here is shown as a function of x and z (both in km), while the colourbar shows its value (in m/s). Respectively, these plots show U at 65, 70, 75, and 80 tidal periods.

4.3.2 Comparative Simulations

Before we commence with analysis of our waveforms, for a few points of comparison, we present slight variations on the base results of our case study. The first sets of plots we look at are in Figures 4.15 and 4.16, wherein we see our results contrasted with simulations run with differing lengths of the tabletop in our bathymetry (7.5km and 15km, respectively for each Figure). Note that in this comparison, we omit the auxiliary plots (e.g. effective Coriolis frequency, background current, etc.) as changing the top length of the ridge has no effect on the initial current. In figures referencing these cases, we will adopt the abbreviations "CS7.5kmT" and "CS15kmT", for "case study 7.5 km top" and

"case study 15 km top", respectively. The second point of comparison we will observe uses the original 10km tabletop, but slightly modifies the base parameters of the horizontal current in our simulation. Specifically, we take the horizontal amplitude factor ($hvar_{max}$) and the distance over which the horizontal density perturbation occur (λ_x) and raise/lower them by 5% each. In figures referencing these cases, we will adopt the abbreviations "CSP5%" and "CSM5%", for "case study plus 5 percent" and "case study minus 5 percent", respectively.

Figures 4.15 and 4.16 show the current profiles for a simulation identical to the base case for our case study, but with the top lengths of the bathymetry changed to 7.5 km and 15 km, respectively. Figures 4.18 and 4.17 display, analogously to Figure 4.13/4.14 and 4.12, the current profiles and instability criterion, effective Coriolis frequency (squared) mapping, initial density, and initial background current for the case where we keep the same top length as our base, but increase horizontal amplitude scaling and horizontal perturbation spread by 5% Figures 4.20 and 4.19 show this for the case where these values are decreased by 5% instead.

For the most part, the plots we see in these figures are quite similar to their respective counterparts in the case study. Hence, we will focus here on what has changed in these variations:

- A change in the length of our tabletop changes both the relative strength of our generated instability, and how early (in terms of tidal periods) it is produced. A smaller top length causes an increase in relative magnitude and a decrease in time required to develop, while the opposite is true for a longer top length. This is particularly easy to see by comparing plots of the same tidal period across all three cases. For example, in Figure 4.13 at 30 tidal periods, the instability at $x = \pm 20$ km is just barely forming, while it is clearly formed in 4.15 and is only faintly visible (if at all) on one side in 4.16. Both of these results stem from the fact that changing the length of the tabletop alters the horizontal location at which the internal wave beams are generated. This directly impacts where the beams reach the surface in relation to the region of lowered effective Coriolis frequency, as well as the points at which reflected and incident wave beams intersect. For example, widening the tabletop pushes these points outwards relative to the region of lowered f_{eff}, while narrowing it does the opposite. Such is consistent with why we see effects developing more quickly and in greater magnitude in the smaller tabletop's horizontal baroclinic current profiles compared to the

larger one - the narrower tabletop better focuses the developed internal wave beams into the region of lowered f_{eff}, allowing for its effects to begin developing sooner and continue developing for lnger.

- In the simulation where we increased/decreased horizontal amplitude scaling and horizontal perturbation spread parameters by 5%, we see a slight decrease/increase in the magnitude of our generated instability. For a simple comparison, look at the size of dark red/blue in the plots at 60 tidal periods in Figures 4.14, 4.18, and 4.20. Thinking back to our instability criterion and its dependent parameters, this result is consistent with what we have discussed previously. Slightly further concentrating/spreading out the area over which the initial horizontal current perturbation occurs by changing the heights pycnoclines are changed (amplitude) and horizontal spread parameter should cause greater/lesser resulting effects. For example, when we decrease the horizontal amplitude scaling on our background current, we see a more gradual change over the pycnocline, resulting in smaller gradients of fluid velocity. Consequently, as f_{eff} is dependent on the velocity gradient, it follows, that we get a lowered minimum value for f_{eff} in a case with this kind of reduction. The opposite would hold true for amplification. Obviously, these simulations are very close to our original, and their departures from it are small, but it is important to see this occur and verify it nonetheless. Note that too large a deviation could betray our instability criterion or drastically reduce our visible instability effects, neither of which would be desirable.

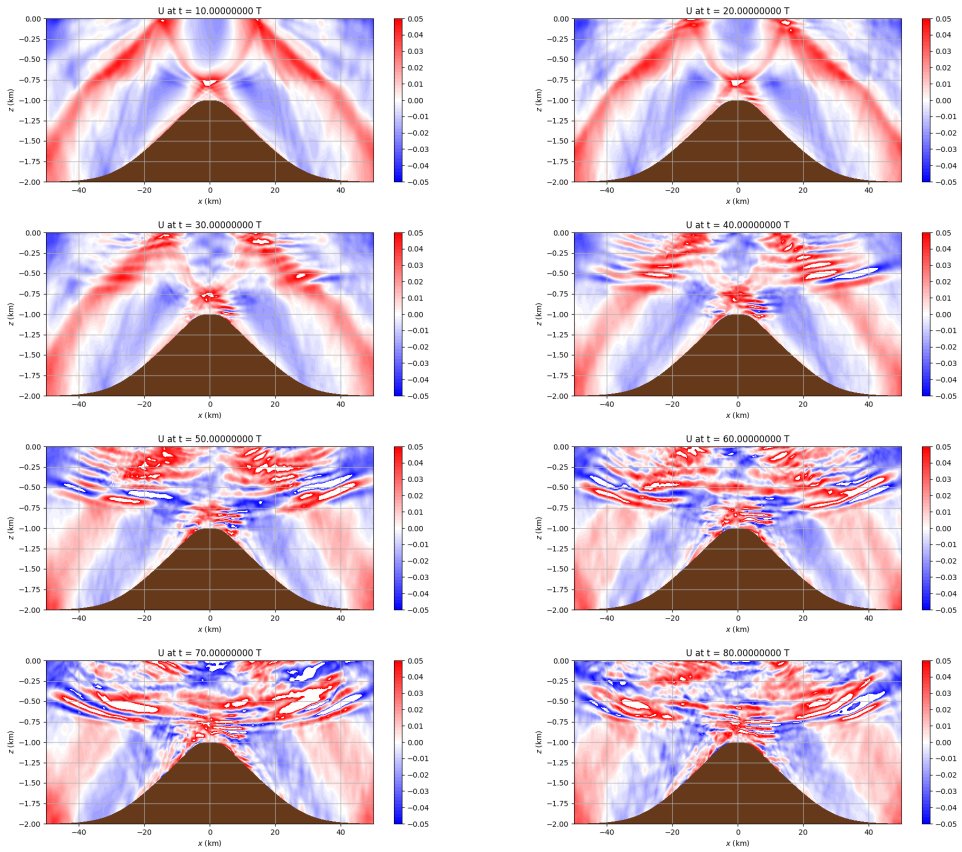

Figure 4.15: Plots of the x-component of the baroclinic current U for our modified case study with the 7.5 km top length bathymetry (CS7.5kmT). Note that U here is shown as a function of x and z (both in km), while the colourbar shows its value (in m/s). Respectively, these plots show U at 10, 20, 30, 40, 50, 60, 70, and 80 tidal periods. Large white gaps are regions where the magnitude of the current exceeds the limits of the colourbar.

4.3.3 Analysis

To answer the question of whether PSI is indeed active in our chosen case of study, we perform further analysis of the spectra of the waves observed in the regions of largest instability.

To do so, we begin by isolating the horizontal baroclinic velocity U as a function of z and t at a fixed horizontal location. In our case study, given that we see large instabilities growing at $x = \pm 20$ km, we perform our analysis at $x = 20$ km (one could equivalently perform the analysis on the other side for similar results). Figure 4.21 shows this value plotted every four tidal periods, starting from when we see the instability first seriously begin its growth, around 20 tidal periods, until about 60 tidal periods, when the instability is large and visible.

Looking at the plots in Figure 4.21 of U at this horizontal location, it is apparent that an instability is indeed growing. Over time, though the internal waves send energy upward, an instability begins creeping down the water column from near the surface. That it appears to be generated between $z = 0$ m and $z = -200$ m coincides with the region of lowered effective Coriolis frequency, as we can see in the third plot in Figure 4.12. We next seek to confirm the frequency/frequencies present along this vertical slice, and in particular want to do so at specific points in the horizontal. By taking spectra at specific points (x, z) like this, we can confirm exactly which frequencies are passing through that point over time.

To begin, as a control, we want to examine the power spectrum at a point (x, z) of a stable simulation wherein PSI (or the possibility thereof) was seemingly not observed. To create this control, we take the simulation presented in our case study, but run it with one-third of the maximum tidal current strength (0.01 m/s as opposed to 0.03 m/s). Recall from Section 2.2.1 that the components of velocity for our internal waves are on the same order as the amplitude of said waves, By decreasing the maximum tidal current amplitude, not only do we deal with smaller velocity gradients, but also, if we consider that PSI waves must grow from daughter waves of the original tides, we produce perturbation waves of smaller amplitudes, which will take a longer time to grow. This helps reduce the chance of seeing it form (or at least delay it sufficiently), while still maintaining the stability of the underlying background current. For the figure for this special example case, we will use the abbreviation "CSNoPSI", for "case study, no PSI".

The resulting power spectrum density plot is presented in Figure 4.22, along with a plot of the current profile at the tidal period at the end of the

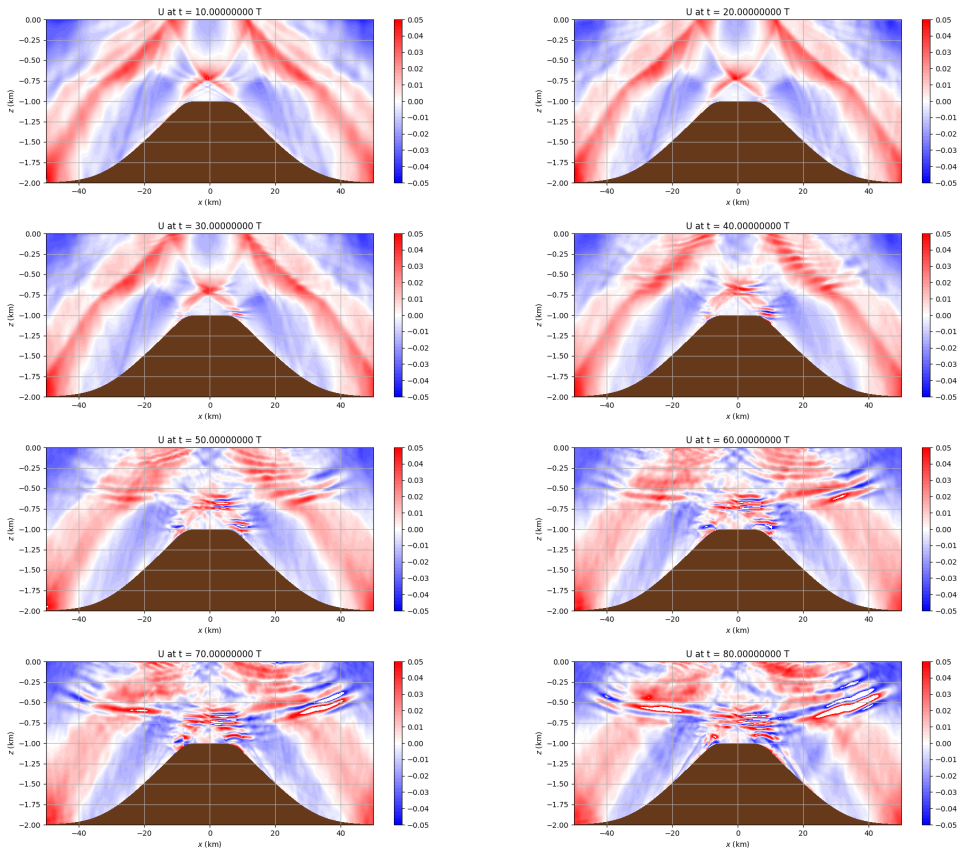

Figure 4.16: Plots of the x-component of the baroclinic current U for our modified case study with the 15 km top length bathymetry (CS15kmT). Note that U here is shown as a function of x and z (both in km), while the colourbar shows its value (in m/s). Respectively, these plots show U at 10, 20, 30, 40, 50, 60, 70, and 80 tidal periods. Large white gaps are regions where the magnitude of the current exceeds the limits of the colourbar.

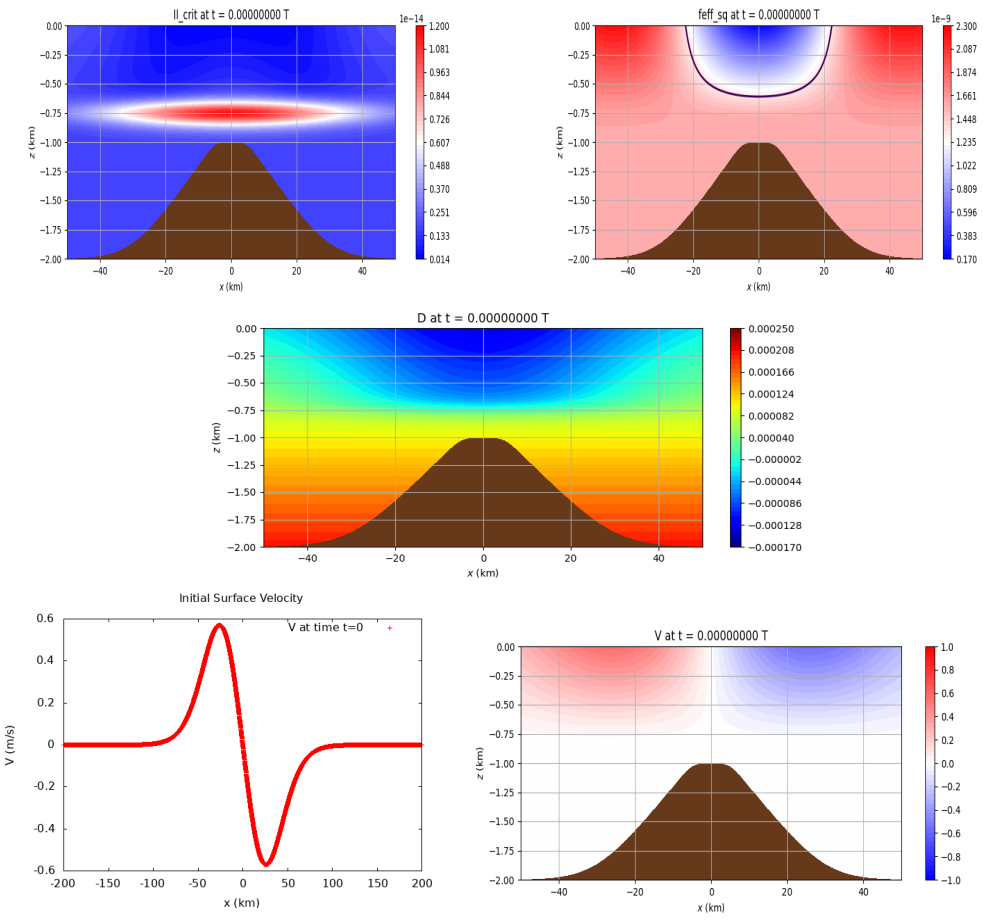

Figure 4.17: Top-left: A plot of the absolute value of the instability criterion for our modified case study with the horizontal amplitude factor and horizontal density perturbation length increased by 5% (CSP5%). The instability criterion, or II_{crit} on the plot, is shown as a function of x and z, with the colourbar showing its value (units of s^{-4}). Note the lack of a dark line - there are no zeroes, hence no instabilities. Top-right: A map of the value of the square of effective Coriolis frequency, f_{eff}^2. The colourbar shows its magnitude, in s^{-2}. The purple line denotes the critical value of f_{eff}^2. Middle: The initial density profile for this case. The colourbar shows the magnitude of the density D, which is dimensionless. Bottom-left: A plot of the initial background current at the surface for this case. The red line shows the velocity at the surface, V, in units of m/s. Bottom-right: A plot of the initial background current V for this case. Note that V here is shown as a function of x and z (both in km), while the colourbar shows its value (in m/s).shows the velocity, V, in units of m/s.

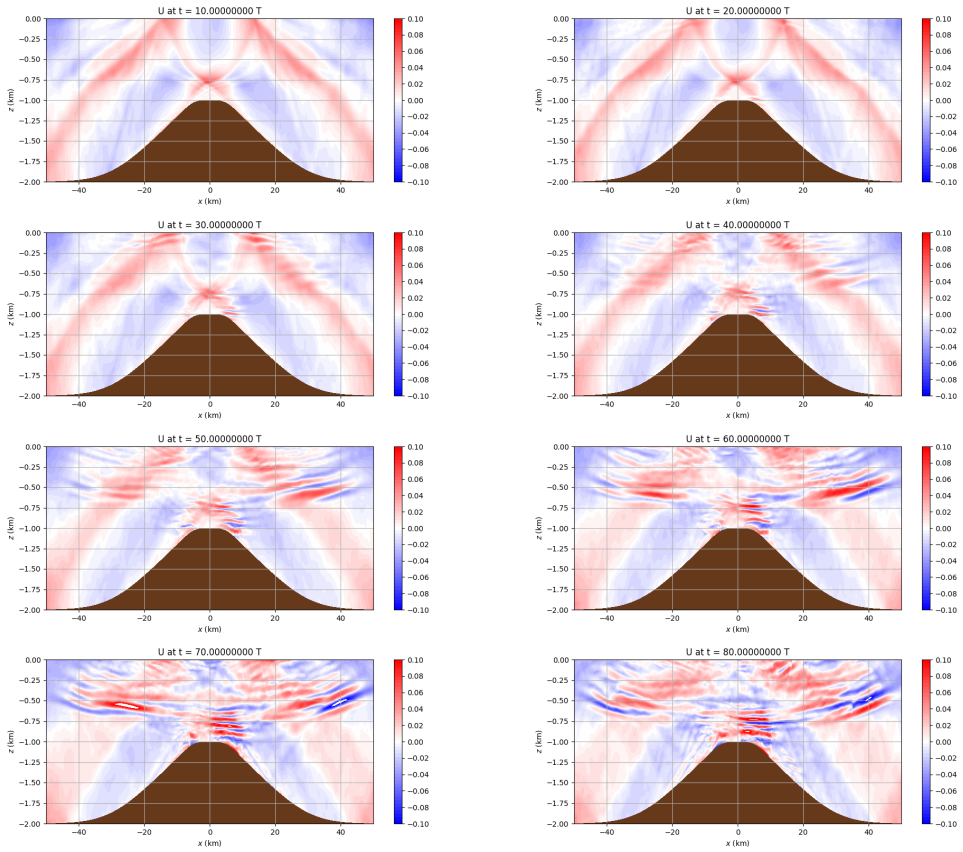

Figure 4.18: Plots of the x-component of the baroclinic current U for our modified case study with the horizontal amplitude factor and horizontal density perturbation length increased by 5% (CSP5%). Note that U here is shown as a function of x and z (both in km), while the colourbar shows its value (in m/s). Respectively, these plots show U at 10, 20, 30, 40, 50, 60, 70, and 80 tidal periods. White gaps in the middle of coloured zones are regions where the magnitude of the current exceeds the limits of the colourbar.

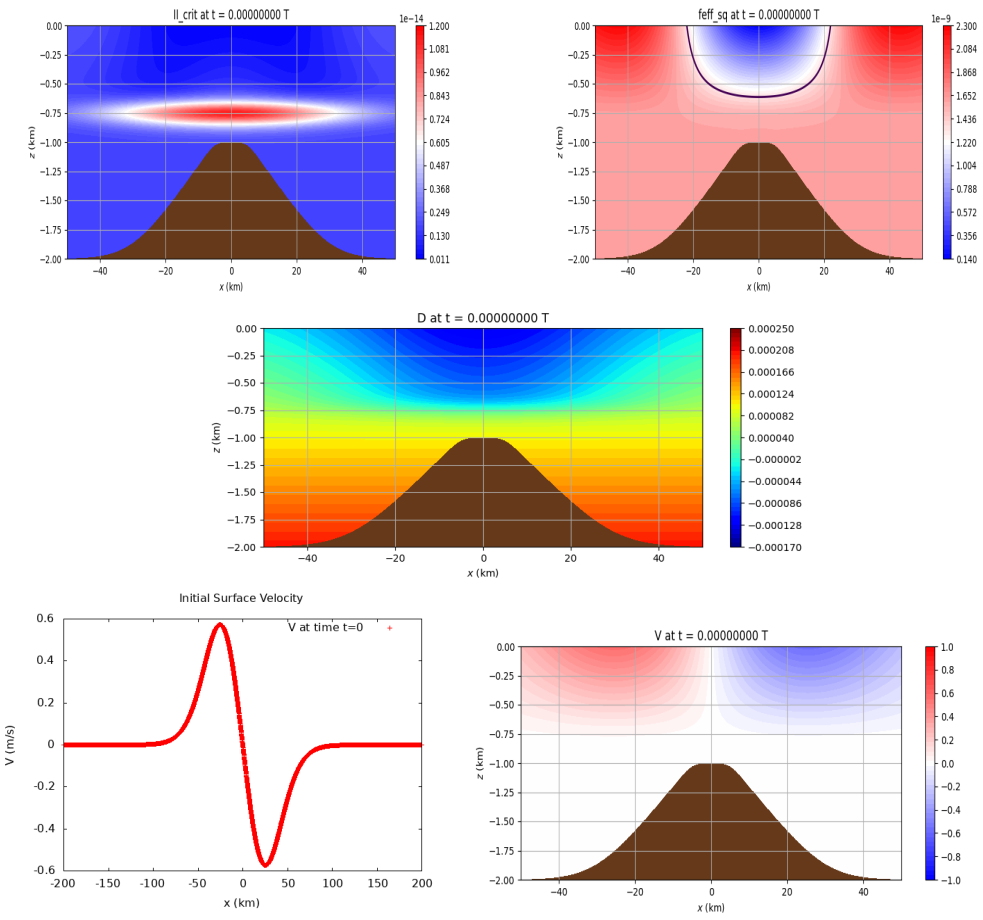

Figure 4.19: Top-left: A plot of the absolute value of the instability criterion for our modified case study with the horizontal amplitude factor and horizontal density perturbation length decreased by 5% (CSM5%). The instability criterion, or II_{crit} on the plot, is shown as a function of x and z, with the colourbar showing its value (units of s^{-4}). Note the lack of a dark line - there are no zeroes, hence no instabilities. Top-right: A map of the value of the square of effective Coriolis frequency, f_{eff}^2. The colourbar shows its magnitude, in s^{-2}. The purple line denotes the critical value of f_{eff}^2. Middle: The initial density profile for this case. The colourbar shows the magnitude of the density D, which is dimensionless. Bottom-left: A plot of the initial background current at the surface for this case. The red line shows the velocity at the surface, V, in units of m/s. Bottom-right: A plot of the initial background current V for this case. Note that V here is shown as a function of x and z (both in km), while the colourbar shows its value (in m/s).shows the velocity, V, in units of m/s.

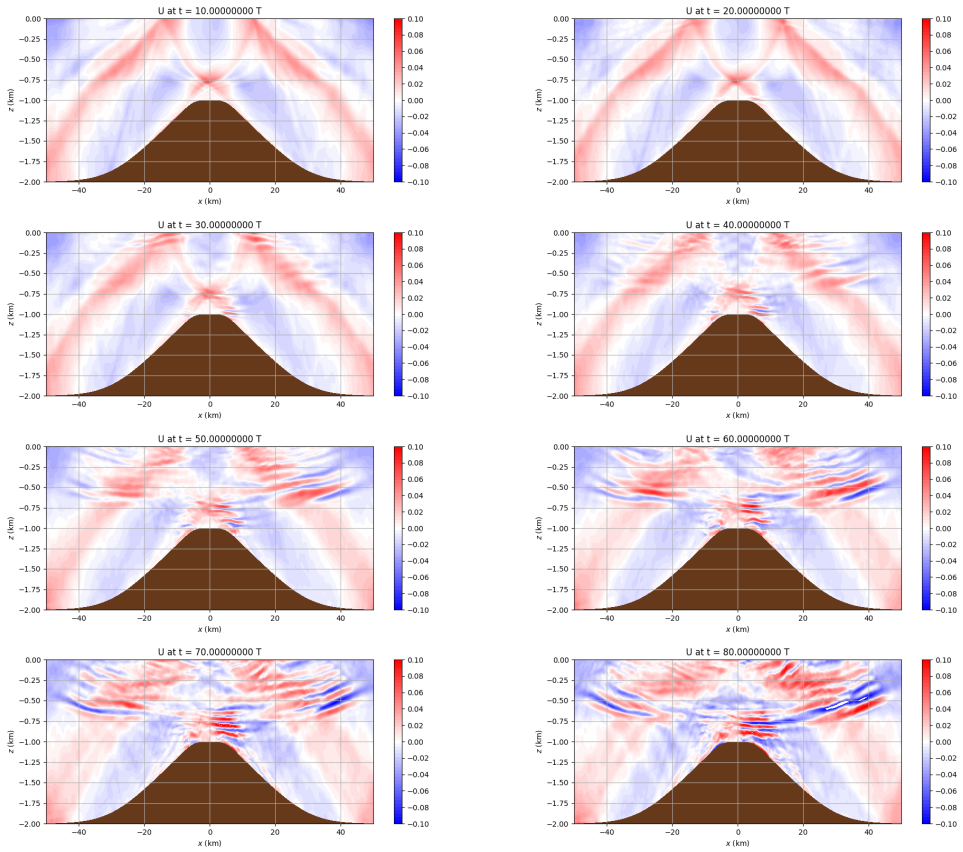

Figure 4.20: Plots of the x-component of the baroclinic current U for our modified case study with the horizontal amplitude factor and horizontal density perturbation length decreased by 5% (CSM5%). Note that U here is shown as a function of x and z (both in km), while the colourbar shows its value (in m/s). Respectively, these plots show U at 10, 20, 30, 40, 50, 60, 70, and 80 tidal periods. White gaps in the middle of coloured zones are regions where the magnitude of the current exceeds the limits of the colourbar.

spectral measurement (60 K_1). Note that power spectral density plots were created using periodogram in Python's scipy module with no windowing and a scaling by 2π to scale the spectra after transforms. Looking at the current profile in Figure 4.22, especially in comparison with the 60 tidal period plot in Figure 4.13, we see none of the effects that we could possibly attribute to PSI in this case. There does not seem to be any shaping of the internal wave beams by instability, particularly in the region wherein the effective Coriolis frequency would be lowered (refer to 4.12; the regions wherein f_{eff} dips below the critical value are the same here). Looking at the power spectral density plot, we see contributions at around one-third and two-thirds of the K_1 tidal frequency, and what appear to be contributions at the $(\frac{1}{2}+n)\omega_{K_1}$ harmonics $(1.5\omega_{K_1}, 2.5\omega_{K_1}, ...)$, but these contributions are over 5 orders of magnitude less than the primary contribution at the tidal frequency at their highest. Even compared to the peaks at $2\omega_{K_1}$ and $3\omega_{K_1}$ (which are present since internal wave beams are generated at all harmonics by linear theory), these peaks are still multiple orders of magnitude smaller. Such a result tells us that though it would not be impossible for PSI to be present in this case, given that we are already 60 tidal periods into the simulation, its contribution would be overwhelmingly minuscule compared to the tidal frequency and its harmonics. So, effectively, we can assume that we have a case without PSI here.

With the control out of the way and ready for comparison, we can now look at power spectral density plots for our case study proper. To this end, we present plots in two different capacities. The first plot we look at is Figure 4.23, wherein we have presented the power spectral density for the entirety of the run time of our case study (80 K_1 tidal periods). To more thoroughly study the development of patterns within the spectra, in 4.24, we present the power spectral density of our case study broken down into 20 K_1 tidal period-long pieces.

As was the case with our "No PSI" case, we have strong contributions at the tidal frequency and its harmonics, which is to be expected of internal waves generated by internal tides flowing over a ridge. However, this time, we see a marked contribution at $0.5K_1$, as well as the $(\frac{1}{2}+n)\omega_{K_1}$ frequencies. Indeed, the contribution at $0.5K_1$ is within two orders of magnitude of the contribution at the tidal frequency, the contribution at $1.5K_1$ is within three orders of magnitude of the primary contribution at the tidal frequency, and higher $(\frac{1}{2}+n)\omega_{K_1}$ frequencies provide larger contributions than the higher-order harmonics of the tidal frequency. We also see a significantly larger contribution at the zero frequency, around three-to-four orders of magnitude higher than in Figure 4.22 (though this is likely just a result of having a non-periodic time-series with

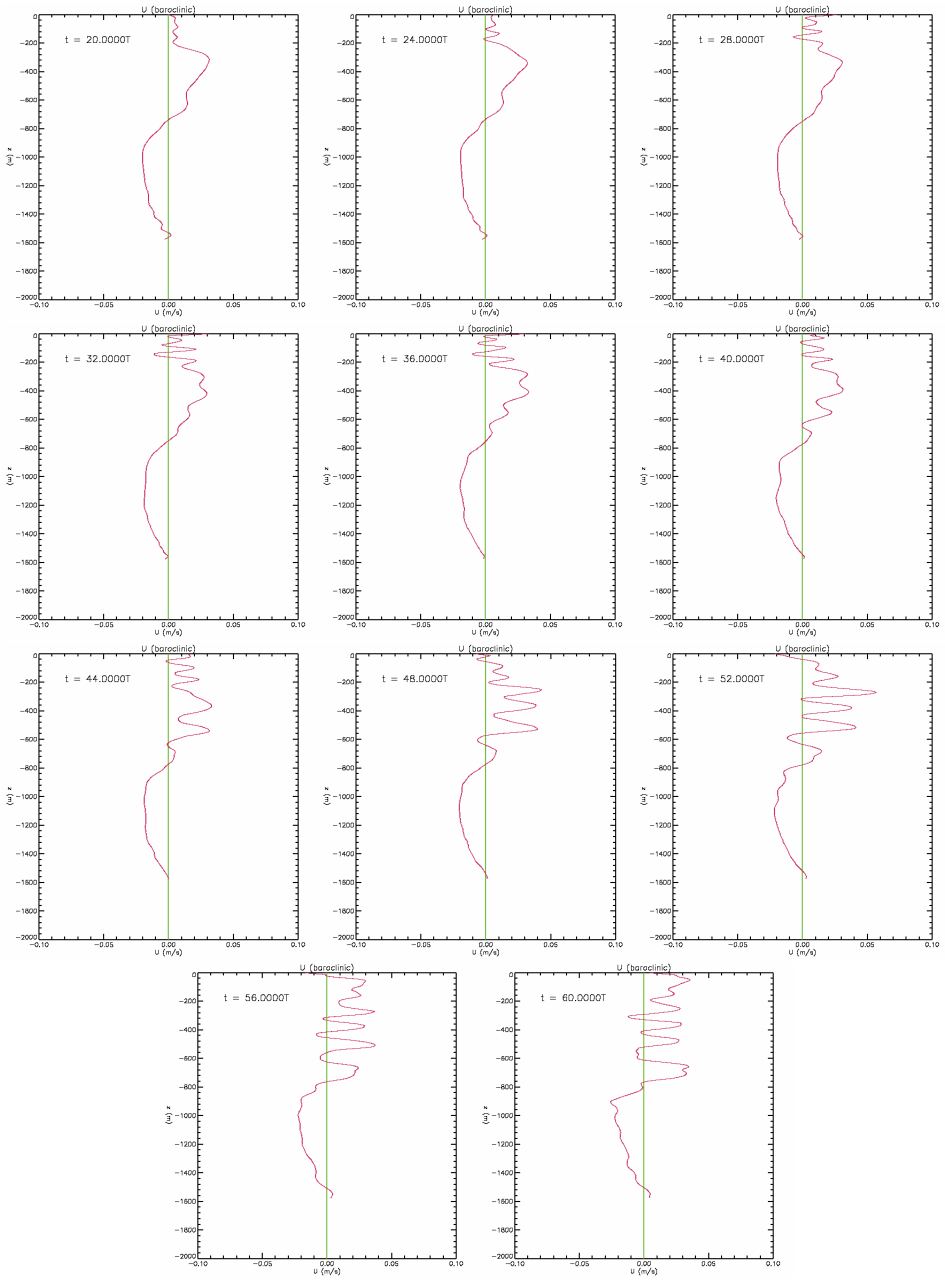

Figure 4.21: Plots of the x-component of the baroclinic current U for our case study (CS) as a function of z at the value $x = 20$ km. The green line marks off a baseline of $U = 0$, while the red line shows the magnitude of U, in m/s.

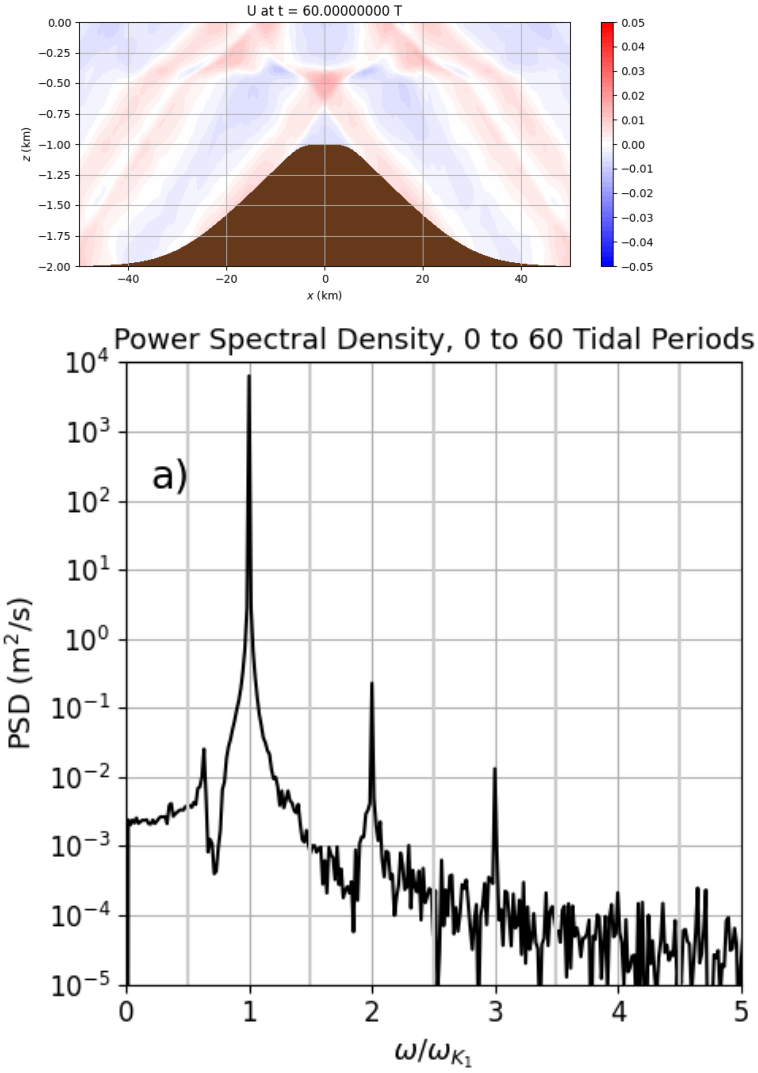

Figure 4.22: Top: A plot of the x-component of the baroclinic current U for our modified case study created to have no visible effects of PSI (CSNoPSI). This case was run over the Gaussian bathymetry with a maximum current strength of 0.01 m/s, but is otherwise the same as the case study. Note that U here is shown as a function of x and z (both in km), while the colourbar shows its value (in m/s). This plot was taken after 60 tidal periods had elapsed. Bottom: A power spectral density plot for our "no PSI" case. The power spectral density is shown as the magnitude of the spectrum (in m^2/s) at each frequency by ratio with the K_1 tidal frequency. This plot was taken from extracting U as a time series at $(x, z) = (20 \text{ km}, -450 \text{ m})$ from 0 to 60 tidal periods.

a non-zero mean, and this being more visible with our more complex case). More importantly, that we see contributions at the $(\frac{1}{2} + n)\omega_{K_1}$ frequencies likely indicates the changing effective Coriolis frequency and the induction of PSI that we have been searching for. Indeed, as we discussed in Section 2, PSI resonates most strongly at or around half of the tidal frequency and at integer multiples thereof, so to see contributions of a relatively similar order of magnitude (or sufficiently close) as the tidal frequency contributions strongly implies that we are seeing a prominent contribution from the effects of PSI in our waveforms. This time series was taken at the point $x = 20$ km, $z = -400$ m, which is in our region of lowered effective Coriolis frequency. Moreover, if we look at the plot for 10 tidal periods in Figure 4.13, originally, we would have had internal wave beams of tidal frequency passing through this point, which would have only given rise to contributions from the tidal frequency and its harmonics in the power spectral density plot. Hence, given that we have achieved the $(\frac{1}{2} + n)\omega_{K_1}$ frequencies here, it seems likely that the effects of PSI as induced by a lowered effective Coriolis frequency are indeed being observed in this case.

What remains to consider is the progression of the development of these PSI effects and to consider the noise present in Figure 4.23. To that end, we turn our attention to Figure 4.24. Looking at the first two plots, or the power spectral density plots for 0-20 and 10-30 tidal periods, respectively, we see a waveform initially dominated by frequencies in integer multiples of the tidal frequency. By 30 tidal periods, there may be small contributions at the half-integer frequencies visible, but these are at least 5 orders of magnitude lower than the central peak. Considering the 30 tidal period plot on Figure 4.13, wherein we saw the faint vestiges of a pattern emerging, this seems to correlate with what we would expect. Moving onward, looking at the plots for 20-40, 30-50, 40-60, and 50-70 tidal periods, we see the steady growth of contributions at the $(\frac{1}{2} + n)\omega_{K_1}$ frequencies, until the point where the power spectral density of the frequency $0.5K_1$ is within an order of magnitude of the tidal frequency by 70 tidal periods elapsed. One interesting point of note is the growth of the contributions at the higher harmonics. For example, in the 20-40 plot, the contributions at the frequencies $2.5K_1$ and $3.5K_1$ measure at around 10^{-1} m^2/s and 10^{-2} m^2/s, respectively, while by 70 tidal periods, these have increased by an order of magnitude. What we seem to therefore be observing is the steady growth of disturbance waves at both the $0.5\omega_{K_1}$ frequency and the $(\frac{1}{2} + n)\omega_{K_1}$ frequencies, which is what we would expect, given our previous discussion of PSI. What remains to discuss is the seeming shrinking of some of these large contributions in the 60-80 plot. This could be for a variety of

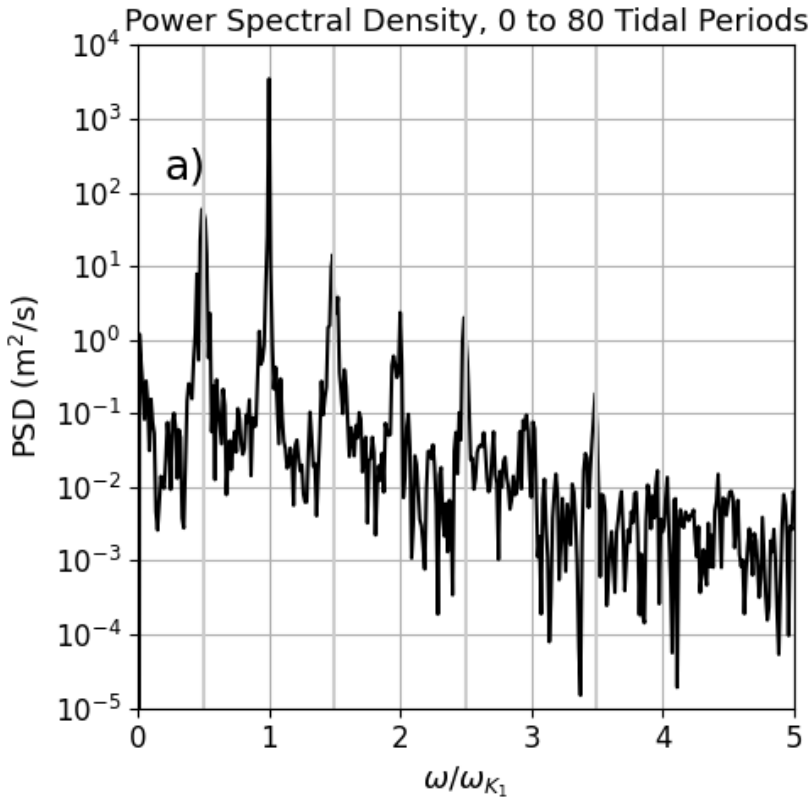

Figure 4.23: A power spectral density plot for our case study (CS). The power spectral density is shown as the magnitude of the spectrum at each frequency by ratio with the K_1 tidal frequency. This plot was taken from extracting U as a time series at $(x, z) = (20 \text{ km}, -450 \text{ m})$ from 0 to 80 tidal periods.

reasons - waves of these frequencies could be in the process of travelling away from the ridge, reducing contributions at the point at which we took the time series, energy could be dissipating with the breaking of waves over time, or indeed, other factors could be at play. Regardless, this does not change what we have seen - the subharmonic peaks are indeed visible throughout these pieces, and we see the clear development of a subharmonic resonance at the $(\frac{1}{2} + n)\omega_{K_1}$ frequencies.

As one final point of discussion, in Section 4.3.1, we considered the strange phenomenon of the effects we attribute to PSI creeping beyond the region in which the effective Coriolis frequency is lowered. Using our spectral analysis as before, we are equipped to more deeply consider the nature of these odd patterns. We will consider two examples for observation. Firstly, let us consider the elongated beam that develops between approximately $x = 25$ km to $x = 45$ km and $z = -750$ m to $z = -300$ m in the plots for 50 tidal periods and onward in our case study (see Figures 4.13 and 4.14). We present a series of spectra across various (x, z)-points along this beam in Figures 4.25 and 4.26, with points starting at $(x, z) = (25 \text{ km}, -650 \text{ m})$ and increasing by 5km intervals in the horizontal while decreasing by 50m intervals in the vertical between each row of plots. We see that the 0 to 40 tidal period plots differ to some extent across all of the various points, which is what would be expected, as these points would be in different regions of where the initial internal wave beams would be travelling. More interestingly, however, we see that for all of the 40 to 80 tidal period plots (and by extension, the 0 to 80 tidal period plot), we have predominant effects visible at half the tidal frequency and its harmonics. In particular, in the 40 to 80 tidal period plot at (40 km,−500 m) in Figure 4.26, the contribution at around (or just slightly above) half the tidal frequency is just over an order of magnitude lower than the contribution at the tidal frequency. This would suggest PSI's occurrence in this beam-like structure we have been studying, yet we are outside the range wherein the inertial frequency would have been lowered enough for this to happen.

To further examine this curious case, we zoom in on a single plot at (30 km, −600 m) between $0\omega_{K_1}$ and ω_{K_1} and provide lines to mark off every tenth of the tidal frequency. This is visible in Figure 4.27. Note that at this point, the square of the effecive Coriolis frequency is 1.657×10^{-9} s^{-2}, or equivalently, $\frac{f_{eff}}{\sigma} \approx 0.558$. In this Figure, we see a split peak approximately equally spaced on either side of $0.5\omega_{K_1}$. As previously mentioned in Sections 1.3 and 2.3, PSI is not limited to occurring strictly at exactly half of the tidal frequency; it can occur at or near it, so long as the two waves produced add up to the initial frequency in the end. This seems to be what is observed in 4.27 - we have two frequencies near half the tidal frequency that approximately add together to total the tidal frequency in value.

Let us consider the situation occurring around the peak of the ridge as well. Figure 4.28 shows power spectral density plots at the point (5 km, −900 m), just above and to the right of the ridge. As before, we seem to see spikes at the $(\frac{1}{2}+n)\omega_{K_1}$ frequencies, in this case even exceeding the contributions at the tidal frequency and its harmonics at each respective half interval ($0.5\omega_{K_1}$, $1.5\omega_{K_1}$,

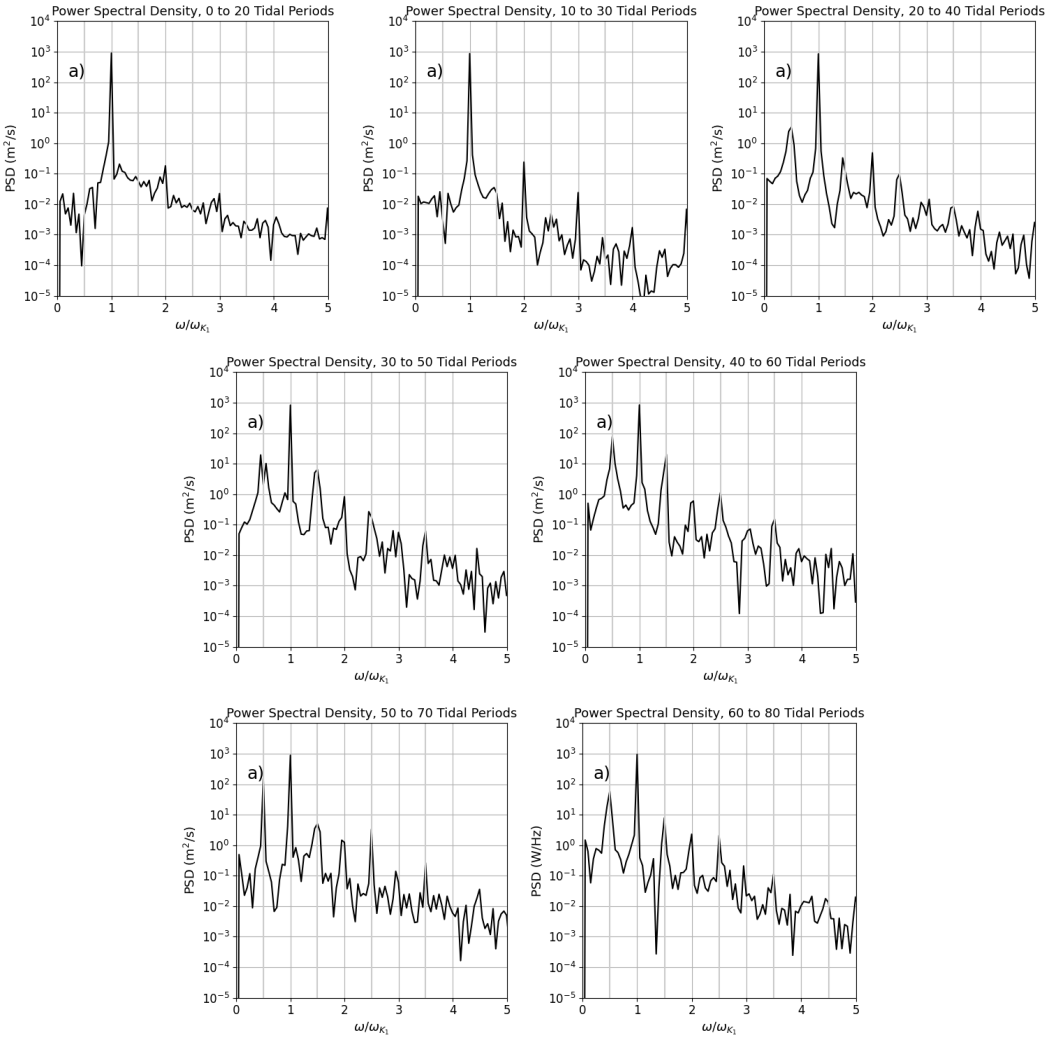

Figure 4.24: Plots of power spectral density for our case study (CS), broken down into 20 tidal period long intervals. The power spectral density is shown as the magnitude of the spectrum at each frequency (in m^2/s) by ratio with the K_1 tidal frequency. These plot were created by extracting U as a time series at $(x, z) = (20\ \mathrm{km}, -450\ \mathrm{m})$ from 0 to 20, 10 to 30, 20 to 40, 30 to 50, 40 to 60, 50 to 70, and 60 to 80 tidal periods, respectively.

...). However, before this is attributed to PSI, we should look more closely at what is happening over the ridge. To this end, density plots are presented in Figure 4.29, starting at 10 tidal periods and extending to 80 tidal periods. Over top of the ridge, we see the initially relatively flat density contours begin twisting and breaking, until they have been consumed by turbulent motions by 80 tidal periods. At our point in question in the spectra plots, we would be seeing significant breaking occurring over time, which means that the weakly nonlinear theory of PSI does not apply here. While it is not impossible for PSI to be occurring here (more on that in the next paragraph), the theory we have established thus far could not be properly used to analyze it, nor does it rule out other factors that could be causing the generation of waves of these non-integer frequencies instead.

Taken together, these plots suggest we have PSI occurring in regions where we are beyond the critical value for its development. Why then might this be occurring? One option is that these are not freely propagating waves. In such a case, we are seeing trapped waves generated by PSI in the region of lowered f_{eff} moving outwards. Such a theory would be corroborated by the relative consistency of the 40 to 80 tidal period plots and the 0 to 80 tidal period plots as we move along the examined beam. The waves would simply grow in amplitude and slowly spread outward over time as move waves generated in the region of lowered f_{eff} were sent to join them. Another alternative possible here is that our estimated critical value for the effective Coriolis frequency does not accurately reflect its actual value in the simulations. In this thesis, we have used the approximation by Kunze in his 1985 paper to define the effective Coriolis frequency. It is this definition that we have applied to our calculations thus far. However, such an approximation is not the complete effective Coriolis frequency, as is explained in the appendices of Kunze's paper [41]. Should we be neglecting terms in the full expansion of the effective Coriolis frequency that may not be negligible in our cases (or perhaps other terms in the equation Kunze uses for its derivation), it could be possible that we are over- or under-estimating the critical value of the effective Coriolis frequency, and thus the region in which its alteration allows for PSI may be more expansive than we think. Such a situation could allow for the generation of PSI along this beam or above the ridge (though again, wave breaking makes it unlikely that traditional PSI theory could apply in above the ridge's case) as it would be in the basin-like region in the f_{eff}^2 plot in Figure 4.12. In such a case, nothing strange would be occurring here at all. Given that our selected spot over the ridge and the area along our beam seem to have approximately the same magnitude of f_{eff}^2 in the relevant plot in Figure 4.12, and given that their respective spectra

are of similar orders of magnitude, should PSI indeed somehow be possible in these regions, the results would seem to properly match expectations. Either way, examination of these and other strange regions like them could help shed light into the reason for their occurrence and possibly help explain more about wave phenomena like these in these types of simulations.

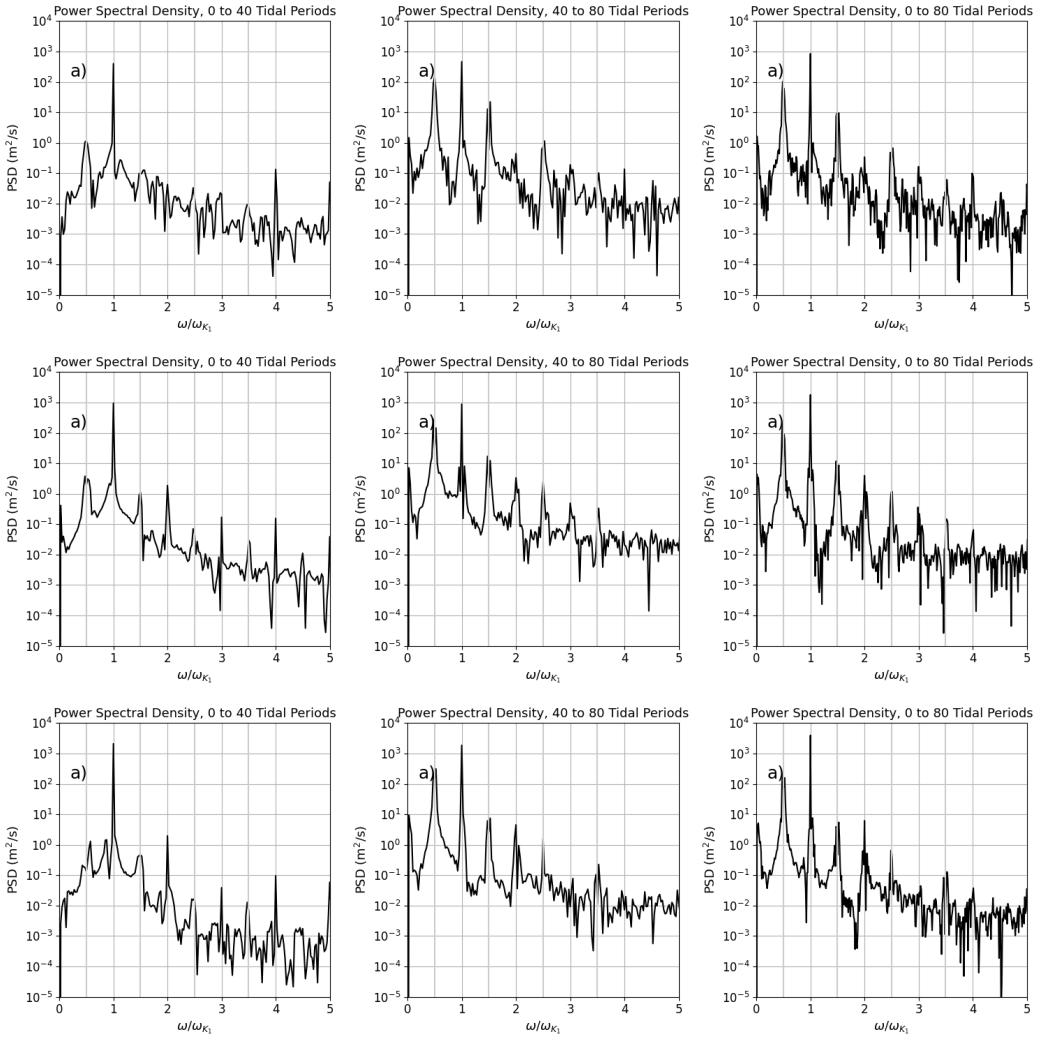

Figure 4.25: Plots of power spectral density in our case study (CS) along our studied beam between $x = 20$ km to $x = 45$ km and $z = -750$ m to $z = -300$ m. Specifically, the top row is spectra taken at $(x, z) = (25 \text{ km}, -650 \text{ m})$, the middle is at $(30 \text{ km}, -600 \text{ m})$, and the bottom row is at $(35 \text{ km}, -550 \text{ m})$ The power spectral density is shown as the magnitude of the spectrum at each frequency (in m^2/s) by ratio with the K_1 tidal frequency. From left to right in each row, these spectral density plots were taken from 0 to 40 tidal periods, 40 to 80 tidal periods, and 0 to 80 tidal periods.

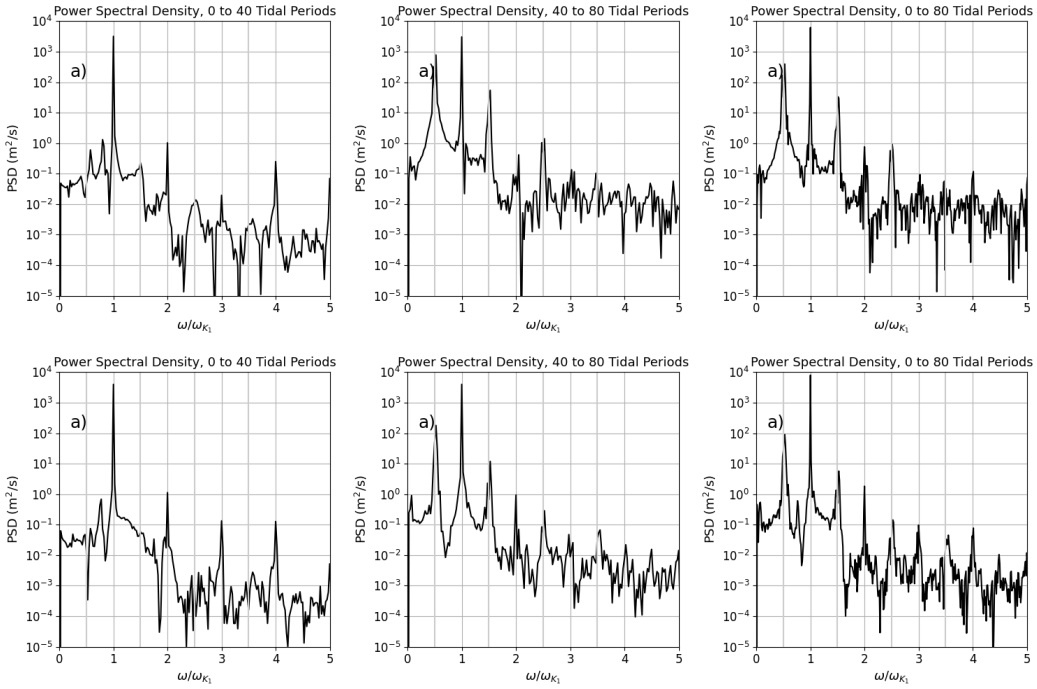

Figure 4.26: Plots of power spectral density in our case study (CS) along our studied beam between $x = 20$ km to $x = 45$ km and $z = -750$ m to $z = -300$ m. Specifically, the top row is spectra taken at $(x, z) = (40 \text{ km}, -500 \text{ m})$ and the middle is at $(45 \text{ km}, -450 \text{ m})$. The power spectral density is shown as the magnitude of the spectrum at each frequency (in m^2/s) by ratio with the K_1 tidal frequency. From left to right in each row, these spectral density plots were taken from 0 to 40 tidal periods, 40 to 80 tidal periods, and 0 to 80 tidal periods.

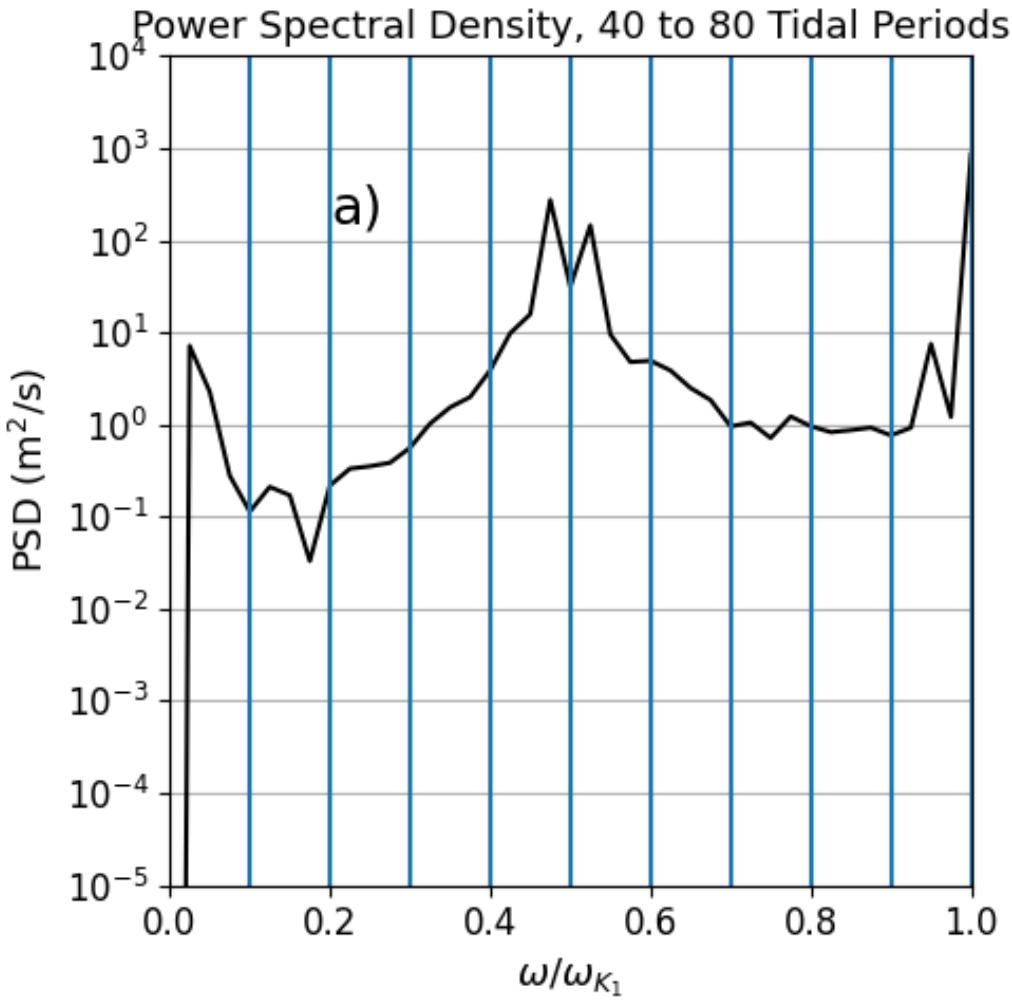

Figure 4.27: A plot of power spectral density in our case study (CS) along our studied beam between $x = 20$ km to $x = 45$ km and $z = -750$ m to $z = -300$ m. This plot is a zoomed-in version of the plot for $(x, z) = (30 \text{ km}, -600 \text{ m})$ between 40 and 80 tidal periods, with lines added to show every tenth of the tidal frequency between $0\omega_{K_1}$ and ω_{K_1}. The power spectral density is shown as the magnitude of the spectrum at each frequency (in m^2/s) by ratio with the K_1 tidal frequency.

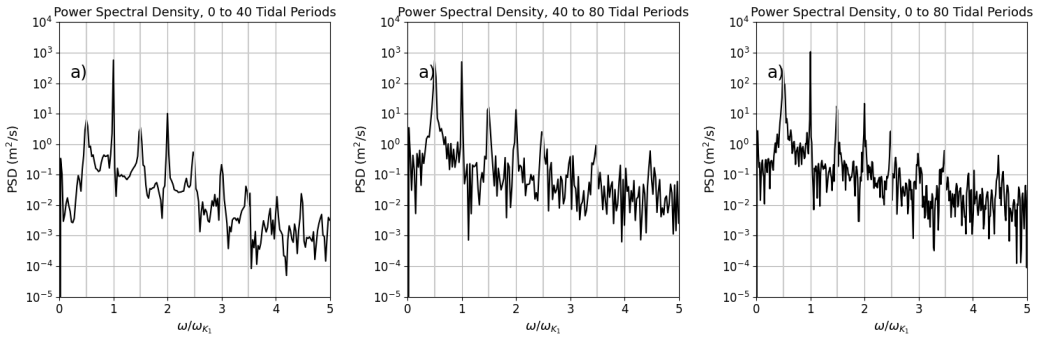

Figure 4.28: Plots of power spectral density in our case study (CS) near the top of our ridge. Specifically, these spectra were taken at $(x, z) = (5 \text{ km}, -900 \text{ m})$. The power spectral density is shown as the magnitude of the spectrum at each frequency (in m^2/s) by ratio with the K_1 tidal frequency. From left to right, these spectral density plots were taken from 0 to 40 tidal periods, 40 to 80 tidal periods, and 0 to 80 tidal periods.

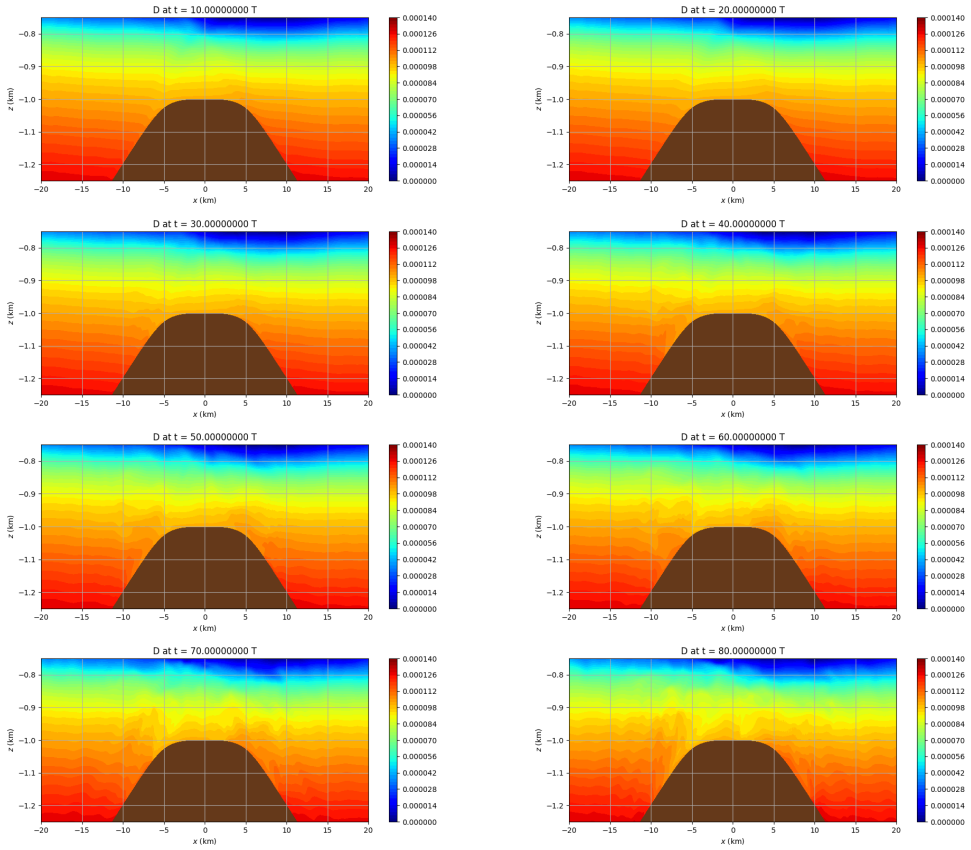

Figure 4.29: A collection of density profiles for our case study (CS), zoomed in on the top of the ridge. The colourbar shows the magnitude of the density D, which is dimensionless. From left-to-right, top-to-bottom, these plots show the density profiles at 10, 20, 30, 40, 50, 60, 70, and 80 tidal periods, respectively.

Chapter 5

Conclusion

In this thesis, we have worked to create a simulation in which the effects of parametric subharmonic instability could be observed in regions wherein the effective Coriolis frequency had been lowered, thus allowing for the development of resonant effects in locations where their generation would otherwise not be possible. After exploring the theory behind internal waves, PSI, and near-inertial waves and the effective Coriolis frequency, using a second-order, finite projection method-based model in 2D (with f-plane approximation), we simulated tidal flow over an isolated ridge with a steady along-ridge background current. Criteria were then developed for testing stability and iterating on parameters in the creation of test currents. Multiple different currents were created and examined, through the generation of different background velocity fields via the integration of density-field inputs via the thermal wind relation. Of these, one density structure in particular - a difference of hyperbolic tangent functions - was examined in greater depth. Through careful management of the shaping of the bathymetry, parameters of the current, and the tidal strength, a simulation was created wherein effects that could reasonably be attributed to PSI and the $(\frac{1}{2} + n)\omega_{K_1}$ harmonics where observed to occur in magnitudes between two orders of magnitude below to even exceeding that of the primary tidal frequency and its harmonics.

Understanding the transfer of energy in Earth's oceans is a vital component in solving a great variety of problems in a broad spectrum of disciplines, from mapping oceanic mixing, studying oceanic heating/cooling, modeling the shaping of continental shelves, and visualizing the distribution of nutrients essential for marine life, among many others. Internal wave interactions with seafloor topography make up almost half of the energy required for global overturning and circulation. PSI accounts for a significant portion of energy loss in

low-mode internal tides, particularly at critical latitudes. The intermittency of near-inertial internal waves makes up almost half of the internal waveband's energy. These factors all individually play vital roles in shaping the profile of energy and its transference in Earth's oceans - even more so when their interplay is considered. Indeed, as the effects of background vorticity shift the allowable regions for PSI, for example, we are capable of seeing energy transfer in regions where it would be otherwise considered impossible (or, similarly, with opposite vorticity, the exclusion of PSI in regions where it would otherwise be able to occur). That we are capable of viewing the effects of PSI in regions like these allows us to further develop our understanding of the movement of energy through these regions, and the consequences in which this may or may not result. By creating a simulation in which this phenomenon is visible, we aim to clearly illustrate its possibility while providing a point from which further examination of the interplay between these facets of internal waves may be continued, both within the framework of fluid dynamics and beyond.

Possible extensions of this work could include further examination of other current types, different shaping of ridges or other seafloor topographies, exploring further lengthened simulations for the observation of longer- and wider-scale effects, and transitioning the work into 3D, allowing for the observation of turbulence and its effects around the ridge. Further investigation with observational data could also be used to explore, refine, and verify the simulations presented here. Near-inertial internal waves and the instabilities they experience, such as PSI, play significant roles in the global oceanic mixing and circulation. Should the effects of a lowered inertial frequency cause the development of PSI in regions otherwise not possible, the areas in which PSI and its effects - and the resulting transfer of energy - are visible expand. Such phenomena could explain the movement of energy and circulation of ocean waters in capacities that the two phenomena alone are incapable of completely capturing. Therefore, the development and expansion of simulations like these could play an integral role in helping to develop our understanding of the transfer of energy in Earth's oceans, and understanding near-inertial wave phenomena on a larger scale.

Bibliography

[1] Ferrari, R., Wunsch, C. (2004). *Vertical mixing, energy, and the general circulation of the oceans*. Annu. Rev. Fluid Mech., 36, 281–314, doi: 10.1146/annurev.fluid.36.050802.122121.

[2] Klymak, J. M., Legg, S., Alford, M. H., Buijsman, M., Pinkel, R., Nash, J. D. (2012). *The direct breaking of internal waves at steep topography*. Oceanography 25(2):150–159. http://dx.doi.org/10.5670/oceanog.2012.50.

[3] Boyd, P. (2007). *Biogeochemistry: Iron findings*. Nature, 446(7139):989–991.

[4] Liang, Y., Couston L. A., Guo, Q., Alam, M. R. (2017). *Dominant resonance in parametric subharmonic instability of internal waves*. arXiv:1709.06250 [physics.flu-dyn].

[5] Dunphy, M., Lamb, K. G. (2014). *Focusing and vertical mode scattering of the first mode internal tide by mesoscale eddy interaction*. J. Geophys. Res. Oceans, 119. doi:10.1002/2013JC009293.

[6] Lamb, K. G., Dunphy, M. (2018). *Internal wave generation by tidal flow over a two-dimensional ridge: energy flux asymmetries induced by a steady surface trapped current*. J. Fluid Mech. (2018), vol. 836, pp. 192–221. doi:10.1017/jfm.2017.800.

[7] Ferrari, R., Wunsch, C. (2009). *Ocean circulation kinetic energy: Reservoirs, sources, and sinks*. Annu. Rev. Fluid Mech., 41(1), 253–282. doi:10.1146/annurev.fluid.40.111406.102139.

[8] Schafstall, J., Dengler, M., Brandt, P., Bange, H. (2010). *Tidal induced mixing and diapycnal nutrient fluxes in the Mauritanian upwelling region*. J. Geophys. Res., 115, C10014. doi:10.1029/2009JC005940.

[9] Garrett, C., Kunze, E. (2007). *Internal tide generation in the deep ocean*. Annu. Rev. Fluid Mech., 39, 57–87. doi:10.1146/annurev.fluid.39.050905.110227.

[10] Zhao, Z., Alford, M. H., Girton, J. B. (2012). *Mapping low-mode internal tides from multisatellite altimetry*. Oceanography, 25(2), 42–51. doi: 10.5670/oceanog.2012.40.

[11] Nikurashin, M., Ferrari, R. (2013). *Overturning circulation driven by breaking internal waves in the deep ocean*. Geophys. Res. Lett. 40, 3133–3137.

[12] Ferrari, R., Mashayek, A., McDougall, T. J., Nikurashin, M., Campin, J. M. (2016). *Turning ocean mixing upside down*. J. Phys. Oceanogr. 46, 2239–2261.

[13] Falahat, S., Nycander, J., Roquet, F., Zarroug, M. (2014). *Global calculation of tidal energy conversion into vertical normal modes*. Journal of Physical Oceanography, 44(12), 3225-3244.

[14] Nash, J. D., Alford, M. H. Kunze, E., Martini, K., Kelley, S. (2007). *Hotspots of deep ocean mixing on the Oregon continental slope*. Geophysical Research Letters 34, L01605, http://dx.doi.org/ 10.1029/2006GL028170.

[15] MacKinnon, J. A., Winters, K. B. (2005). *Subtropical catastrophe: Significant loss of low-mode tidal energy at 28.9°N*. Geophysical Research Letters 32, 15605, http://dx.doi.org/ 10.1029/2005GL023376.

[16] Bell, T.H. (1975). *Lee waves in stratified flows with simple harmonic time dependence*. Journal of Fluid Mechanics 67:705–722, http://dx.doi.org/10.1017/S0022112075000560.

[17] Balmforth, N., G. Ierley, W. Young. (2002). *Tidal conversion by subcritical topography*. Journal of Physical Oceanography 32:2,900–2,914, http://dx.doi.org/10.1175/1520-0485(2002)032 ¡2900:TCBST¿2.0.CO;2.

[18] Llewellyn Smith, S. G., Young, W. R. (2003). *Tidal conversion at a very steep ridge*. Journal of Fluid Mechanics 495:175–191, http://dx.doi.org/10.1017/S0022112003006098.

[19] St. Laurent, L. C., Stringer, S., Garrett, C., Perrault-Joncas., D. (2003). *The generation of internal tides at abrupt topography*. Deep Sea Research Part I 50:987–1,003, http://dx.doi.org/ 10.1016/S0967-0637(03)00096-7.

[20] Drazin, P. G. (1977). *On the instability of an internal gravity wave*. Proceedings of the Royal Society of London. A. Mathematical and Physical Sciences, 356(1686), 411-432.

[21] Korobov, A. S., Lamb, K. G. (2008). *Interharmonics in internal gravity waves generated by tide-topography interaction*. Journal of Fluid Mechanics, 611, 61-95.

[22] McComas, C. H., Müller, P. (1981). *The dynamic balance of internal waves*. Journal of Physical Oceanography, 11(7), 970-986.

[23] Alford, M. H., MacKinnon, J. A., Simmons, H. L., Nash, J. D. (2016). *Near-inertial internal gravity waves in the ocean*. Annual review of marine science, 8, 95-123.

[24] Olbers, D., Pomphrey, N. (1981) *Disqualifying two candidates for the energy balance of oceanic internal waves*. J. Phys. Oceanogr. 11, 1423–1425.

[25] Eden, C., Olbers, D. (2014). *An energy compartment model for propagation, nonlinear interaction, and dissipation of internal gravity waves*. Journal of Physical Oceanography, 44(8), 2093-2106.

[26] Hazewinkel, J., Winters, K. B. (2011). *PSI of the internal tide on a β plane: flux divergence and near-inertial wave propagation*. Journal of physical oceanography, 41(9), 1673-1682.

[27] Alford, M. H., MacKinnon, J. A., Zhao, Z., Pinkel, R., Klymak, J., Peacock, T. (2007). *Internal waves across the Pacific*. Geophysical Research Letters, 34(24).

[28] MacKinnon, J. A., Alford, M. H., Sun, O., Pinkel, R., Zhao, Z., Klymak, J. (2013). *Parametric subharmonic instability of the internal tide at 29 N*. Journal of Physical Oceanography, 43(1), 17-28.

[29] Lvov Y. V., Polzin K. L., Yokoyama N. (2012). *Resonant and near-resonant internal wave interactions*. J. Phys. Oceanogr. 42:669–91

[30] Staquet, C., Sommeria, J. *Internal gravity waves: from instabilities to turbulence*. Annu. Rev. Fluid Mech. 2002.34:559-593.

[31] MacKinnon, J. A., Winters, K. B. (2007). *Tidal mixing hotspots governed by rapid parametric subharmonic instability*. J. Phys. Oceanogr. (submitted).

[32] Javam, A., Imberger, J., Armfield, S. W. (1999). *Numerical study of internal wave reflection from sloping boundaries*. Journal of Fluid Mechanics, 396, 183-201.

[33] Javam, A., Imberger, J., Armfield, S. W. (2000). *Numerical study of internal wave–wave interactions in a stratified fluid*. Journal of Fluid Mechanics, 415, 65-87.

[34] MacKinnon, J. A., Winters, K. B. (2003). *Spectral evolution of bottom-forced internal waves*. In Near-Boundary Processes and Their Parameterization: Proc. 13th 'Aha Huliko'a Hawaiian Winter Workshop (pp. 73-83).

[35] Lamb, K. G. (2004). *Nonlinear interaction among internal wave beams generated by tidal flow over supercritical topography*. Geophysical Research Letters, 31(9).

[36] Gerkema, T., Staquet, C., Bouruet-Aubertot, P. (2006). *Decay of semi-diurnal internal-tide beams due to subharmonic resonance*. Geophysical Research Letters, 33(8).

[37] Fu, L. L. (1981). *Observations and models of inertial waves in the deep ocean*. Reviews of Geophysics, 19(1), 141-170.

[38] Garrett, C., Munk, W. (1972). *Space-time scales of internal waves*. Geophysical Fluid Dynamics, 3(3), 225-264.

[39] Garrett, C., Munk, W. (1975). *Space-time scales of internal waves: A progress report*. Journal of Geophysical Research, 80(3), 291-297.

[40] Munk, W. (1981). *Internal waves and small-scale processes*. B.A. Warren and C. Wunsch, Eds. The MIT Press, 264-291.

[41] Kunze, E. (1985). *Near-inertial wave propagation in geostrophic shear*. Journal of Physical Oceanography, 15(5), 544-565.

[42] Mooers, C. N. (1975). *Several effects of a baroclinic current on the cross-stream propagation of inertial-internal waves*. Geophysical and Astrophysical Fluid Dynamics, 6(3), 245-275.

[43] Kunze, E. (1986). *The mean and near-inertial velocity fields in a warm-core ring*. Journal of physical oceanography, 16(8), 1444-1461.

[44] Halle C. (2003). *Internal wave variability in the Beaufort Sea during the winter of 1993/1994*. J. Geophys. Res. 108:3210

[45] Rainville, L., Pinkel, R. (2004). *Observations of energetic high-wavenumber internal waves in the Kuroshio*. Journal of physical oceanography, 34(7), 1495-1505.

[46] Zhai X., Greatbatch R. J., Zhao J. (2005). *Enhanced vertical propagation of storm-induced near-inertial energy in an eddying ocean channel*. Geophys. Res. Lett. 32:L18602

[47] Zhai X., Greatbatch R. J., Eden C. (2007). *Spreading of near-inertial energy in a 1/12◦ model of the North Atlantic Ocean*. Geophys. Res. Lett. 34:L10609

[48] Alford, M. H., Whitmont, M. (2007). *Seasonal and spatial variability of near-inertial kinetic energy from historical moored velocity records*. J. Phys. Oceanogr., 37, 2022–2037, https://doi.org/10.1175/JPO3106.1.

[49] Shearman, R. K. (2005). *Observations of near-inertial current variability on the New England Shelf*. J. Geophys. Res., 110, C02012, https://doi.org/10.1029/2004JC002341.

[50] Choi, J., Troy, C. D., Hsieh, T. C., Hawley, N., McCormick, M. J. (2012). *A year of internal Poincaré waves in southern Lake Michigan*. J. Geophys. Res., 117, C07014, https://doi.org/10.1029/2012JC007984.

[51] Price, J. F. (1983). *Internal wave wake of a moving storm. Part I: Scales, energy budget, and observations*. J. Phys. Oceanogr., 13, 949–965, https://doi.org/10.1175/1520-0485(1983)013¡0949:IWWOAM¿2.0.CO;2.

[52] D'Asaro, E. A., Eriksen, C. C., Levine, M. D., Niiler, P., Van Meurs, P. (1995). *Upper-ocean inertial currents forced by a strong storm. Part I: Data and comparisons with linear theory*. Journal of Physical Oceanography, 25(11), 2909-2936.

[53] Weller, R. A. (1982). *The relation of near-inertial motions observed in the mixed layer during the JASIN (1978) experiment to the local wind stress and to the quasi-geostrophic flow field*. J. Phys. Oceanogr., 12, 1122–1136, https://doi.org/10.1175/1520-0485(1982)012¡1122:TRONIM¿2.0.CO;2.

[54] Pettigrew, N. R.. (1980). *The dynamics and kinematics of the coastal boundary layer off Long Island*. Ph.D. thesis, Massachusetts Institute of Technology, 262 pp., https://doi.org/10.1575/1912/3727.

[55] Kelly, S. M. (2019). *Coastally generated near-inertial waves*. Journal of Physical Oceanography, 49(11), 2979-2995.

[56] Yang, W., Hibiya, T., Tanaka, Y., Zhao, L., Wei, H. (2018). *Modification of parametric subharmonic instability in the presence of background geostrophic currents*. Geophysical Research Letters, 45, 12,957–12,962. https://doi.org/10.1029/2018GL080183

[57] Lamb, K.G. (2021). *IGW: A 2-D numerical model for investigating internal wave generation in the ocean*. University of Waterloo.

[58] Elsevier B. V. (n.d.). Boussinesq approximation. *Boussinesq Approximation - an overview — ScienceDirect Topics*. Retrieved July 8, 2022, from https://www.sciencedirect.com/topics/earth-and-planetary-sciences/boussinesq-approximation

[59] Cushman-Roisin, B., Beckers, J. M. (2011). *Introduction to geophysical fluid dynamics: physical and numerical aspects*. Academic press.

[60] Phillips, O. M. (1966). *The dynamics of the upper ocean*. Cambridge UP.

[61] Tabaei, A., Akylas, T. R. (2003). *Nonlinear internal gravity wave beams*. Journal of Fluid Mechanics, 482, 141-161.

[62] Lamb, K. G. (2022). *Ocean Waves*. University of Waterloo.

[63] Lamb, K. G. (n.d.).*AM867: Dispersive and Nonlinear Waves. Resonant Triads*. University of Waterloo.

[64] Wang, S., Cao, A., Liang, X., Chen, X., Meng, J. (2021). *Impact of background geostrophic currents with vorticity on resonant triad interaction over midocean ridges*. Journal of Geophysical Research: Oceans, 126, e2021JC017227. https://doi.org/10.1029/2021JC017227

[65] Bell, J. B., Colella, P., Glaz, H. M. (1989). *A second-order projection method for the incompressible Navier-Stokes equations*. Journal of computational physics, 85(2), 257-283.

[66] Bell, J., Solomon, J., Szymczak, W. (1989). *A second-order projection method for the incompressible navier stokes equations on quadrilateral grids*. In 9th Computational Fluid Dynamics Conference (p. 1967).

[67] Bell, J. B., Marcus, D. L. (1992). *A second-order projection method for variable-density flows*. Journal of Computational Physics, 101(2), 334-348.

[68] Urbancic, G., Lamb, K., Fer, I., Padman, L. (2022). The generation of linear and nonlinear internal waves forced by sub-inertial tides over the Yermak Plateau, Arctic Ocean. Journal of Physical Oceanography. 10.1175/JPO-D-21-0264.1.

[69] Hua, B. L., Moore, D. W., Le Gentil, S. (1997). *Inertial nonlinear equilibration of equatorial flows*. Journal of Fluid Mechanics, 331, 345-371.

APPENDICES

Appendix A

Table of Cases in Chapter 4

Case Name	**Section**	**Background Density Structure** $-\frac{g}{N^2}\rho(x,z)$
No Current (NC)	4.1.1	z
Unstable $1+\tanh$ (U1PT)	4.1.2	$4[1+\tanh(\frac{z+1500}{50})][1+\tanh(\frac{x+30000}{40000})]^2$
Unstable Difference of Tanh Functions (UDT)	4.1.2	$400[1+\tanh(\frac{z+400}{100})]\{[\tanh(\frac{x+30000}{20000})-\tanh(\frac{x-30000}{20000})]\}^2$
$1+\tanh$ (1PT)	4.2.1	$400[1+\tanh(\frac{z+750}{100})][1+\tanh(\frac{x+30000}{40000})]^2$
sech (S)	4.2.2	$400[1+\tanh(\frac{z+400}{100})]\text{sech}^2(\frac{x+10000}{40000})$
Difference of Tanh Functions (DT)	4.2.3	$800[1+\tanh(\frac{z+400}{50})][\tanh(\frac{x+30000}{40000})-\tanh(\frac{x-30000}{40000})]^2$
Case Study (CS)	4.3.1	$800[1+\tanh(\frac{z+750}{50})][\tanh(\frac{x+30000}{40000})-\tanh(\frac{x-30000}{40000})]^2$
Case Study 7.5 km Top Length (CS7.5kmTop)	4.3.2	$800[1+\tanh(\frac{z+750}{50})][\tanh(\frac{x+30000}{40000})-\tanh(\frac{x-30000}{40000})]^2$
Case Study 15 km Top Length (CS15kmTop)	4.3.2	$800[1+\tanh(\frac{z+750}{50})][\tanh(\frac{x+30000}{40000})-\tanh(\frac{x-30000}{40000})]^2$
Case Study 5% Parameter Increase (CSP5%)	4.3.2	$840.5[1+\tanh(\frac{z+750}{50})][\tanh(\frac{x+30000}{41000})-\tanh(\frac{x-30000}{41000})]^2$
Case Study 5% Parameter Decrease (CSM5%)	4.3.2	$760.5[1+\tanh(\frac{z+750}{50})][\tanh(\frac{x+30000}{39000})-\tanh(\frac{x-30000}{39000})]^2$
Case Study with No Visible PSI (CSNoPSI)	4.3.3	$800[1+\tanh(\frac{z+750}{50})][\tanh(\frac{x+30000}{40000})-\tanh(\frac{x-30000}{40000})]^2$

Table A.1: A list of all the simulations present in Chapter 4, organized by the name and abbreviation of the test case, the relevant section in the text in which it appears, and the background density structure (simplified for brevity). Cases are presented in the order in which they appear in the text. Note that some cases have identical background structures, and will differ by parameters laid out in their titles and described in the relevant text sections.